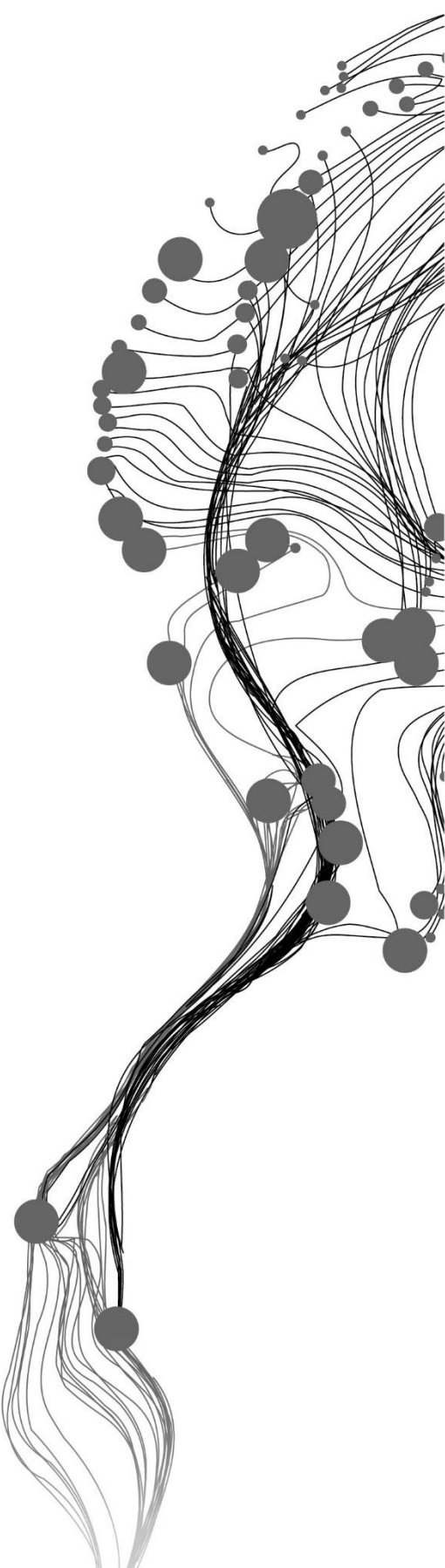


Estimating and mapping aboveground biomass/carbon stock using ALOS-2 PALSAR-2 in the mangrove forest in East Kalimantan, Indonesia

MST KARIMON NESHA
February 2019

SUPERVISORS:
Dr. Yousif A. Hussin
Ir. L.M. van Leeuwen-de Leeuw

ADVISOR:
Dr. Y. Budi Sulistioadi
University of Mulawarman, Samarinda, Indonesia



ESTIMATING AND MAPPING ABOVEGROUND BIOMASS/CARBON STOCK USING ALOS-2 PALSAR-2 IN THE MANGROVE FOREST IN EAST KALIMANTAN, INDONESIA

MST KARIMON NESHA

Enschede, The Netherlands, February 2019

Thesis submitted to the Faculty of Geo-Information Science and Earth Observation of the University of Twente in partial fulfilment of the requirements for the degree of Master of Science in Geo-information Science and Earth Observation.

Specialization: Natural Resources Management

SUPERVISORS:

Dr. Yousif A. Hussin

Ir. L.M. van Leeuwen-de Leeuw

ADVISOR:

Dr. Y. Budi Sulistioadi

University of Mulawarman, Samarinda, Indonesia

THESIS ASSESSMENT BOARD:

Prof. Dr. A.D. Nelson

Dr. Tuomo Kauranne (External Examiner, Lappeenranta University of Technology, Finland)

DISCLAIMER

This document describes work undertaken as part of a programme of study at the Faculty of Geo-Information Science and Earth Observation of the University of Twente. All views and opinions expressed therein remain the sole responsibility of the author and do not necessarily represent those of the Faculty.

ABSTRACT

UN-REDD+ program introduces the MRV mechanism for AGB/carbon stock estimation to reduce the emissions from deforestation and forest degradation in the tropics. The MRV mechanism requires a low cost and robust technique to estimate AGB/carbon stock with reasonable accuracy in the tropical forests. Among the different RS techniques, L-band SAR estimates AGB with high accuracy in the inland tropical forests. However, the accuracy of AGB estimation in the tropical mangrove forests is relatively low. Therefore, this study was carried out to estimate AGB/carbon stock using backscatter coefficients of ALOS-2 PALSAR-2 in part of the planted mangrove forest at Mahakam Delta, East Kalimantan, Indonesia. The forest parameters (DBH and tree height) were collected from a total of 71 sampling plots in October 2018. The parameters were used to calculate the field-based AGB using an allometric equation for the mangrove forests. PALSAR-2 data with level 1.1 fine beam dual (FBD) polarization was obtained from JAXA. Linear regression models were applied to estimate AGB in the study area (105 ha) using HV and HH backscatter coefficients of PALSAR-2. The accuracy of the AGB estimation was assessed in terms of R^2 , RMSE, and p-value. The results of the linear regression models in our study revealed that HV backscatter coefficients estimate AGB with higher accuracy at R^2 of 0.89, RMSE of 23.16 tons ha^{-1} and p-value < 0.01 . The accuracy of the model validation was also higher at R^2 of 0.89, RMSE of 22.69 tons ha^{-1} and p-value < 0.01 . This implied that HV backscatter coefficients of PALSAR-2 predicted AGB in the mangrove forest with 89% accuracy in our study. Therefore, the equation derived from the simple linear regression model was used to map the AGB and carbon stock in the study area. The estimated AGB in the study area of the mangrove forest ranged from 1 to 350 tons ha^{-1} with an average of 181 tons ha^{-1} , and the total AGB accounted for 13, 719 tons.

The findings of our study showed a promising accuracy in estimating AGB using HV polarized ALOS-2 PALSAR-2 backscatter coefficients in the mangrove forest. Therefore, our study concluded that L-band ALOS-2 PALSAR-2 data has a great potential to estimate AGB with high accuracy in the mangrove forest as in the inland forest in the tropics. Thus, the findings of our study can contribute to the MRV mechanism of UN-REDD+ program for monitoring the carbon emission reduction in the mangrove forests in the tropics.

Keywords: Aboveground Biomass, Carbon Stock, Mangrove Forest, Regression Model, HV and HH Polarization Backscatter, ALOS-2 PALSAR-2

ACKNOWLEDGMENTS

I thank the Faculty of Geo-information Science and Earth Observation (ITC), the University of Twente for providing the financial support to conduct fieldwork in Indonesia and obtain ALOS-2 PALSAR-2 data from JAXA. I also thank ITC for financial assistance to pursue my MSc.

I am greatly thankful to my supervisor Dr. Yousif Ali Hussin for his cordial guidance and support during the entire research period including the fieldwork. It is a privilege to work under his cordial and close supervision. I also thank my second supervisor Ir. L.M. van Leeuwen-de Leeuw for her feedback to improve my research work.

I highly acknowledge and appreciate the support of the Indonesian Ministry of Science and Technology and Higher Education by offering our team a research permit to execute our research activities and our fieldwork in Indonesia.

I cordially thank Mulawarman University, Samarinda, Indonesia for their assistance with the logistics and data collection in the study site Mahakam Delta, East Kalimantan. I specially thank to Dr. Budi Sulistioadi, and his team (M. Lutfi hamadan and Mita Priskawanti), Faculty of Forestry, Mulawarman University to facilitate our fieldwork in the mangrove forest. I thank our research group for their cooperation during fieldwork. It is also my pleasure to thank local people of Tani Baru village at Mahakam Delta for their hospitality and support during my stay there for field data collection.

My sincere gratitude also goes to Drs. RG. Nijmeijer, NRM Course Director, for his kind support, motivation, and cooperation during the entire course period. I am delighted and privileged to have such a kind and compassionate course director.

I would also like to express my gratitude to Prof. Dr. A.D. Nelson and Dr. Ling Chang for their constructive advice on my thesis.

Finally, I thank my parents with great honor for their perseverance, prayers, and inspiration in taking my steps forward to achieve my dreams and aspirations.

Mst Karimon Nesha
Enschede, The Netherlands
February 2019.

TABLE OF CONTENTS

1.	Introduction.....	1
1.1.	Problem Statement and Justification.....	3
1.2.	Research Objectives.....	3
1.3.	Research Questions.....	4
1.4.	Research Hypothesis.....	4
1.5.	Assumptions.....	4
2.	Literature Review.....	5
2.1.	Radar.....	5
2.2.	Polarimetric Backscattering.....	6
2.3.	Factors affecting Backscattering of SAR.....	6
2.4.	Forest and L-band SAR Backscattering.....	9
2.5.	Application of L-band SAR for Forest Biomass Estimation.....	10
2.6.	Application of L-band SAR for Biomass Estimation in the Mangrove.....	11
3.	Materials and Methodology.....	12
3.1.	Study Area.....	12
3.2.	Study Materials.....	14
3.3.	Study Design.....	15
3.4.	Sampling Design.....	16
3.5.	Field Plot Establishment.....	16
3.6.	Data Collection.....	17
3.7.	Data Processing.....	19
3.8.	Analysis.....	24
4.	Results.....	28
4.1.	Descriptive Analysis of the Study Data.....	28
4.2.	Correlation Analysis between Backscatter Coefficients and Forest Parameters.....	30
4.3.	The relationship between HV Backscatter and BA, DBH & Tree Height.....	31
4.4.	Relationship of BA, DBH and Tree Height with AGB.....	32
4.5.	The Regression between AGB and Backscatter Coefficients.....	33
4.6.	Model Development, Validation and Accuracy Assessment.....	36
4.7.	Estimation of AGB Saturation Point in relation to HV Backscatter.....	38
4.8.	AGB and Carbon Stock Map of the Study Area.....	39
5.	Discussion.....	42
5.1.	Data and Method of AGB Estimation.....	42
5.2.	The relationship between AGB and Backscatter Coefficients.....	43
5.3.	The relationship between BA, DBH, Tree Height and Backscatter Coefficients.....	48
5.4.	Determination of AGB Saturation.....	49
5.5.	AGB and Carbon Stock Map.....	49
5.6.	Limitations and Uncertainties of the Study.....	50
5.7.	The Relevance of the Study.....	52
6.	Conclusion.....	54
6.1.	Conclusion.....	54
6.2.	Recommendations.....	54
	List of References.....	56
	List of Appendices.....	64

LIST OF FIGURES

Figure 1: Illustration of radar backscatter (adapted from Natural Resources Canada, 2015a).....	6
Figure 2: Radar penetration in X-band (3 cm), C-band (5 cm) and L-band (24 cm) wavelengths for forest vegetation (adapted from DLR, 2013).....	7
Figure 3: Soil backscatter as a function of dielectric constant (adapted from Humboldt State University, 2016).....	9
Figure 4: Scattering mechanisms from forest vegetation (adapted and modified from Carver, 1988)	9
Figure 5: Zonation of mangroves (adapted from Kushan, 2016).....	10
Figure 6: Radar backscattering from the flooded forest (adapted and modified from Carver et al.,1988)...	10
Figure 7: Location map of the study area.....	13
Figure 8: Methodological flowchart of the study.....	16
Figure 9: A circular plot of 500 m ² (adapted from Asmare, 2013 and Sumareke, 2016).....	17
Figure 10: DBH measurement of <i>Rhizophora</i> Species, the measurement was taken at 1.3 m height from the stem base/junction over the prop roots.....	18
Figure 11: Retrieval of HV backscatter/NRCS in dB using equation 1 in SNAP.....	20
Figure 12: Geometric correction and geo-referencing of the PALSAR-2 data, Range Doppler Terrain Correction and coordinate system, WGS_1984_UTM_Zone_50S were used.	21
Figure 13: Establishment of the 3 by 3 pixels for extraction of backscatter values from the plot.	22
Figure 14: Location of plot center between two or more pixels.	22
Figure 15: The plot center is shown on top of the drone image, the yellow dots are the plot center, and the purple circle is the perimeter of the plot.	23
Figure 16: The shifting of the plot center for establishment 3 by 3 pixels window. The red points mark the original position, and the yellow points represent the final position of the plot center after shifting.	23
Figure 17: Distribution of tree species in the field plots.....	28
Figure 18: Density curve over the histogram of AGB, the line represents the density curve, and the bar chart represents a histogram of AGB distribution.....	29
Figure 19: Density curve over the histogram of HV backscatter, the line represents the density curve, and the bar chart represents a histogram of HV distribution.....	29
Figure 20: Normal Q-Q plot of AGB distribution.	29
Figure 21: Normal Q-Q plot of HV backscatter values.....	29
Figure 22: A linear regression between HV backscatter coefficients and BA; the black dots are field-measured BA, and orange dot points along the regression line are the predicted BA by the regression.	31
Figure 23: A linear regression between HV backscatter and DBH, the black dots are field-measured DBH, and orange dots along the regression line are the predicted DBH by the regression.	32
Figure 24: A linear regression between HV backscatter and tree height, the black dot points are field-measured tree height and orange dot points along the regression line are predicted tree height by the regression.....	32
Figure 25: The scatterplot of the linear regression using BA to predict AGB, the black dots represents field-measured AGB, and orange dots along the regression line (solid line) represents predicted AGB by the regression.....	32
Figure 26: A linear regression using HV backscatter coefficients to predict AGB, the black dots represent field measured AGB and orange dots on the regression line (solid line) represents predicted AGB by the regression.....	34
Figure 27: A linear regression between HH backscatter coefficients and AGB, the black dots represent field-measured AGB, the purple dots on the regression line represent predicted AGB by the regression.....	35
Figure 28: The regression model between HV Backscatter and field-measured AGB, the black dots represent field-measured AGB while the purple dots represent the predicted AGB along the regression line by the regression model.....	37
Figure 29: The regression model validation between observed AGB and estimated AGB, the black points represent field measured AGB while the orange line represents the AGB predicted by the regression model validation.....	38
Figure 30: AGB saturation point with respect to HV backscatter coefficients. The red vertical line intersecting at the slope of 0.01dB depicts the AGB saturation point at 216.9 tons ha ⁻¹ . The yellow line represents the consecutive decrease in slope over the curve before it reached to 0.01dB.....	39

Figure 31: AGB map of the study area at Mahakam mangrove forest, East Kalimantan, Indonesia.....	40
Figure 32: The frequency distribution of the estimated AGB using its histogram. The values more than zero (75 ha) represents ABG values, and the rest is water (20 ha).....	40
Figure 33: Carbon stock map of the study area at Mahakam Delta mangrove forest, East Kalimantan, Indonesia.....	41
Figure 34: Volume scattering of radar signals from vegetation canopy (adapted from Carver, 1988).....	43
Figure 35: The linear regression between speckle filtered HV backscatter and AGB, the black dots are field-measured AGB, and magenta dots along the regression line of best fit are the predicted AGB by the regression.	45
Figure 36: An example Radar backscattering in wet and dry conditions for the forest (adapted from ITC course materials, Anonymous, 2018).....	46
Figure 37: Radar signal from the flooded forest (after Richards et al., 1987).....	47
Figure 38: Relative radar returns in response to wavelength and different vegetation conditions (after Henderson and Lewis, 1998).	47
Figure 39: Radar return from Cypress swamp forest in Northern Florida (adapted from Hussin, 1990)..	47
Figure 40: The sources of errors in AGB estimation in the tropical forests from the sampling plots (adapted from Chave et al., 2004).	51
Figure 41: HV backscatter image before geometric correction.	52
Figure 42: HV backscatter image after geometric correction.....	52
Figure 43: Geocoding of L-band SAR image using DEM (adapted from Logan, 1997).....	52

LIST OF TABLES

Table 1: A list of field study equipment with their purpose.....	14
Table 2: A list of data used in this research.	14
Table 3: A list of software used in this research.....	15
Table 4: A detail specification of the ALOS-2 PALSAR-2data used in this study.....	19
Table 5: The descriptive statistics of all the study parameters.	28
Table 6: The correlation analysis between forest parameters and backscatter coefficients of PALSAR-2. .	30
Table 7: Summary statistics of the regression between HV backscatter and BA, DBH & tree height.	31
Table 8: Summary statistics of regression between BA and AGB.	33
Table 9: Summary statistics of regression analysis between HV backscatter and AGB.	34
Table 10: Summary statistics of the relationship between HH backscatter and AGB.....	35
Table 11: Summary statistics of multi-linear regression between AGB and HV, HH backscatter.....	36
Table 12: Summary statistics of the regression model between AGB and HV backscatter.	37
Table 13: Summary statistics of the model validation.	38
Table 14: The total AGB for different AGB ranges with corresponding pixel numbers.....	40

LIST OF EQUATIONS

Equation 1: Retrieval of PALSAR-2 backscatter coefficients/ NRCS.....	20
Equation 2: Allometric equation for calculation of AGB.....	24
Equation 3: AGB calculation in tons per ha.	24
Equation 4: Calculation of carbon stock using conversion factor.....	24
Equation 5: Calculation of BA.	24
Equation 6: Linear regression function between HV backscatter coefficients and field-measured AGB...	26
Equation 7: Equation for RMSE calculation.	27
Equation 8: Determination of AGB saturation point using slope between changes in HV backscatter coefficients and changes in AGB.....	27

LIST OF APPENDICES

Appendix 1: Radar system and its comparison to optical RS system.	64
Appendix 2: Microwave region of the electromagnetic spectrum.....	64
Appendix 3: SAR imaging geometry system.....	64
Appendix 4: Outlook of ALOS-2 and observation attitude of PALSAR-2.	64
Appendix 5: Observation modes of PALSAR-2.....	65
Appendix 6: Scattering mechanisms of Radar.....	65
Appendix 7: Incidence angle in relation to surface roughness.	65
Appendix 8: The diffuse, specular and corner reflectance.	66
Appendix 9: The effects of topography/local incidence angle on Radar backscattering.	66
Appendix 10: Tree height measurement of <i>Rhizophora spp.</i>	66
Appendix 11: DBH and tree height measurement of the <i>Avicennia alba</i> tree species.	66
Appendix 12: Multi-stem trees of <i>Rhizophora</i> and <i>Avicennia</i> species.....	67
Appendix 13: An example of a field datasheet.	67
Appendix 14: Ground surface during peak hours of low tide in the study area.	67
Appendix 15: Summary of the study parameters per plot; the plots with yellow marker denotes the validation plot and other plots are model plots.	68
Appendix 16: The original ALOS-2 PALSAR-2 data with DN values.	70
Appendix 17: HV polarized PALSAR-2 image after speckle filtering.....	70
Appendix 18: Some pictures of the water channels and Mahakam river near the sample plots, and muddy ground surface covered by water in the sample plots taken during data collection in the field.....	71
Appendix 19: The photos of sample plot 3 and plot 4 taken during data collection.....	71
Appendix 20: The sampling plots (71) on the PALSAR-2 backscatter image; 42 plots for model development and 29 plots for model validation.....	72
Appendix 21: The results of the correlation analysis between the field-measured AGB and speckle filtered HV polarization backscatter coefficients.....	72
Appendix 22: The results of correlation analysis between AGB and other forest parameters.....	72
Appendix 23: The results of the correlation between AGB and the derivatives of HH and HV polarization backscatter coefficients.....	73
Appendix 24: Regression analysis between AGB and DBH.....	73
Appendix 25: The regression analysis between AGB and tree height.....	74
Appendix 26: Residuals of the regression analysis between HV backscatter and AGB.....	74
Appendix 27: The regression analysis between the sum backscatter coefficients (HV+HH) and AGB.....	75
Appendix 28: The regression analysis between the ratio of HV/HH backscatter coefficients and AGB. ..	76
Appendix 29: The regression analysis between the ratio of HH/HV backscatter coefficients and AGB. ..	77

LIST OF ACRONYMS

AGB	Above Ground Biomass
AFCS	Aboveground Forest Carbon Stock
BA	Basal Area
CO ₂	Carbon Dioxide
DBH	Diameter at Breast Height
DEM	Digital Elevation Model
DLR	German Aerospace Center
DN	Digital Number
ESA	European Space Agency
FAO	Food and Agricultural Organization
GIS	Geographic Information System
Ha	Hectare
HH	Horizontal Send, Horizontal Receive
HV	Horizontal Send, Vertical Receive
IPCC	International Panel on Climate Change
JAXA	Japan Aerospace Exploration Agency
MRV	Monitoring, Reporting and Verification
ALOS-2	Advanced Land Observation Satellite-2
PALSAR-2	Phased Array Synthetic Looking Aperture Radar-2
PES	Payment for Ecosystem Services
RADAR	Radio Detection And Ranging
RMSE	Root Mean Square Error
SAR	Synthetic Aperture Radar
SNAP	Sentinel Application Platform
SRTM	Shuttle Radar Topographic Mission
UNFCCC	United Nation Framework Convention on Climate Change
UN-REDD+	United Nations Reducing Carbon Emissions from Deforestation and Forest Degradation
UTM	Universal Transverse Mercator

1. INTRODUCTION

Forests have an inevitable role in the carbon cycle of the globe and thus, in the global climate (Pan et al., 2011; Wright, 2005). Forests sequester and store carbon in their biomass and exchange it with the atmosphere through deforestation, forest degradation, and regrowth. Carbon storage in the aboveground biomass (AGB) may range from 47 to 50% by region and the types of forests (Thapa et al., 2015).

The mangrove forests are one of the key contributors to the global carbon budget for their role in carbon sequestration and storage. Mangrove ecosystem covers 15.6 million ha in the tropical and sub-tropical areas and is situated in the transition zone between the land and the sea. This location of the mangroves produces cumulative benefits of carbon storage, which can be more significant than other ecosystems (Barbier et al., 2011). In fact, mangroves sequester four times more carbon per unit area compared to the terrestrial forests in the tropics (Donato et al., 2011). Therefore, mangrove forests are of utmost importance when it comes to global climate regulation.

However, mangroves are one of the most threatened ecosystems and feature a rapid decline worldwide. One-third of the global mangrove forest has been lost over the last 50 years as a result of deforestation and degradation (Alongi, 2002). The amount of carbon released through the loss of mangroves amounts to 24 million tons of CO₂ per year- equivalent to the annual emissions of Myanmar (Hamilton & Friess, 2018). In terms of global contribution to emissions, carbon emissions from deforestation and forest degradation have been estimated at 20% of global anthropogenic CO₂ emissions each year from the tropical forests (Gibbs and Herold, 2007; FFPRI, 2012; Ho Tong Minh et al., 2016). However, mangrove deforestation alone accounts for around 10% emissions, despite accounting for just 0.7% of the tropical forest area (van der Werf et al., 2009; Giri et al., 2011).

This dire situation initiated the need to reduce carbon emission from deforestation and forest degradation in the tropical forests including mangrove forests and eventually led the United Nation Framework Convention on Climate Change (UNFCCC) to initiate UN-REDD program (Combes et al., 2009; UNFCCC, 2010). United Nations Reducing Carbon Emissions from Deforestation and Forest Degradation (UN-REDD+) program was initiated in 2008 as a key driver to reduce carbon emissions from forests (FAO, 2018a). The UN-REDD+ initiative aims at reducing carbon emission through performance-based credits by comparison of performance against a business as usual reference emission level. The countries need to prove an increase in forest biomass to claim the credits under the UN-REDD+ program (Solberg et al., 2014).

To this end, UN-REDD+ proposes the need of an accurate Measuring, Reporting, and Verification (MRV) system for AGB estimation (Gibbs et al., 2007) and subsequent monitoring of forest carbon pool (Lucas et al., 2015). However, estimates of AGB should be measurable, transparent, verifiable, and consistent over the time for the MRV system. To achieve this goal, a universal, low cost and robust way to measure and monitor carbon stocks over the vast regions in the tropics is needed (Grassi et al., 2008). Therefore, UN-REDD+ recommends the use of different RS techniques such as very high-resolution satellite images, L-band SAR images (backscatter) and Lidar to assess AGB and above ground forest carbon stock (AFCS) accurately (FFPRI, 2012).

However, it is very challenging to assess AFCS/AGB accurately as it varies from region to region (Shimada et al., 2014) and types of the forests (Thapa et al., 2015). Several methods have been developed for AGB/AFCS estimation including destructive measurement, non-destructive measurement, and forest growth models over the last few decades (Lucas et al., 2015). Among them, the destructive method provides higher accuracies. However, its applications are impractical over the large forest areas as this method is time-consuming, expensive and labor intensive. Also, this method is not applicable particularly in the tropics including the mangrove forests due to inaccessibility.

Alternatively, ground-based carbon inventories have gained a degree of consensus as for the best method for estimating AGB in the tropics. However, measuring tree parameters over large forest areas for carbon inventories is not realistic, especially in the tropics due to inaccessibility, cost and time consideration (Brown, 1997; Chave et al., 2009; Phillips et al., 2006). Eventually, RS techniques appear to be more suitable to predict forest AGB at larger scales with reasonable efforts (Villard et al., 2016). With RS techniques, models are used for scaling up ground-based measurements and monitoring changes over large and regional scales (Reuben, 2009). Therefore, UN-REDD+ also recommends the use of different RS techniques to assess AGB for MRV (FAO, 2018b; FFPRI, 2012).

Over time, both passive (e.g., optical) and active (e.g., Radar and Lidar) RS have been used to map AGB/AFCS (Cutler, et al., 2012; Kelsey & Neff, 2014; Kurvonen, et al., 1999; Lucas et al., 2015; Singh, et al., 2014). However, estimation of AGB with reasonable accuracy is a main challenge due to the saturation of the optical sensors at a low level of the spectral bands (Lucas et al., 2015). Optical RS systems are further limited in the tropics by cloud cover. On the contrary, active RS such as Radar can penetrate clouds and provide data day and night (Asner, 2001). Therefore, active RS (Radar/Lidar) emerged as potential tools for measuring AGB with high accuracy in the tropics (Hyde et al., 2007; Joshi et al., 2015; Kaasalainen et al., 2015).

RS data acquired from Lidar proved to measure AGB with higher accuracy using tree height and DBH (Duncanson et al., 2010). However, acquisition of Lidar data is restricted to sophisticated technical equipment, for instance, airborne or terrestrial laser scanner over the small area coverage (Rahman et al., 2017; Liang et al., 2016). Moreover, it is costly (Kaasalainen et al., 2015). Furthermore, airborne Lidar cannot penetrate through the clouds rendering its application in the tropics.

On the contrary, Radar signals can penetrate forest canopy, and they are not affected by cloud cover, rain or atmospheric contaminants. Therefore, it is becoming increasingly useful for measuring AGB/AFCS in the tropics on a large scale. The longer wavelength L and P- bands of Radar are important bands for AGB estimation because their backscatters are related to volume scattering from tree canopy, branches and trunks enabling more biomass estimation (Mermoz et al., 2014; Villard et al., 2016). However, spaceborne P-band SAR is not currently available, and data is only available from airborne P-band SAR, limiting its application on a large scale in the tropical forests.

L-band SAR has been widely used to estimate AGB of the terrestrial forest in the tropics, and the findings of these studies depict AGB estimation with higher accuracy (Nga, 2010; Odipo et al., 2016). Few studies also attempted to estimate AGB of the mangrove forest using L-band SAR (Hamdan et al., 2014; Pham & Yoshino, 2017; Pham et al., 2017; Pham et al., 2018). However, the accuracy of AGB estimation varies mostly from lower to a moderate level. This study, therefore, aims to model AGB/carbon stock using L-band ALOS-2 PALSAR-2 data in the mangrove forest at Mahakam Delta, East Kalimantan, Indonesia.

1.1. Problem Statement and Justification

Mangrove is a unique and complex ecosystem, flooded during high tide and the ground is a layer of dense mud, with soil containing high levels of organic materials during low tide (FAO, 2007). Mangrove forest has zonation where the types of plants change with different water and salinity level moving away from the sea towards the inland. All these unique attributes in the mangrove forests lead to uncertainty in estimating AGB with high accuracy and low cost. As a result, this has partly resulted in difficulties to assess AGB for MRV mechanism of UN-REDD+ program following a unique methodology in diverse forests regions in the tropics including mangroves.

Most of the studies on AGB/carbon stock estimation in mangrove forests have been done using optical images (Du et al., 2012; Dube & Mutanga, 2015; Gibbs et al., 2007; Lu et al., 2004; Powell et al., 2010). However, mangrove forests are situated in tropical and sub-tropical regions, thus affected by cloud condition for most of the year, making it difficult to obtain clear passive optical images from the satellite (Asner, 2001). In contrast, L-band SAR is an active sensor which can be used in all weather conditions, making it more reliable for accurate estimation of AGB/carbon stock (Omar et al., 2015).

L-band SAR backscatter is depicted to estimate higher AGB with reasonable accuracy in the terrestrial forests in the tropics (Odipo et al., 2016). On the contrary, the use of L-band SAR for AGB estimation are surprisingly lacking for the mangroves, although mangroves have high carbon assimilation and flux rates (Bouillon et al., 2008; Chmura, et al., 2003; Komiyama, et al., 2008; Kristensen, et al., 2008). Until today, a few studies have been conducted to estimate AGB in the mangrove forest using L-band SAR backscatter data (Hamdan et al., 2014; Pham & Yoshino, 2017; Pham et al., 2017; Pham et al., 2018). Again, the accuracy of AGB estimation in these studies is lower than that of inland forests in the tropics. In this context, we studied the relationship between PALSAR-2 backscatter coefficients and AGB in the mangroves of Mahakam Delta, in East Kalimantan, Indonesia to examine if backscatter coefficients of PALSAR-2 can estimate AGB with higher accuracy in the mangrove forest.

The findings of our study may prove a way forward towards a system using L-band SAR for modeling and estimating AGB in the mangroves with reasonable accuracy. Therefore, it may promote the implementation of REDD+ and Payment for Ecosystem Services strategies (PES), thus providing practical implications for developing regional and national Blue Carbon trading markets and guiding mangrove management and conservation.

1.2. Research Objectives

This study aims to model AGB/carbon stock of mangrove forest using the cross (HV) and/or like (HH) polarized ALOS-2 PALSAR-2 data in part of East Kalimantan, Indonesia

Specific Objectives are:

1. To assess the relationship between mangrove forest parameters viz. DBH, BA, and tree height with the HV and/or HH polarized ALOS-2 PALSAR-2 backscatter coefficients.
2. To assess the relationship between field-measured AGB/carbon stock of mangrove forest and HV and/or HH polarized ALOS-2 PALSAR-2 backscatter coefficients.
3. To assess the AGB/carbon saturation point in the mangroves in relation to ALOS-2 PALSAR-2 backscatter coefficients.
4. To estimate and map AGB/carbon stock in the mangroves using ALOS-2 PALSAR-2 backscatter coefficients.

1.3. Research Questions

Objective 1: To assess the relationship between mangrove forest parameters viz. DBH, BA, and tree height with the HV and/or HH polarized ALOS-2 PALSAR-2 backscatter coefficients.

RQ 1: What is the relationship between mangrove forest parameters (DBH, BA and tree height) and ALOS-2 PALSAR-2 backscatter coefficients?

Objective 2: To assess the relationship between field-measured AGB/carbon stock of mangrove forest and HV and/or HH polarized ALOS-2 PALSAR-2 backscatter coefficients.

RQ 2: What is the relationship between HV and/or HH backscatter of ALOS-2 PALSAR-2 and AGB/carbon stock in the mangrove?

Objective 3: To assess the AGB/carbon saturation point in the mangroves in relation to ALOS-2 PALSAR-2 backscatter coefficients.

RQ 3: What is the saturation point of AGB/carbon stock estimation in the mangrove forest in relation to the ALOS-2 PALSAR-2 backscatter coefficients?

Objective 4: To estimate and map AGB/carbon stock in the mangroves using ALOS-2 PALSAR-2 backscatter coefficients.

RQ 4: what is the AGB/carbon stock in the study area and how to map it?

1.4. Research Hypothesis

Objective 1:

H_0 = There is no significant relationship between the mangrove forest parameters and HV and/or HH ALOS-2 PALSAR-2 backscatter coefficients.

H_1 = There is a significant relationship between the mangrove forest parameters and HV and/or HH ALOS-2 PALSAR-2 backscatter coefficients.

Objective 2:

H_0 = There is no significant relationship between HV and/or HH backscatter of ALOS-2 PALSAR-2 and AGB in the mangrove.

H_1 = There is a significant relationship between HV and/or HH backscatter of ALOS-2 PALSAR-2 and AGB in the mangrove.

Objective 3:

H_0 = There is no significant effect of ALOS-2 PALSAR-2 backscatter saturation in AGB estimation in the mangrove forest.

H_1 = There is a significant effect of ALOS-2 PALSAR-2 backscatter saturation in AGB estimation in the mangrove forest.

1.5. Assumptions

The relationship is linear between HV and/or HH backscatter of ALOS-2 PALSAR-2 and field-measured AGB in the mangrove forest in the study area at Mahakam Delta.

2. LITERATURE REVIEW

2.1. Radar

Radar (Radio Detection and Ranging) is a technique to detect remote objects by transmitting the electromagnetic wave to the targets and observing the returned reflection (Appendix 1A) and basically, it is a radio echo (Emery & Camps, 2017). Radar uses the microwave part of the electromagnetic spectrum, from a frequency of 0.3 GHz to 300 GHz, or 1 m to 1 mm wavelength (Lee & Pottier, 2009). In contrast to optical RS that uses the naturally emitted microwave energy to detect objects, radar has its own source of energy as in Appendix 1B (Emery & Camps, 2017).

Radar, being an active RS system, is independent of solar illumination and thus, capable of day and night imaging (Lee & Pottier, 2009). Moreover, it operates in the microwave region of the electromagnetic wave avoiding the effects of clouds, fog, rain and smokes (Lee & Pottier, 2009). Also, some features are better seen in radar images such as ice and ocean waves, soil moisture, vegetation mass, human-made objects like building and geological structures (Emery & Camps, 2017).

2.1.1. Synthetic Aperture Radar (SAR)

The imaging SAR is a radar system between P-band and Ka-band in the microwave region as illustrated in Appendix 2 (Lee & Pottier, 2009). A SAR system comprises of a microwave transmitter, an antenna for both transmission and reception, and a receiver and is placed on an airplane, UAV, space-shuttle, or satellite platform (Lee & Pottier, 2009). It is a side-looking system that illuminates perpendicular to the flight line direction (Lee & Pottier, 2009). SAR imaging geometry is shown in Appendix 3.

SAR has been widely used to monitor land surfaces because of its own source of energy, penetration to the ground surface, day-night and all-weather imaging capability (Moreira et al., 2013). It transmits electromagnetic pulses as it moves and successively, records the backscattered signal (Ager, 2011). The received backscatter detects the objects and determines its position, and the range from the SAR antenna to the objects is determined using the travel time of the electromagnetic pulse (Ager, 2011).

There are both airborne and space-borne polarimetric SAR systems (NASA, 1987). Japanese L-band SAR was first launched on JERS-1/SAR in 1992 and later inherited on the ALOS/PALSAR in 2006 (JAXA, 2009), then on the ALOS-2/PALSAR-2 in 2014 (JAXA, 2016). ALOS PALSAR is a type of spaceborne polarimetric SAR system 2006 (JAXA, 2009). A brief description of ALOS PALSAR is given in the following sections.

2.1.1.1. ALOS PALSAR

Advanced Land Observing Satellite (ALOS) was launched on 24 January 2006 to contribute to the fields of mapping, land coverage observation, disaster monitoring, and resource surveying (JAXA, 2009). Land observation technologies of ALOS was enhanced through the development and operation of its predecessors, the Japanese Earth Resource Satellite-1 (JERS-1) and the Advanced Earth Observing Satellite (ADEOS) enabling it to perform better (JAXA, 2009).

ALOS has three sensors: Panchromatic Remote-sensing Instrument for Stereo Mapping (PRISM), Advanced Visible and Near Infrared Radiometer type 2 (AVNIR-2), and Phased Array type L-band Synthetic Aperture Radar (PALSAR) (ESA, 2015). PRISM is comprised of three sets of optical systems to measure precise land elevation while AVNIR-2 observes the land cover of the earth surface (ESA, 2015).

PALSAR is an active microwave sensor with L-band frequency to acquire cloud-free, all weather and day-and-night land observation (JAXA, 2009). However, ALOS lost communication because of power generation anomaly on 22 April 2011. As a result, JAXA stopped its operation on 12 May 2011 (JAXA, 2016). Technologies of the ALOS operation was succeeded to the second Advanced Land Observing Satellite named ALOS-2 (JAXA, 2016).

2.1.1.2. ALOS-2 PALSAR-2

ALOS-2 carries the L-band Synthetic Aperture Radar (SAR) called PALSAR-2 which was launched on 24 May 2014 (JAXA, 2016). ALOS-2 carries the PALSAR-2 antenna under its body, and there are two paddles of a solar array at both sides of the antenna (Kankaku et al., 2013). The overview of the ALOS-2 is shown in Appendix 4A. ALOS-2 has several unique features such as it has a right and left looking function (Kankaku et al., 2014) which is illustrated in Appendix 4B.

PALSAR-2 has improved observation frequency as the observation range of ALOS-2 expands from 870 km to 2,320 km which is about three times more than ALOS (JAXA, 2016). Eventually, its orbit has a short repeat cycle of 14 days, and orbit control is very accurate (JAXA, 2016). Moreover, the antenna of PALSAR-2 has two-dimension beam steering and dual channel functions (JAXA, 2016). PALSAR-2 has three observation modes Appendix 5. Among them, spotlight observation mode is an improved feature of PALSAR-2 which provides observation with higher resolution (JAXA, 2016). Apart from spotlight mode, there are three Stripmap and three ScanSAR observation modes (JAXA, 2016).

2.2. Polarimetric Backscattering

The polarimetric radar can measure the scattered signals by the target as depicted in Figure 1. The target is illuminated by an incident wave from the Radar (A), and the target scatters the wave in all directions (C) (Natural Resources Canada, 2015a). The radar system receives only a small part of the scattered wave that is returned towards the receiving antenna (B) (Natural Resources Canada, 2015a). The energy received by the radar system is referred to as backscatter (Natural Resources Canada, 2015a).

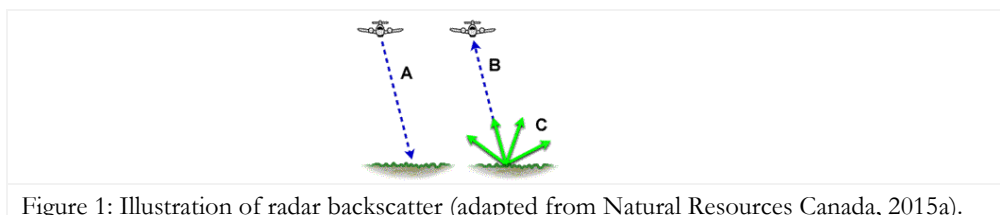


Figure 1: Illustration of radar backscatter (adapted from Natural Resources Canada, 2015a).

There are different types of backscattering such as surface scattering, volume scattering and double-bounce scattering (Evans et al., 1988). The mechanisms of radar backscatter are illustrated in Appendix 6. Volume scattering corresponds to multiple scattering from the targets which can occur in dry soil, sand, ice or vegetation canopy such as forest (Evans et al., 1988).

2.3. Factors affecting Backscattering of SAR

Three factors affect the radar return from the objects. These are the system parameters, topography (slope and aspect) and characteristics of surface materials which includes geometric properties (e.g., surface roughness) and dielectric constant (moisture content) of the objects (Moreira et al., 2013). A brief description of these factors is given in the following sub-sections.

2.3.1. System Parameters

2.3.1.1. Radar Wavelength and Penetration

Radar system operates in a wide range of frequency bands. The band choice influences the imaging of radar and, thus, the information extraction from the objects. The typical wavelength of radar is X, C, L, and P-bands. L-band corresponds to the longer wavelength of 24 cm, whereas C-band and X-band to the shorter wavelengths of 5.6 cm and 3.1 cm respectively (DLR, 2013).

The radar bands can penetrate deeper with the longer wavelength. For instance, when it comes to the forest, the long wavelength L-band can penetrate through the forest canopy and eventually, reach down to the ground underneath the canopy. Therefore, L-band undergoes multiple scattering between the canopy, tree stems and ground surface enabling the Radar system to receive backscatters from all areas of the forest. As a result, L-band Radar corresponds to volume scattering from the forest vegetation (DLR, 2013). On the contrary, short wavelength radar such as X-band penetrate only the top layer of the forest canopy, and thus, backscatters are only reflected from the canopy top (DLR, 2013). The backscattering characteristics of the L band, X band and C are illustrated in Figure 2.

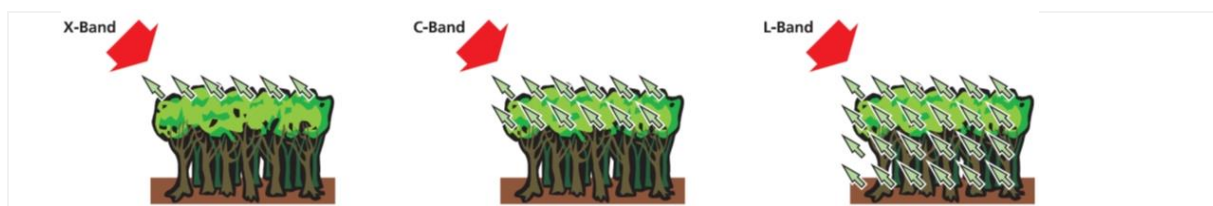


Figure 2: Radar penetration in X-band (3 cm), C-band (5 cm) and L-band (24 cm) wavelengths for forest vegetation (adapted from DLR, 2013).

2.3.1.2. Radar Polarization

The polarization refers to the orientation of the electric vector of an electromagnetic wave in relation to the horizontal direction. When the electric field oscillates parallel to the horizontal direction, the wave is referred to as horizontal (H) polarized. On the other hand, when the electric vector oscillates perpendicular to the horizontal direction, the wave is denoted as vertical (V) polarized (CRISP, 2001).

Radar antennas are configured to emit and receive either horizontal or vertical polarized electromagnetic waves. The electric field vector can be instructed to vibrate in a horizontal or vertical direction when it is sent from the transmitter depending on the antenna design (Natural Resources Canada, 2015b). Two letters usually denote the polarisation of SAR imagery; the first letter indicates the transmitted polarisation and the second letter indicates the received polarisation. Thus, a radar system using H and V linear polarizations can have the following polarization channels (Natural Resources Canada, 2014):

- horizontal transmit and horizontal receive (HH)
- vertical transmit and vertical receive (VV)
- horizontal transmit and vertical receive (HV)
- vertical transmit and horizontal receive (VH)

HH and VV polarizations are denoted as like-polarizations because the transmitted and received polarizations are the same. On the other hand, HV and VH are denoted as cross-polarizations due to the transmitted and received polarizations are orthogonal to each other (Natural Resources Canada, 2014). A Radar system can offer polarization at a different level of complexity such as (Natural Resources Canada, 2014):

- single polarized - HH or VV or HV or VH
- dual polarized - HH and HV, VV and VH, or HH and VV
- four polarizations - HH, VV, HV, and VH

2.3.1.3. Incidence Angle

The angle between the radar illumination and the normal to the ground surface is referred to as the incidence angle. The Radar backscatter from the different types of surfaces varies depending on the incidence angle (Mouginis-Mark, 2001; Emery & Camps, 2017). In general, backscatter from the surfaces decreases with increasing incidence angle. However, the decrease is slow for rough surfaces Appendix 7.

2.3.2. Characteristics of Surface Materials

2.3.2.1. Surface Roughness

Surface roughness is the terrain property that most strongly influences the strength of the radar backscatter and thus, in turn, the brightness of features on the radar imagery (Humboldt State University, 2016). The surface roughness of a scattering surface is relative to radar wavelength and incident angle (Emery & Camps, 2017). A surface is considered smooth if its height variations are considerably smaller than the radar wavelength (Lillesand & Kiefer, 1994). Horizontal smooth surfaces reflect nearly all incident energy away from the radar and are called specular. Calm water bodies or paved highways are specular surfaces and appear dark on the radar imagery (Humboldt State University, 2016).

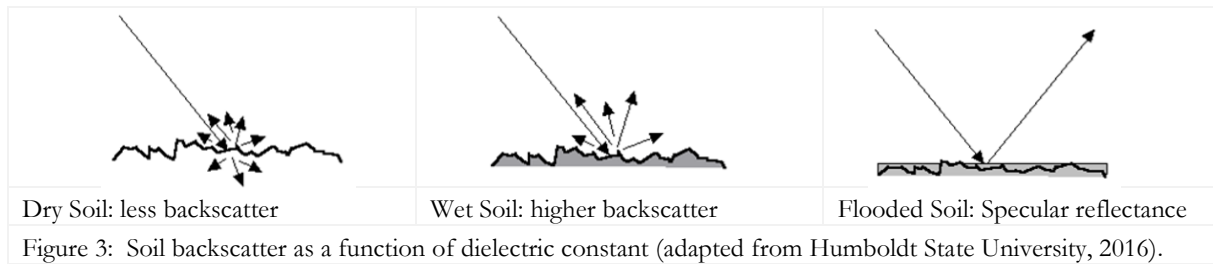
A rough surface is defined as having a height variation of about half the radar wavelength (Lillesand & Kiefer, 1994). Microwaves incident upon a rough surface is scattered in many directions which are known as diffuse or distributed reflectance (Emery & Camps, 2017). For example, vegetation surfaces cause diffuse reflectance and result in a brighter tone on the radar imagery (Humboldt State University, 2016).

When the side of a building or bridge is combined with reflection from the ground, it works as a corner reflector. Buildings are characterized by a relatively simple geometric shape and called discrete scatterers (Humboldt State University, 2016). The diffuse, specular and corner reflectance are shown in Appendix 8.

2.3.3. Dielectric Constant

The dielectric constant can be defined as a measure of the reflectivity and conductivity of a given object. (Humboldt State University, 2016). The dielectric constant of most of the dry materials ranges from 1 to 8 in the microwave region. On the contrary, the dielectric constant of water is around 80 (Humboldt State University, 2016). The moisture content significantly increases the dielectric constant of an object. This, in turn, increases the Radar backscatter, thereby, affects how a target appears on the image (Humboldt State University, 2016).

The dielectric constant of the dry soils is low, and thus, it has low Radar backscatter. On the other hand, wet soil has strong backscatter due to high dielectric constant (Humboldt State University, 2016). A flooded surface acts as a specular reflector, resulting in low backscatter, thus appear dark in the Radar image (Humboldt State University, 2016). The backscattering of different soils is illustrated in Figure 3.



2.3.4. Topography

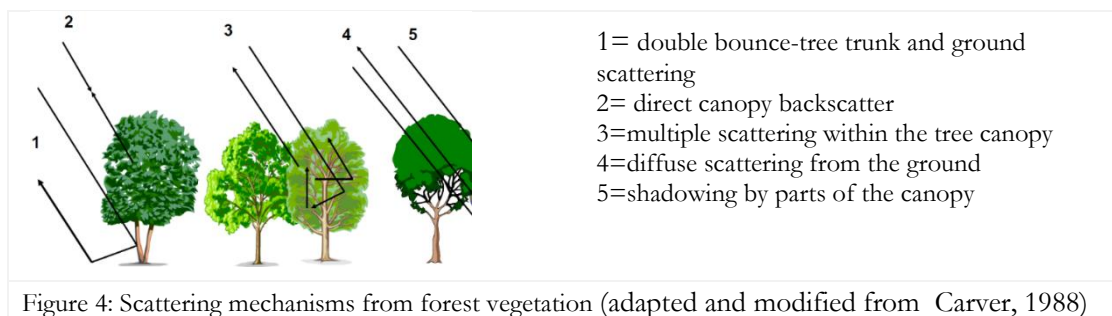
The surface topography plays a vital role in Radar imaging. When it comes to spaceborne Radar, incidence angle changes only a few degrees over the flat surface resulting in a brighter image. However, when the ground surface has a higher slope, the changes in the local incident angle is substantial which results in dark image (ESA, 2002). The effects of local incidence angle on Radar backscattering is shown in Appendix 9.

2.4. Forest and L-band SAR Backscattering

2.4.1. Forest in General

In forestry, the penetration properties of the Radar signals has great significance to model forest AGB (Kumar *et al.*, 2017). The X, C, S, L, and P-bands, as well as the polarisation channels of the Radar system, determines the penetration and backscattering of the Radar system (Hertz, 2008; Lee & Pottier, 2009). In case of relatively short wavelength (i.e., 3 cm for X-band or 6 cm for C-band), the Radar energy is scattered by the foliage and small branches of the canopy (DLR, 2013). Therefore, the SAR energy is reflected mainly from the surface of the canopy at comparatively short wavelength.

On the contrary, the Radar microwave energy with relatively long wavelengths such as L and P-band together with cross polarisation (VH/HV) have depicted their penetration capacities passing through the forest canopy down to the ground surface. This, in turn, results in three main types of radar backscattering namely surface scattering from canopy top and ground surface or single bounce, double bounce (e.g., ground-tree trunk/canopy-ground) and volume scattering (Neumann *et al.*, 2012; Sai *et al.*, 2015). The different types of backscattering at relatively long wavelength are presented in Figure 4. Also, there are some other types of scattering from the forest such as diffuse scattering from the ground. The volume scattering from forest canopy has key importance for forest AGB estimation.



L-band SAR energy is not depolarized when it is scattered from the surface of the canopy, and therefore, there is a strong reflection of like-polarized backscatter. On the other hand, if the SAR energy interacts with the multiple scatterers within the canopy, it is often depolarized, and there is a strong reflection of cross-polarized energy (Jensen, 2007). A SAR image of L or P-band with cross polarization can, therefore, provide information related to forest biomass.

2.4.2. Mangrove Forest

Mangrove forest consists of one or two layers of canopy. The tree height of the mangroves can reach up to 40 m. Mangroves are flooded during high tide, and the ground is a layer of dense mud during low tide (FAO, 2007). Zonation can be found in the mangrove forest from the sea to the inland (Kushan, 2016). The coastal zone is completely inundated up to several meters during high tide and has muddy ground during low tide. Even some areas of the forest can have water surface over the muddy ground during low tide. It is also intersected by numerous water channels including rivers. The schematic diagram of the mangrove forest is given in Figure 5.

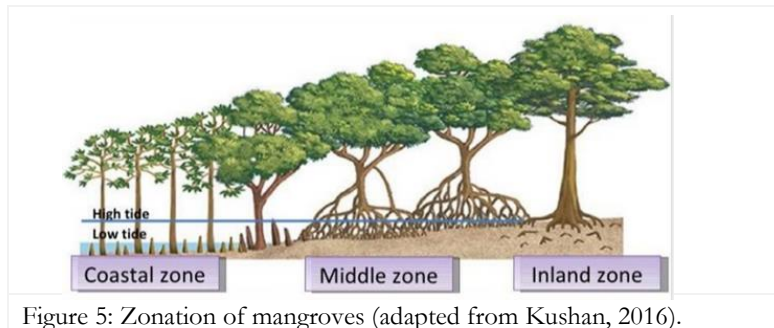


Figure 5: Zonation of mangroves (adapted from Kushan, 2016).

Owing to the structural difference, the scattering of L-band SAR for the mangrove is different than that of the terrestrial forest. Also, zonation in the mangrove forest affects the backscattering of SAR. The scattering from mangrove forest include the volume scattering from the canopy, scattering from canopy to trunk, scattering from tree stems to forest surface, diffuse scattering from the rugged forest floor, specular scattering from inundated water surface and volume to surface scattering at the trunk to surface level (Richards et al.,1987; Manavalan, 2018). The scattering mechanism in a flooded forest is illustrated in Figure 6.

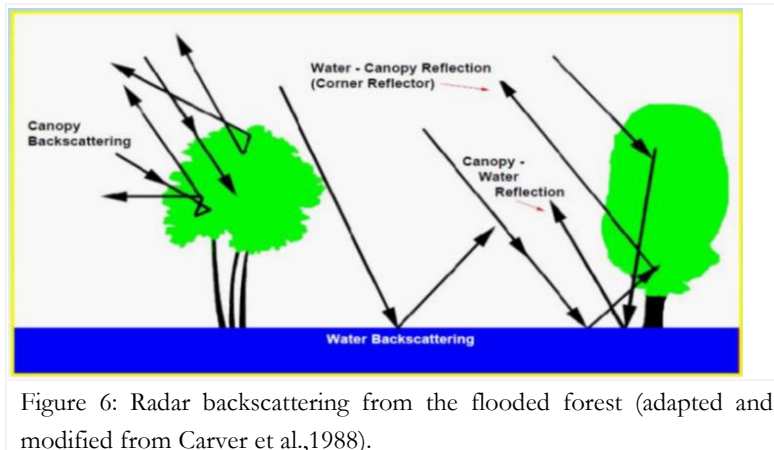


Figure 6: Radar backscattering from the flooded forest (adapted and modified from Carver et al.,1988).

The intensity of such scattering is heterogeneous and varies from one SAR image to another due to the varying nature of vegetation structures and the ground surface. In addition to these vegetation-related scattering natures, the sensor-related factors such as frequency, incidence angle, and polarization of the SAR signals are equally essential to extract information of the mangrove forest.

2.5. Application of L-band SAR for Forest Biomass Estimation

L-band SAR is an only spaceborne system capable of obtaining data at L-band wavelength. Moreover, L-band SAR has the ability of the system to acquire backscatter data in dual and quad polarisation. Therefore; it shows better potential in retrieving the biomass of forests including the sub-tropical and tropical forest.

Several studies have been conducted to estimate AGB and carbon stock using ALOS PALSAR in tropical dry inland forests (Ghasemi *et al.*, 2011; Morel *et al.*, 2011; Hamdan *et al.*, 2011; Carreiras, *et al.*, 2012; Goh *et al.*, 2013; Mermoz, 2014; Thapa *et al.*, 2015). These studies show a strong and positive correlation between forest AGB and cross (HV/VH) polarized backscatter of L-band SAR. The like-polarised backscatter (HH/VV) from the relatively short wavelength X-band and C-band have a weak relationship with AGB/carbon stock (Dobson *et al.*, 1992; Le Toan *et al.*, 1992b)

There is also a saturation problem in AGB estimation using L-band SAR (Mermoz *et al.*, 2014). However, the sensitivity of the L-band SAR to AGB rather depends on the study area due to the influence of forest structure on the relative contribution of the backscattering (Imhoff, 1995; Lucas *et al.*, 2010). Also, the individual contribution to the total forest backscatter is also dependent on dielectric properties of the vegetation and ground surface. The moisture content and the size, geometry, and orientation of leaves, trunks, branches, and aerial or stilt roots also result in a specific backscatter signal (Kuenzer *et al.*, 2011)

2.6. Application of L-band SAR for Biomass Estimation in the Mangrove

Only a few studies have explored the relationships between L-band SAR backscatter and aboveground biomass (AGB) of mangrove forest. For instance, HV polarization of ALOS PALSAR is the best predictor of AGB in the mangroves according to a study in Matang mangroves in Malaysia (Hamdan *et al.*, 2014). A combination of HH and HV backscatter from ALOS-2 PALSAR-2 has also been used to estimate AGB of the two mangrove species (*Sonneratia caseolaris* and *Kandelia obovata*) of Hai Phong city, Vietnam (Pham & Yoshino, 2017). Moreover, machine learning techniques called multi-layer perceptron neural networks (MLPNN) shows the potential for estimation of the AGB of *Sonneratia caseolaris* in a coastal area of Hai Phong city, Vietnam (Pham *et al.*, 2017).

Furthermore, AGB in the mangrove forest in Vietnam is mapped by solving the allometric equations with HV polarimetric measurements of ALOS PALSAR, tree height, DBH and AGB (Takeuchi *et al.*, 2011). In addition, Sentinel-1 C-band SAR data has been used to model AGB estimates of mangrove forest using combinations of polarizations (VV, VH), its derivatives, grey level co-occurrence matrix (GLCM), and its principal component (Argamosa *et al.*, 2018).

Again, a study demonstrates the potential use of integration of SAR data with optical data for estimating AGB of the mangrove forest. For example, ALOS-2 PALSAR-2 data and Sentinel-2A data were integrated to estimate AGB using SVR model in the mangrove forest of North Vietnam. Four variables of ALOS-2 PALSAR-2 data (HH, HV, HV/HH, HH-HV,) and 5 variables from Sentinel 2A (NIR and 4PC1: combination of bands generated from Blue, Green, Red, and NIR multispectral bands) were used for the SVR model to estimate AGB (Pham *et al.*, 2018).

3. MATERIALS AND METHODOLOGY

3.1. Study Area

When it comes to the distribution of mangroves, Indonesia alone accounts for more than 30% of the entire world's mangrove carbon stock (Hamilton & Friess, 2018). However, most of Indonesia's mangrove forests are destroyed or severely degraded, and nearly half of the mangroves have been lost mostly to aquaculture and coastal development during the past 50 years (Kusmana, 2014). Of the 31,894 km² of existing mangrove wetland in Indonesia, 31% are in good condition, 27% are moderately degraded, and the remaining 42% of mangrove forests are heavily degraded (Saputro, 2009).

Despite sheltering almost one-third of the global mangrove forest, information on AGB estimation of mangrove forests is limited in Indonesia. East Kalimantan province has a second-largest area of mangroves in Indonesia. Mangroves in East Kalimantan covers over 11% of Indonesia's total mangrove forest (Hartini et al., 2010). Most of East Kalimantan's mangroves originated from the Mahakam Delta. In Mahakam Delta, mangrove covers nearly 1,500 km². However, most of the mangrove area has been lost mainly due to conversion to fish and shrimp ponds. The total area deforested was estimated to be 85,000 ha in 2001 representing about 75% of the mangrove forest in Mahakam Delta (Zwieten et al., 2006).

In an effort to restore the mangroves in Mahakam Delta, plantation took place since 2002 by both government and private companies at some sites of the Mahakam Delta. However, no studies have been conducted so far to quantify the AGB of the regrowth mangrove in the Mahakam Delta using L-band SAR. Thus, estimating AGB in the mangroves forests of Mahakam Delta using L-band SAR may help to elucidate the spatial distribution patterns of AGB in that region.

The study site was an area of young and reforested mangrove forest in the sea-front areas in north distributary zones of the Mahakam Delta in East Kalimantan, Indonesia. The study was conducted on a mangrove forest since L-band SAR has been less exploited to estimate its AGB/carbon stock though mangrove forest has high potential to sequester more carbon than any other forest ecosystem. The young mangrove forest was chosen as L-band SAR saturates at higher AGB estimates. Also, Mulawarman University, Samarinda, Indonesia provided us with the logistic support and two undergrad students in executing the fieldwork. A brief description of the study area is given in the following subsections.

3.1.1. Geographic Location

The study site covered an area of 105 ha in the mangrove forest located between W longitude 117.560366° to E longitude 117.573216° and N latitude -0.533392° to S latitude -0.543048° at Mahakam Delta, in the East Kalimantan province, Indonesia (Figure 7). East Kalimantan is one of the provinces in the Indonesian part of Borneo Island. It has the second largest area of mangroves representing about 11% of total mangrove forest in Indonesia (Hartini et al., 2010; Susilo et al., 2017). Most of the mangroves of East Kalimantan originated from the Mahakam Delta (Sidik, 2008; Susilo et al., 2017). Mahakam Delta comprises of 46 small islands forming an exceptional fan-shaped lobate and extends to the coastal area of the Makassar Strait of East Kalimantan (Dutrieux, 1991; Zain et al., 2014). It is approximately 20 km from the capital city of East Kalimantan, Samarinda, Indonesia.

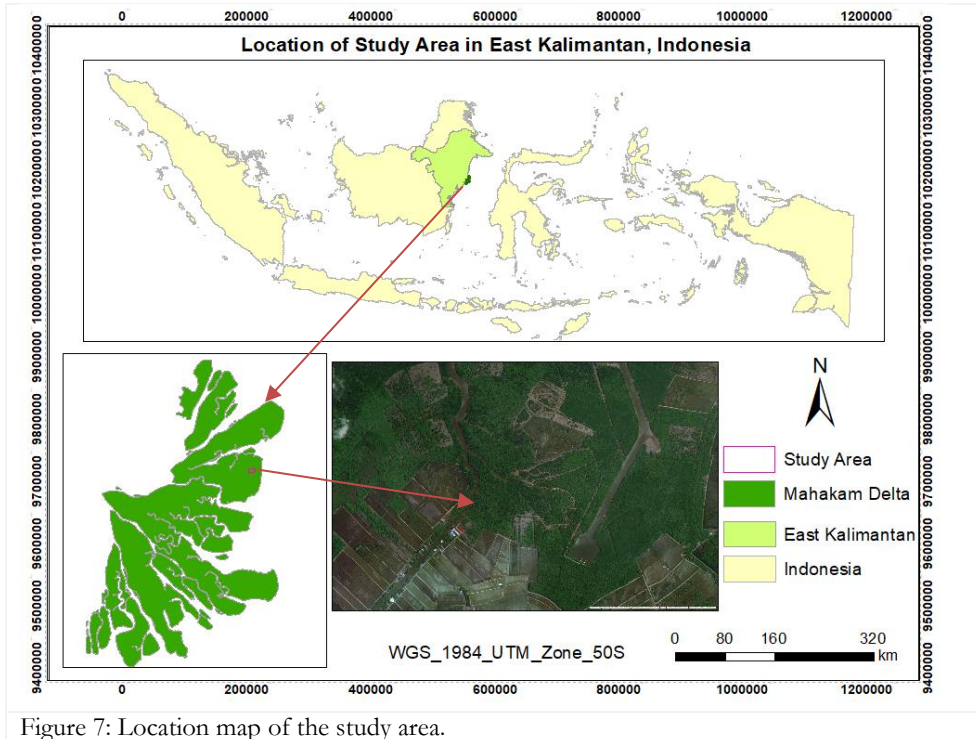


Figure 7: Location map of the study area.

3.1.2. Geomorphology

Mahakam Delta was divided into pro-delta, delta front and deltaic plain based on the geomorphology (Dutrieux, 1991). Pro-delta is part of the delta that borders with the Makassar Strait. *Avicennia* species predominates along with *Rhizophora* and *Bruguiera* species in the pro-delta or sea-front formation. Front delta is the deltaic fringe inundated at high tide and a major area for sediment deposition. The deltaic plain consists of many small islands separated by tributary channels where freshwater from the river and salt water from the sea are mixed (Dutrieux, 1991).

3.1.3. Vegetation and Topography

Mahakam delta has very flat topography with around 0.1% slope. Several vegetation zones can be identified in the mangrove forest of the Mahakam Delta (Sidik, 2008). For instance, the pedada zone is located close to the delta front and is characterized by *Sonneratia alba* and *Avicennia spp.* The bakau (*Rhizophora*) zone is found mostly along the bank of distributaries of the lower delta area. The transition zone is a mixed zone where *Avicennia sp.*, *Sonneratia caseolaris*, *Rhizophora sp.*, *Bruguiera sp.*, *Xylocarpus granatum*, and *Nypa fruticans* grow together. The nibung zone is in the uppermost area of the delta and is characterized by species of *Oncosperma sp.*, *Heritiera littoralis*, *Gruguiera sexangula*, and *Excoecaria agallocha* (Sidik, 2008).

3.1.4. Climate

The location of the Mahakam Delta in equator symbolizes high annual temperature which is constant at 26-28°C with a minimum yearly variation and limited diurnal temperature (Zain et al., 2014). Mahakam Delta has a tropical climate with a relatively dry (May to September) and a wet (October to April) season, dominated by the Monsoons (Sassi et al., 2011). Dry and wet seasons are represented by July and January respectively. April and October depict transitional months. The amount of annual rainfall is more than 2,500 mm in the Mahakam Delta (Bosma et al., 2012).

3.1.5. Tidal Current

Tidal current occurs due to a combination of diurnal and semi-diurnal component and can reach up to 2.5 m height. This tidal current is combined with high current from the Mahakam River at 1,500 m³/sec (Zain et al., 2014).

3.2. Study Materials

Study materials such as software, field equipment, and data are of paramount importance to conduct any research study. The following subsections highlight the materials used in this study.

3.2.1. Field Equipment

Several field equipment was used to collect primary data in the field sample plots. The list of all field equipment and their purpose are explained in Table 1.

Table 1: A list of field study equipment with their purpose.

Field Equipment	Purpose
Diameter Tape	Measuring tree diameter at breast height (DBH).
Leica DISTO D510 laser instrument	Measuring tree height.
Field data sheet and pencil	Record keeping of the field data.
Measuring Tape	Defining the perimeter of the field sample plots.
Garmin GPS	Measuring coordinates of the field sample plots.

3.2.2. Data and Purpose of Use

ALOS-2 PALSAR-2 backscatter coefficients were used to estimate and map AGB in the study area. DBH and height of the trees were measured in the field while the Basal Area (BA) was calculated from field-measured tree DBH. Moreover, wood density was collected from the World Agroforestry Centre (World Agroforestry Indonesia, 2018; World Agroforestry, 2019). These data and their purpose in the study are described in Table 2.

Table 2: A list of data used in this research.

Data	Purpose
ALOS-2 PALSAR-2	To extract HV and HH backscatter coefficients for the field plots and derive their relationship with field-measured AGB, BA, tree DBH and tree height.
DBH	To be used in the allometric equation for calculating field-measured AGB.
Tree Height	To be used in the allometric equation for calculating field-measured AGB.
BA	To derive the relationship between BA and backscatter coefficients.
Wood Density	To be used in the allometric equation for calculating field-measured AGB.

3.2.3. Software

Few software was used for processing and analyzing data in this research. One of them was the Sentinel Application Platform (SNAP) which is an open source software developed for the European Space Agency (ESA). SNAP is a typical platform for all Sentinel Toolboxes (ESA, 2009a). The Sentinel-1 Toolbox (S1TBX) supports an extensive collection of data for processing, display, and analysis from ESA SAR missions as well as third-party SAR data, for example, ALOS PALSAR (ESA, 2009b).

ArcGIS-ArcMap 10.6.1 was used for performing all GIS-based analysis including retrieval of the PALSAR-2 backscatter coefficients. Statistical analysis was conducted using both Microsoft Excel and R programming Language in RStudio. Finally, Microsoft Office was used for writing the report and presentation. Table 3 lists all the software and its application in this study.

Table 3: A list of software used in this research.

Software	Purpose
SNAP	<ul style="list-style-type: none"> ❖ Sub-setting the ALOS-2 PALSAR-2 image for the study area ❖ Pre-processing of ALOS-2 PALSAR-2 data <ul style="list-style-type: none"> • Calibration of PALSAR-2 data, i.e., conversion of DN values to backscatter coefficients • Geometric correction and georeferencing of PALSAR-2 image • Speckle filtering of PALSAR-2 image
ArcGIS	<ul style="list-style-type: none"> ❖ Extraction of backscatter coefficients from PALSAR-2 subset in the field plots ❖ Producing AGB/carbon stock map
R studio	<ul style="list-style-type: none"> ❖ Statistical analysis <ul style="list-style-type: none"> • Correlation analysis • Regression analysis • Model development and validation • Accuracy check (R^2, RMSE and p-value)
Msoffice	<ul style="list-style-type: none"> ❖ Statistical analysis ❖ Report writing ❖ Presentation

3.3. Study Design

This study was designed to estimate AGB using HV and HH polarization backscatter data from ALOS-2 PALSAR-2 in the mangroves of Mahakam Delta in East Kalimantan, Indonesia. Linear regression was used to model AGB in the mangrove forest using the backscatter coefficients of PALSAR-2. The main steps of the study are shown in the flowchart in Figure 8 and briefly described below.

Step 1: This step involved the collection of trees DBH, tree height, wood density, and PALSAR-2 data.

Step 2: The biometric data was processed, and field-measured AGB/carbon stock was calculated using the allometric equation by Chave et al. (2005) in this step. BA was also calculated in this step.

Step 3: This step involved the calibration of PALSAR-2 data in retrieving the backscatter coefficients, geometric correction and georeferencing, and speckle filtering of the PALSAR-2 image.

Step 4: This step included regression analysis between PALSAR-2 backscatter coefficients and forest parameters (BA, DBH and tree height). It also included regression analysis between forest parameters.

Step 5: This step depicted the model development and validation between HV polarization backscatter coefficients of PALSAR-2 and field measured AGB.

Step 6: This step dealt with the saturation point determination of AGB estimation in relation to HV backscatter coefficients of PALSAR-2.

Step 7: This step involved in AGB/carbon stock mapping using the equation derived from the best model in terms of R^2 , and RMSE resulted from step 5.

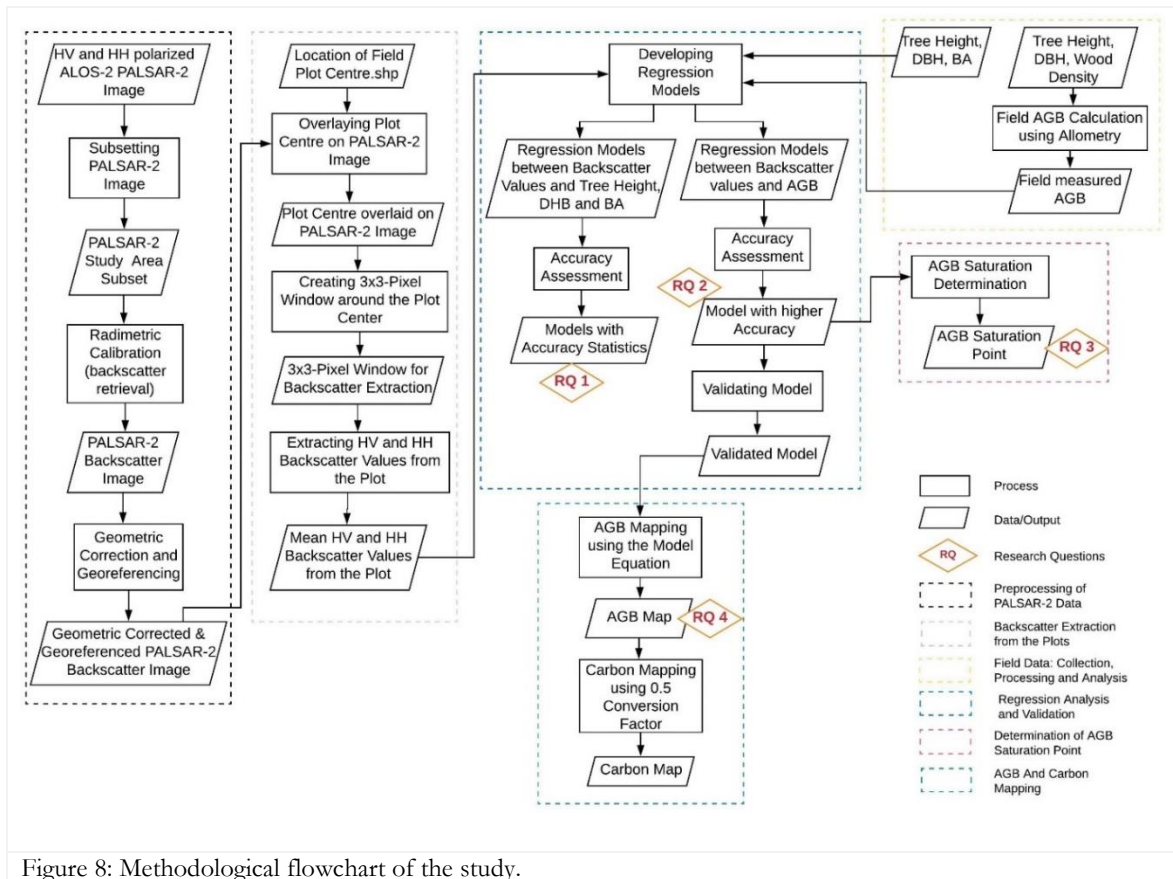


Figure 8: Methodological flowchart of the study.

3.4. Sampling Design

Purposive sampling was used for determining the sample plots in the study area. In total, 71 sample plots were selected. The main reasons for using purposive sampling are as followed.

Accessibility: Sample plots were selected in the study area where it was accessible by the boat through rivers and small water channels. It was very challenging and in some places, impossible to walk through the excessive muddy ground. Therefore, some areas of the mangrove forest were excluded due to the excessive muddy surface.

Time and Cost: Several plots were also chosen in the mangrove forest close to the school (where our team and we were staying during the period of data collection) and accessible by walking to reduce the boat hiring cost. Time was a crucial factor as we had to collect data during peak hours of low tide.

Administrative Permission: Access was restricted in some parts of the mangrove forest in the study area particularly close to an oil company property. Therefore, we selected the sample plots in areas where we had full access from the authority.

3.5. Field Plot Establishment

Although the shape of the plots varies in different studies, circular plots have been used in most of the forest inventories compared to rectangular or square plots (Laar et al., 2007). This is because establishing a circular plot requires to define only one point at its center. Then, the radius of the plot is measured from the center to determine its perimeter. Moreover, the number of trees on the plot borderline is comparatively less in a circular plot. However, four corner points are required to establish a square or rectangular plot which requires more time and labor. Furthermore, more trees fall on the borderline of the square or rectangular

plot. All these induce more systematic error in square or rectangular plot sampling (Kershaw et al., 2016; Laar et al., 2007).

The size of the plot also affects AGB estimation (Luo et al., 2017) and the optimum plot size varies in different regions and types of vegetation (Estornell, 2011). However, AGB estimation was depicted to be the most accurate with the plot size of 500 m² since the plot size > 500 – 600 m² does not significantly improve the result of AGB estimation (Gobakken et al., 2008). Moreover, the plot size of 500 m² was demonstrated as a cost-effective plot size as it tends to sample a reasonable number of trees in each plot (Ruiz et al., 2014). Therefore, a circular plot of 500 m² (0.05 ha) with a radius of 12.62 m was established in our study area. An example of a circular plot with 500 m² is shown in Figure 9.

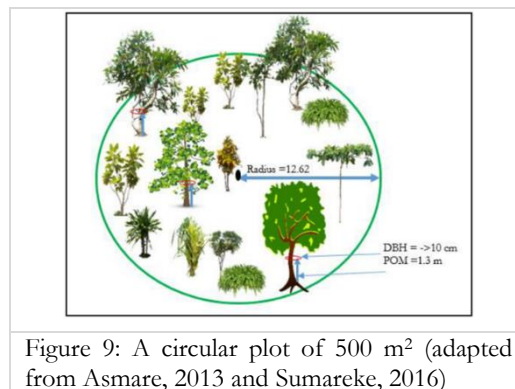


Figure 9: A circular plot of 500 m² (adapted from Asmare, 2013 and Sumareke, 2016)

3.6. Data Collection

3.6.1. Biometric Data Collection from the Plot

The field data were collected from 30 September to 24 October 2018. The circular plots of 500 m² were established using a measuring tape. Then, each tree ≥ 10 cm in diameter was tagged in the plot. This is because trees < 10 cm in diameter have no significant contribution to AGB estimates (Brown, 2002). Therefore, tree height and DBH were measured only for the trees with diameter ≥ 10 cm.

Several tree species were present in the study area. Among them, *Avicennia Alba* and *Rhizophora spp.* were the dominant tree species. There were three species of *Rhizophora* viz. *Rhizophora Stylosa*, *Rhizophora Mucronata*, and *Rhizophora apiculata*. Few species of *Xylocarpus granatum* and *Bruguiera gymnorhiza* were also found in the study area. *Rhizophora spp.* has some unique features such as prop roots extending on the ground. Therefore, DBH and tree height measurements were adjusted for *Rhizophora spp.* taking the prop roots into consideration.

For *Rhizophora spp.*, DBH was measured for the main stem which grows over the prop roots. According to Clough et al. (1997) and Chave et al. (2005), the tree diameter should be measured above the buttress for the trees with prop roots. Therefore, in case of *Rhizophora spp.* the tree DBH is measured at 1.3 m height from the stem base/buttress over the prop roots (Clough et al., 1997). The main stem height over the prop-roots of the *Rhizophora spp.* varies from trees to trees. Measuring DBH at 1.3 height from the buttress represented the tree stem above the uppermost prop-root. Some field photos of DBH measurement of *Rhizophora spp.* are shown in Figure 10.



Figure 10: DBH measurement of *Rhizophora* Species, the measurement was taken at 1.3 m height from the stem base/junction over the prop roots.

However, as far as tree height of *Rhizophora spp.* was concerned, the measurements were taken from the ground, i.e., from the prop roots on the ground to the top of the trees. The reason behind this was that these prop roots cover a large area on the ground as can be seen in Figure 10 as well as in Appendix 10, thus, contribute to the backscattering of the L-band SAR.

In the case of *Avicennia alba* tree species, DBH was measured at 1.3 m height from the ground. The height of 1.3 m was used to minimize the variation in DBH measurement and to be consistent with the point of measurement. Similarly, the tree height was measured from the ground to the top of the trees. The tree height and DBH measurement of *Avicennia alba* tree species are shown in Appendix 11. The measurements for other tree species were similar to *Avicennia alba*. The unit of DBH measurement was “centimeter” (cm) and tree height was “meter” (m).

There were many multi-stem trees of *Avicennia alba* and *Rhizophora spp.* in the study area (

Appendix 12). In this case, each stem of the multi-stem trees was considered as an individual tree (Clough et al., 1997). Accordingly, DBH and tree height were measured separately for each stem of the multi-stem trees.

The coordinates were recorded at the center of each plot using a Garmin GPS. Additional four measurements of coordinates were also recorded at four corners of a plot. All data were recorded in the field data sheet. A datasheet of a plot is shown in Appendix 13.

3.6.2. Wood Density Data Collection from the World Agroforestry Centre

Apart from collecting biometric data from the field, the wood density of the trees was collected from the World Agroforestry and World Agroforestry Indonesia database (World Agroforestry Indonesia, 2018; World Agroforestry, 2019).

3.6.3. Acquisition of ALOS-2 PALSAR-2 Data

The ALOS-2 is an Advanced Land Observation Satellite 2 which carries the Phase Array L-band Synthetic Aperture Radar 2 (PALSAR-2) Sensor on board. ALOS-2 is a Japanese satellite launched by the Japan Aerospace Exploration Agency (JAXA). One dual-polarized (HV and HH) ALOS-2 PALSAR-2 image was acquired from JAXA through the Remote Sensing Technology Center of Japan (RESTEC). RESTEC is responsible for the distribution of RS images from JAXA. The image was acquired by ITC, Faculty of Geoinformation Science and Earth Observation, University of Twente, the Netherlands on 6 December 2018. The specifications of the acquired ALOS-2 PALSAR-2 are given in Table 4.

The mangrove forest in the study area is inundated up to 2.5 m during high tide (Zain et al., 2014). The time of scene observation of the PALSAR-2 image was chosen during peak hours of low tide to minimize the

effects of inundation on the backscattering. The ground surface of the study area mangrove forest during peak hours of low tide is shown in Appendix 14.

Table 4: A detail specification of the ALOS-2 PALSAR-2 data used in this study.

Specifications of ALOS-2 PALSAR-2	Description
Scene Observation Date and Time	30 July 2018 and 16:26:06 (UTC), Local East Kalimantan Time 1:26 am
Product type	FDR 1.1
Product format	CEOS
Observation mode	Stripmap
Observation swath wide	70 km
Process level	1.1
Calibration factor	-83.0
Off-nadir angle	36.6°
Incidence angle at scene centre	40.562°
Pixel spacing	4.29 m
Range spacing	4.29 m
Azimuth spacing	3.42 m
Wavelength	0.2424525 m (24 cm)
Polarization	HV and HH
Range looks x Azimuth looks	1.0 x 1.0
Antenna Pointing	Right Looking
PASS	Ascending
Sample type	Complex

3.7. Data Processing

3.7.1. Field Data Processing

The data on forest parameters were transferred to the Excel sheet. Then DBH, tree height, and wood density were used in the allometric equation for AGB calculation of each tree in the plot. The allometric equation proposed by Chave et al. (2005) for AGB calculation of the mangrove forests was used in our study. In addition, the basal area (BA) of each tree was also calculated in the plot.

The unit of AGB calculation was kg/500 m² in the plot. In the final datasheet, the AGB was converted to ton ha⁻¹. The BA area was calculated in m²/500m². It was converted to m²/ha. Then, average and sum of each parameter viz. DBH, tree height, AGB and BA were calculated for every individual plot. The summary of the forest parameters per plot is presented in Appendix 15.

The coordinates of the plots from Garmin GPS were converted to shapefile in ArcGIS. The center coordinates were exported to a new layer and named as plot center. The buffer was created using 12.62 m radius around the plot center to create the plot area of 500 m². The additional four coordinate points were used to cross-check the position of the plot.

3.7.2. ALOS-2 PALSAR-2 Data Pre-processing

The ALOS-2 PALSAR-2 image was obtained at level 1.1 which is a complex image. Pre-processing of PALSAR-2 image was performed before extracting backscatter coefficients. As part of it, the radiometric calibration was conducted followed by geometric correction and geo-referencing. Filtering was also applied

to remove speckle noise from the image. The pre-processing of PALSAR-2 was performed using software SNAP. A small subset covering the study area was made to reduce the processing time. The study area subset of PALSAR-2 is given in Appendix 16.

3.7.2.1. Radiometric calibration for retrieval of PALSAR-2 backscatter coefficients

PALSAR-2 backscatter coefficients were retrieved by applying radiometric calibration where the DN values of the image were converted to radar backscatter coefficients known as Normalized Radar Cross Section (NRCS) and expressed in decibels (dB). The conversion of DN to NRCS of ALOS-2 PALSAR-2 image for level 1.1 product was done using equation 1 proposed by Shimada et al. (2009).

Equation 1: Retrieval of PALSAR-2 backscatter coefficients/ NRCS.

$$\sigma^{01.1 \text{ product}} = 10 \cdot \log_{10}(I^2 + Q^2) + CF - A$$

Where:

$\sigma^{01.1 \text{ product}}$ = Normalized Radar Cross Section of level 1.1 product in (dB)

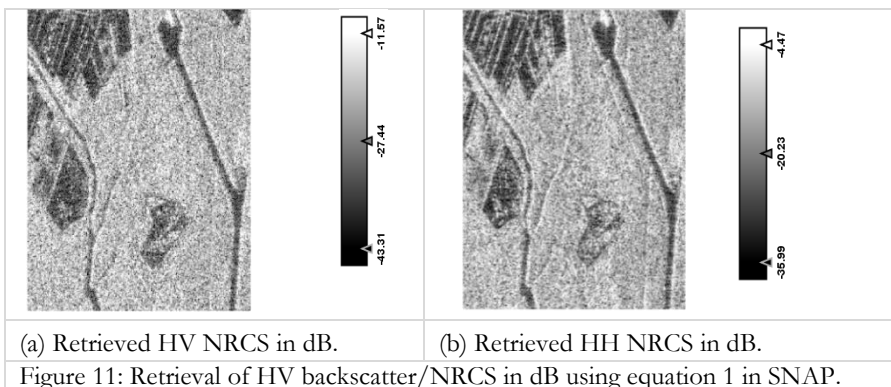
I = Real part of Single Look Complex (SLC) product (level 1.1)

Q = Imaginary part of SLC product (level 1.1)

CF = Calibration Factor = -83.0 dB

A = Constant, 32.0

Equation 1 was calculated using band math in SNAP. The backscatter coefficients were retrieved for cross (HV) and like (HH) polarization of PALSAR-2 data. A snapshot of the retrieved HV and HH polarized images with backscatter coefficients (dB) are depicted in Figure 11. It can be observed from the legend of the image that most of the HV polarization backscatter ranged from -11 dB to -27 dB. The corresponding range for HH polarization backscatter was observed from -4 dB to -20 dB. The ratio and sum of HV and HH polarization backscatter were also derived to explore their response in estimating AGB in the study area.



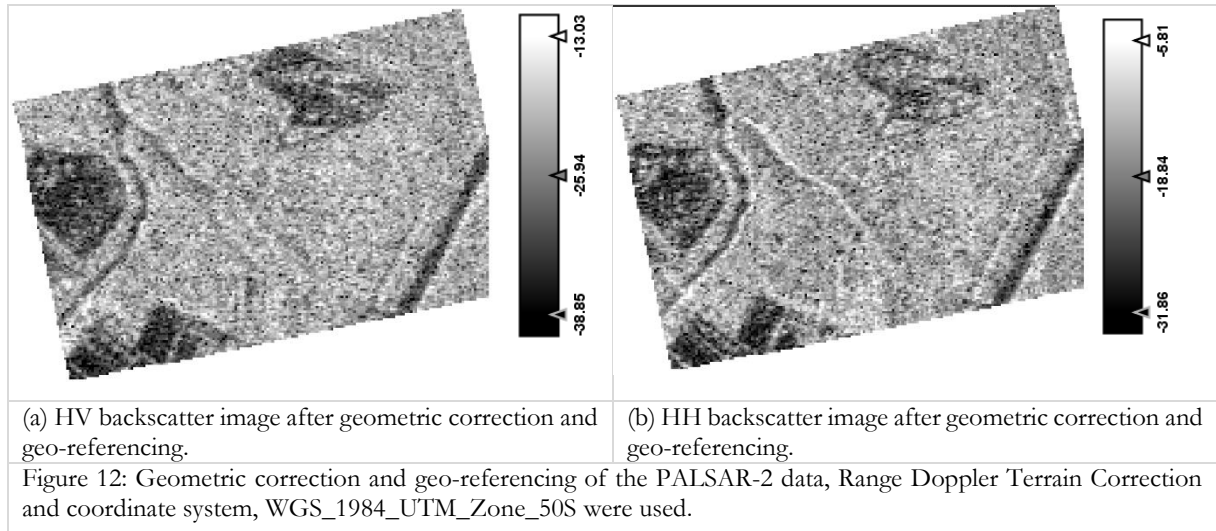
3.7.2.2. Geometric correction and geo-referencing

The single look complex SAR images are geometrically distorted due to the sensors image acquisition not being at Nadir location, tilting of the satellite sensor and image scene topographical variation (Schreier, 1993; Small et al., 2009). Thus, the geometric correction was performed to compensate for these distortions so that the SAR images can represent the real world.

Range-Doppler Terrain Correction was used for the geometric correction of PALSAR-2 image in our study. Range-Doppler determines the location of a pixel in the SAR image by intersecting the centroid of the radar beam and the earth surface (Curlander, 1982). Range-Doppler was used because it is a standard and precise

technique for geometric correction (Jiang et al., 2016). Shuttle Radar Topography Mission (SRTM) DEM (30 m) was used for the Range-Doppler Terrain Correction of the PALSAR-2 image. In our study, SRTM-1 was used because it was higher resolution DEM provided in SNAP software. After geometric correction, the pixel spacing of the PALSAR-2 image is 7 m.

Then, PALSAR-2 image was re-projected to Universal Transverse Mercator (UTM) coordinate system to have a true projection. The coordinate system: Zone 50S (WGS_1984_UTM_Zone_50S) was used for the study area in East Kalimantan, Indonesia. The geometric corrected HV and HH backscatter images along with their legends are shown in Figure 12.



3.7.2.3. Filtering of the PALSAR-2 data

L-band SAR data have a characteristic of salt and pepper like appearance. The salt and pepper appearance or speckle noise can influence the relationship between forest parameters and SAR backscatter coefficients (Joshi et al., 2015). Speckle filtering smoothens the speckle noise on the image. In our study, a Lee speckle filter with a kernel size of 3 by 3 pixels was applied on the PALSAR-2 image after it was geometrically corrected. The speckle filtered images are shown in Appendix 17.

3.7.3. PALSAR-2 Data Processing

3.7.3.1. Extraction of the PALSAR-2 backscatter coefficients from the plots

After pre-processing, the backscatter coefficients were extracted for each plot in the study area for further analysis. The plot had 12.62 m radius, so the diameter of the whole plot was about approximately 25 m ($12.62+12.62= 25.24$ m). On the other hand, the PALSAR-2 image had a pixel size of $7 * 7$ m. Therefore, the plot approximately fitted with 3 by 3 pixels window with a diameter of 21 m ($3*7m=21m$). A similar approach was followed in previous studies (Hamdan et al., 2014; Masolele, 2018; Sumareke, 2016).

The 3 by 3 pixels window was chosen so that the window can approximately cover the plot area (diameter of 25.24m) and avoid smoothing out the average backscatter within a plot. The window of 4 by 4 pixels or 5 by 5 pixels reduces the error of excluding backscatter from the trees within the plot, but it tends to smoothen out the average backscatter within the plot (Sumareke, 2016).

Our study area presents mangrove forest with many intersecting water channels including the Mahakam River. Thereby, the PALSAR-2 signals had specular reflectance from the water channels, i.e., no energy back to the sensor. Also, the muddy ground surface was covered by water in some parts of the study area even

during peak hours of low tide. This also caused specular reflectance in some areas. As a result, the window of 5 by 5 pixels or 4 by 4 pixels showed the possibility to include the nearby dark water pixels and thereby, smoothen out the average backscatter within the plot. Some pictures of the water channels/river/muddy ground covered by water near the sample plots are shown in Appendix 18.

The plot centers were overlaid on the PALSAR-2 image in ArcGIS. Around the plot center, a polygon was created with the 3 by 3 pixels for each plot. Thus, 71 polygons were created for 71 plots, and later these were combined into one shapefile. The establishment of the 3 by 3 pixels window to cover the plot area is illustrated in Figure 13.

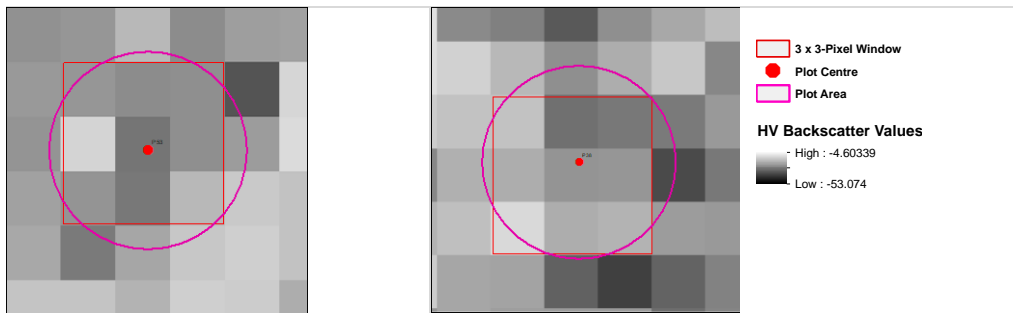
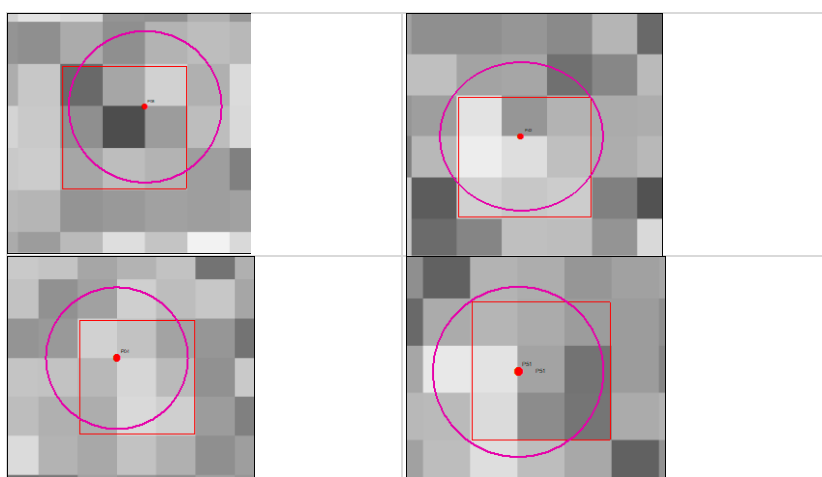


Figure 13: Establishment of the 3 by 3 pixels for extraction of backscatter values from the plot.

The average backscatter coefficient for 3 by 3 pixels window was extracted using zonal statistics under spatial analyst tool in ArcGIS. The polygons of 3 by 3 pixels window were linked to the Plot_ID following the Plot_ID of the coordinates of the plot center. This is to note that all the field-measured data had the same Plot_ID and accordingly, the window of 3 by 3 pixels window was also linked to the same plot. As a result, the extracted backscatter coefficients from the 3 by 3 pixels window were associated with the field-measured data. This was important to be able to analyze the relationship between the field-measured data and backscatter coefficients.

However, not all the plot centers perfectly fitted inside the center of 3 by 3 pixels window. Some plot center points fell between the edge of two pixels. Some of the plot centers were also found at the intersection of four pixels. It created a problem to identify the center of the pixel, thus placement of the 3 by 3 pixels window for the plot. This has been illustrated in Figure 14.

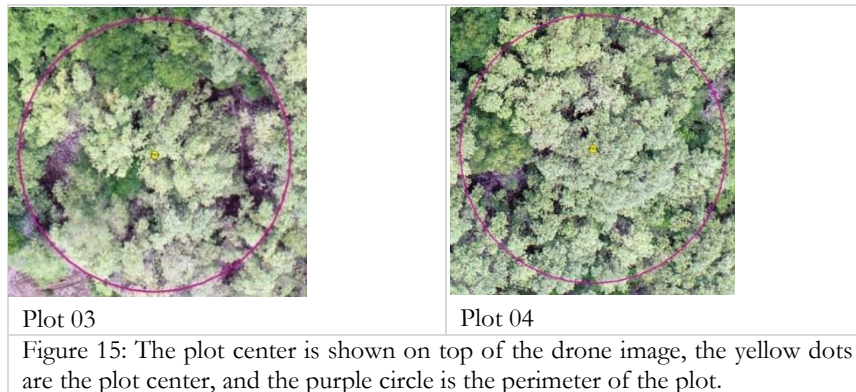


(a) Plot center at the intersection of four pixels.

(b) Plot center at the edge of two pixels.

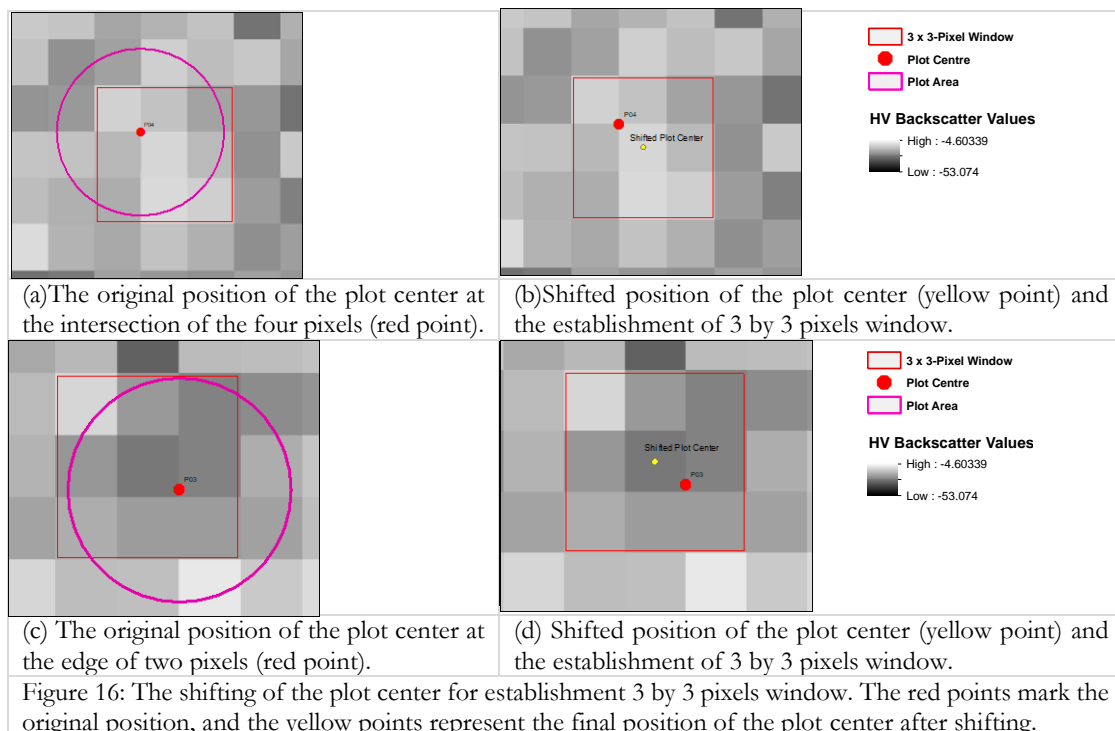
Figure 14: Location of plot center between two or more pixels.

A visual interpretation technique was adopted to address this issue. The plot centers and plot area buffers were overlaid on the drone images collected during the period of our data collection for other studies. The example of drone images with overlying plot 3 and plot 4 are presented in Figure 15.



Drone images provided information on the canopy density of the plot and major species types as well as the position of the plot. The ground photos of the plot taken during data collection were also used to support the visual analysis with the drone images. Based on this analysis, plot center at the intersection of four pixels/at the edge of two pixels was shifted to the most suitable pixel among the shared pixels, and then the window of the 3 by 3 pixels was established. The shifting of the plot center of plot 3 and plot 4 and subsequent establishment of their 3 by 3 pixels window is illustrated in Figure 16. The ground photos of these plots (plot 3 and plot 4) are given in Appendix 19.

The dimension of 3 by 3 pixels covered 9 pixels of the PALSAR-2 image. An average value of the extracted backscatter coefficients within the 9 pixels was used for AGB model development and validation. NRCS/backscatter coefficients were the predictor or estimator for the field-measured AGB.



3.8. Analysis

3.8.1. Plot AGB Calculation

AGB was calculated using tree DBH, tree height and wood density data in an allometric equation proposed by Chave et al. (2005) for the mangrove forests. AGB was calculated for each tree in each plot. The allometric equation used for AGB calculation is given in equation 2.

Equation 2: Allometric equation for calculation of AGB.

$$\text{Mangroves, AGB} = 0.0509 \rho D^2 H$$

Where: AGB = aboveground biomass estimated in kilogram

D = diameter at breast height in centimeter

ρ = wood density in gcm^{-3}

H = tree height in meter

The total AGB was calculated for individual plots using equation 2 in kilogram per 500 m^2 plot. Then, it was converted to tons per hectare using equation 3.

Equation 3: AGB calculation in tons per ha.

$$\text{AGB (tons/ha}^{-1}\text{)} = (\text{Total AGB (kg/plot)} * 20)/1000$$

3.8.2. Plot Carbon Calculation

Carbon was calculated from the AGB using the conversion factor of 0.5 and is expressed in tons ha^{-1} . The conversion factor may vary from plant to plant, species to species and site to site (Abdul Rashid et al., 2009). Therefore, the global default conversion factor of 50% was used to convert AGB to carbon stock followed by the Intergovernmental Panel on Climate Change (IPCC, 2007). The equation to calculate carbon using the conversion factor of 0.5 is given in equation 4.

Equation 4: Calculation of carbon stock using conversion factor.

$$C = \text{AGB} * \text{CF}$$

Where: C is the carbon stock in tons ha^{-1}

AGB is the aboveground biomass in tons ha^{-1}

CF is the carbon fraction (0.5)

3.8.3. BA calculation

The cross-section of the tree stem at 1.3 m breast height is defined as the basal area (BA) of the tree. The tree BA in a plot was calculated following the formula by Larsen (2018) which is given in equation 5.

Equation 5: Calculation of BA.

$$\text{BA} = 0.00007854 * (\text{DBH})^2$$

Where: 0.00007854 is the constant of π

BA is the basal area per tree in square meter (m^2)

DBH is the diameter at breast height in centimeter

The total BA was calculated in the plot in m^2 per 500 m^2 plot. It was converted to m^2 per hectare dividing it by 0.05. BA per hectare was calculated as it is considered as a measure of stocking density of a forest stand and was correlated to the backscatter coefficients of PALSAR-2.

3.8.4. Correlation Analysis

Correlation analysis is essential to be performed to test the strength and direction of correlation between the variables. The correlation coefficient values range between -1 and +1. The value -1 indicates that there is a very strong negative correlation between two variables, and +1 indicates that there is a very strong positive correlation between the variables. A value of 0 indicates that there is no correlation between the variables (Stein et al., 1999).

In our study, correlation analysis was performed to test if a correlation exists between forest parameters (i.e., AGB, BA, DBH and tree height) and backscatter coefficients of PALSAR-2 before applying the regression analysis. The Pearson product-moment correlation was used because it measures the strength and direction of the association between two variables measured on an interval/ratio scale. The measurement scale of our data is a ratio. Therefore, Pearson product-moment correlation analysis was performed between AGB and the PALSAR-2 backscatter coefficients. Moreover, the correlation was performed for BA, DBH and tree height with PALSAR-2 backscatter coefficients. The correlation between AGB and the other forest parameters (BA, DBH, tree height) was also performed.

3.8.5. Regression Analysis

Regression models are the most commonly used models to analyze the relationship between one dependent variable and one or more independent variables (Quinn & Keough, 2002). Linear regression was the most commonly used method for estimating the AGB of mangrove forest in previous studies (Hamdan et al., 2014; Hirata et al., 2014; Pham & Yoshino, 2017). However, the performance of these models was relatively low at R^2 ranging from 0.43 to 0.65 in the three studies mentioned above. Machine learning approach (SVR) was also used by Pham et al. (2018) to estimate AGB in the mangrove forest, but, it also resulted in a low performance with R^2 of 0.596.

We used linear regression to analyze the relationship between field-measured AGB and backscatter coefficients of PALSAR-2 because a linear correlation was observed between our data from correlation analysis. We analyzed the relationship between the field measured AGB and HV, HH polarized PALSAR-2 backscatter coefficients separately using simple linear regression technique. We also investigated if there is a significant improvement on AGB estimation if multiple regression analysis is performed with both HV and HH backscatter coefficients. The accuracy of the linear regression analyses was compared based on the value of R^2 , RMSE, and p-value. Furthermore, the relationship between PALSAR-2 backscatter coefficients and other forest parameters such as BA, DBH and tree height was analyzed using linear regression analysis. The relationship of AGB with BA, DBH and tree height was also explored using linear regression technique.

The backscatter coefficients from the highest performing regression analysis were used to develop a regression model which, in turn, used to estimate and map AGB/carbon stock in the study area. The requirements of performing linear regression analysis between the variables (Quinn & Keough, 2002; Moore et al., 2017) were also verified for the best performing regression in our study. It was done to confirm if our data for estimating AGB/carbon stock fulfills the criteria for the linear regression analysis. Based on the accuracy of the regression analysis, the simple linear regression between HV backscatter coefficients and field-measured AGB yielded the highest performance. Thus, the requirements of the linear regression between HV backscatter and field-measured AGB were tested in our study. These are listed below:

Distribution of the regression data: If the data is normally distributed, most of the observations are found around the mean with very few outliers. In this case, it is very tricky to fit any linear trend in the data and perform a linear regression. Therefore, linear regression needs a uniform distribution of the data, not the normal distribution (Quinn & Keough, 2002; Moore et al., 2017). We used Normal Q-Q plot, and then

performed Shapiro-Wilk test for the testing the distribution of field-measured AGB and HV backscatter according to Altman & Bland (1995) and Field (2009).

A quantile-quantile (Q-Q) plot is a scatterplot created by plotting two sets of quantiles against one another to assess whether a dataset follows a theoretical distribution such as a normal distribution. If both quantiles follow the normal distribution, it forms almost a straight line (Altman & Bland, 1995; Field, 2009).

Shapiro-Wilk is a statistical technique that is a commonly used method for normality test. It is based on the correlation between sample data and the corresponding theoretical normal scores. It calculates a W statistic to test the normality of the data. If the p-value is <0.05 , it implies that data deviates from a normal distribution (Shapiro & Wilk, 1965).

Distribution of the errors/residuals: The residuals of a linear regression follow a normal distribution where residuals cluster more along the regression line. Shapiro-Wilk statistical technique (Shapiro & Wilk, 1965) was used to test the normality of the residuals.

The constant variance of the residuals: The variance of the residuals of the regression are constant over the independent variables. The scatterplot of the regression with the line of best fit was visually analyzed to check if the residuals are constant.

Sum and mean of the residuals is zero: The residuals of the linear regression sum up to zero and have a mean of zero.

3.8.6. Regression Model Development

Using the 60:40 ratio, the 71 plots were split randomly into two datasets: model development dataset and validation dataset. 60% of the data was used for model development and 40% for model validation. The model and validation plots on the PALSAR-2 image are shown in Appendix 20.

The regression analysis depicted the best prediction accuracy of AGB using HV polarized PALSAR-2 backscatter coefficients whereas the prediction was very poor using HH backscatter coefficients. The multi-linear regression analysis showed no improvement of AGB prediction accuracy; rather it was almost the same as a simple linear regression with HV backscatter. Therefore, the linear regression model was developed between the HV backscatter of PALSAR-2 data and field measured AGB. The prediction equation derived from the model was used to estimate AGB and carbon stock of the whole study area. The relationship between HV backscatter and field measured AGB using linear regression function can be expressed as in equation 6.

Equation 6: Linear regression function between HV backscatter coefficients and field-measured AGB.

$$AGB = \beta_0 + \beta_1 HV$$

Where,

AGB = the predicted AGB

β_0 = the intercept

β_1 = the model coefficient for HV

3.8.7. Model Validation

A validity check was performed to measure the prediction accuracy of the regression model. The predicted AGB derived from the model equation was correlated with the field-measured AGB from the 40 plots. The coefficient of determination, R^2 , and RMSE were used to test the accuracy of the model validation. RMSE was calculated using equation 7 according to Deng et al., (2014)

Equation 7: Equation for RMSE calculation.

$$RMSE = \sqrt{\frac{\sum_{i=1}^n (\hat{Y} - Y)^2}{n}}$$

Where,

RMSE = the Root Mean Square Error

Y = the biomass calculated using the allometric equation

\hat{Y} = the biomass predicted from ALOS-2 PALSAR-2 backscatter using the model

n = the number of the validation plots

3.8.8. Determination of Saturation Point

In previous studies, the saturation point of AGB was determined using the logarithmic function between SAR backscatter and AGB. The saturation point of AGB was defined as a point where the slope of the logarithmic regression curve started to decrease by 0.02 dB against the minimum-maximum of the AGB (Suzuki et al., 2013). The saturation level was also defined using 0.01 dB on the slope of the SAR backscatter against the AGB (Watanabe et al., 2006).

In our study, the AGB saturation point was calculated along the slope of the logarithmic curve derived from logarithmic regression between HV backscatter and AGB where the slope started to decrease by 0.01 dB using slope equation 6.

Equation 8: Determination of AGB saturation point using slope between changes in HV backscatter coefficients and changes in AGB.

$$\text{Slope} = \Delta Y / \Delta X \quad (\text{Suzuki et al., 2013; Watanabe et al., 2006}).$$

Where: ΔY is the change in HV backscatter values with respect to the minimum HV value

ΔX is the change in AGB with respect to the minimum AGB value.

First, we determined the points where the slope of the logarithmic curve started to decrease by 0.01 dB and 0.02 dB against the AGB. Then, we visually analyzed both points on the regression curve against the range of AGB. The visual analysis depicted that AGB had a clear pattern of leveling off on the slope of the logarithmic regression curve at 0.01 dB whereas the slope at 0.02 dB, AGB continued to increase. Therefore, we defined the saturation level of AGB when the slope of the logarithmic regression curve decreased to 0.01 dB.

3.8.9. AGB/Carbon Stock Mapping

An AGB/carbon stock map was produced for the study area based on the AGB estimation using the equation derived from the simple linear regression model between the HV backscatter of the PALSAR-2 image and field-measured AGB. Raster calculator tool in the Spatial Analyst toolbox in ArcGIS software was used for mapping the AGB/carbon stock. The model equation was applied on the HV backscatter image where every pixel value from HV backscatter image was converted to AGB following the equation. A similar approach was followed in previous studies for AGB mapping in the mangrove forest (Hamdan et al., 2015). A carbon stock map for the study area was also created from the AGB map using a conversion factor of 0.5 (IPCC, 2007). A separate group was formed for the negative AGB values because they represent specular reflection from the river and water channels.

4. RESULTS

4.1. Descriptive Analysis of the Study Data

4.1.1. Description of the Tree Species

Tree species were identified in the sampling plots during fieldwork. The number of individual tree species measured in the field plots totaled at 2407. Among them, *Avicennia alba* was the most dominating tree species accounting for 60% of all individual trees. It was followed by *Rhizophora spp.* at 38%. The *Rhizophora spp.* composed of *Rhizophora apiculata*, *Rhizophora stylosa*, and *Rhizophora murconata*. Few *Xylocarpus granatum* and *Bruguiera gymnorhiza* were also found in some plots. The percentage distribution of the tree species is presented in Figure 17.

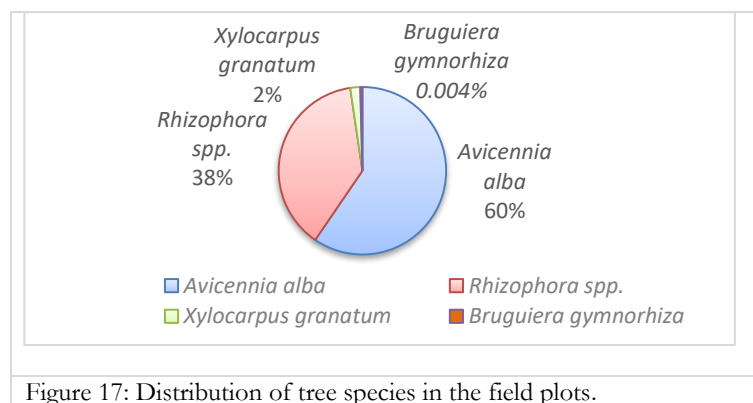


Figure 17: Distribution of tree species in the field plots.

4.1.2. Descriptive Statistics of the Study Parameters

The forest parameters used in this study were tree DBH, tree height, AGB, and BA. These parameters were measured from 71 plots in the mangrove forest of the study area. The mean DBH in all the plots was accounted for 16.81 cm while the mean tree height stood at 14.15 m. The mean AGB and mean BA was calculated at 136.30 tons ha⁻¹ and 18.02 m² ha⁻¹ respectively for all plots.

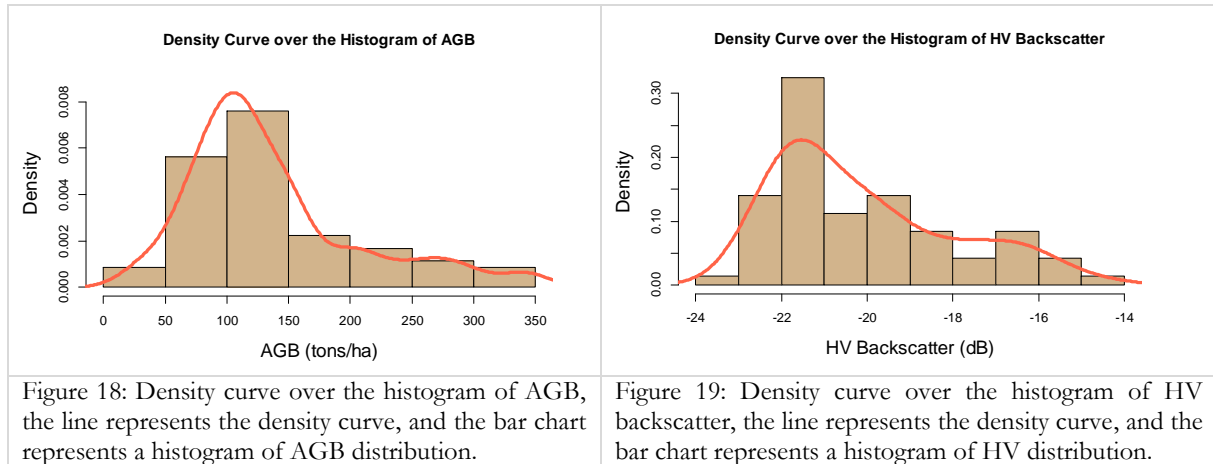
The mean HV and HH backscatter coefficients of PALSAR-2 were extracted from the plots to study their relationship with AGB and other forest parameters. The mean HV backscatter coefficients accounted for -20.09 dB whereas the mean HH backscatter coefficients were -13.82 dB. The descriptive statistics of all the study parameters from the plots are listed in Table 5.

Table 5: The descriptive statistics of all the study parameters.

Parameters	Min	Max	Sum	Mean	Std. Error of Mean	Std. Deviation
AGB (tons ha ⁻¹)	28.30	346.20	9677.60	136.30	8.41	70.87
BA (m ² /ha)	4.28	40.92	1279.39	18.02	0.93	7.82
Mean DBH (cm)	11.90	22.93	-	16.81	0.33	2.81
Mean Height (m)	10.54	18.25	-	14.15	0.22	1.82
Wood Density (g/cm ³)	0.70	0.91	55.72	0.79	0.01	0.05
Mean HV (dB)	-23.01	-14.54		-20.09	0.25	2.09
Mean HH (dB)	-25.86	-9.11		-13.82	0.31	2.63

4.1.3. Distribution of AGB and HV Backscatter using Density Curve over the Histogram

The distribution of AGB and HV backscatter coefficients is shown in Figure 18 and 19 using their histogram and density curve. The density curve visualizes the AGB and HV backscatter distribution where data points can take any value in the continuum and denotes what percentage of the data points falls into a category. The area under the curve equals 100% or 1.0.

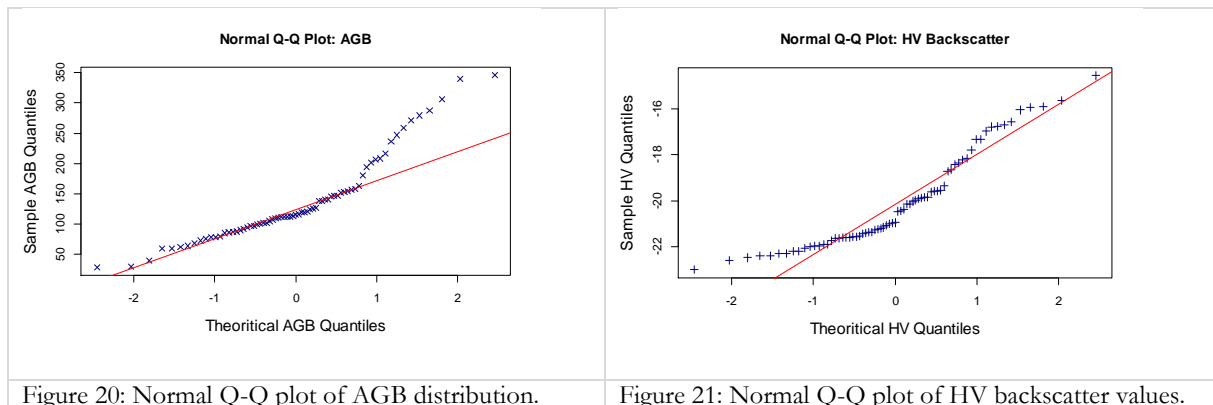


From the distribution of AGB in Figure 18, it can be seen that most of the AGB values fell between 50 tons ha^{-1} and 150 tons ha^{-1} . The density of field-measured AGB peaked at the point on the density curve where the AGB values stood at around 100 tons ha^{-1} . It indicates that the AGB had the highest frequency at approximately 100 tons ha^{-1} .

From the distribution of HV backscatter coefficients in Figure 19, it can be observed that HV backscatter peaked on the density curve where the HV backscatter lies between -21dB to -22 dB. It implies that most of the HV backscatter values ranged from -22 dB to -21 dB.

4.1.4. Normality Test of AGB and HV Backscatter using Normal Q-Q Plot and Shapiro-Wilk Test

The Normal Q-Q plot of AGB (Figure 20) shows that the AGB values were left-skewed at higher values. It can also be observed from the Normal Q-Q plot in Figure 21 that HV backscatter coefficients were right skewed in the middle and left skewed at the higher and lower range of the values. The skewness indicates that data were not normally distribution.



Then, we performed Shapiro-Wilk (Shapiro & Wilk, 1965) test for the testing the field-measured AGB and HV backscatter coefficients for normality. The results of the Shapiro-Wilk normality test showed a W statistic at 0.89067 with a p-value of 1.495E-05 for the field-measured AGB. The p-value was < 0.05 ;

therefore, distribution of the field- measured AGB was significantly different from the normal distribution. In other words, the field- measured AGB was not normally distributed.

We also conducted a Shapiro-Wilk normality test for the HV backscatter coefficients. The test depicted a W statistic of 0.90321 and a p-value of 4.629E-05. This means that HV backscatter values were not normally distributed.

4.2. Correlation Analysis between Backscatter Coefficients and Forest Parameters

Initially, the correlation analysis was conducted between AGB and speckle filtered HV polarization backscatter coefficients. However, the correlation was poor at r of 0.64 (and R^2 of 0.41). The results of the correlation analysis between AGB and speckle filtered HV backscatter coefficients are shown in Appendix 21.

After inspecting the speckle filtered and non-speckle filtered PALSAR-2 image, it was observed that the AGB pixel values from the mangrove forest and water pixel values from river and water channels were averaged during the filtering process. It smoothed out the true HV backscatter of the forest biomass.

Therefore, we performed a correlation analysis between non-speckle filtered HV backscatter and field-measured AGB. The results showed a very strong correlation between non-speckle filtered HV backscatter coefficients and field-measured AGB. Therefore, non-speckle filtered HV backscatter coefficients were used for all analysis in this study and referred to as HV backscatter coefficients. Similarly, non-speckle filtered HH backscatter coefficients were referred to as HH backscatter coefficients.

Pearson's product-moment correlation was used to test the correlation of forest parameters (AGB, BA, DBH and tree height) with HV as well as HH backscatter coefficients. The correlation coefficient, r , was used to observe the strength of correlation. From the results of correlation analysis (Table 6), it can be observed that HV backscatter had a very strong correlation with field-measured AGB at r of 0.94. The BA also showed a strong correlation with HV backscatter ($r=0.89$). The correlation between DBH and HV backscatter had a reasonable correlation at r of 0.71. On the other hand, the tree height depicted a moderate correlation with HV backscatter at r of 0.50. The correlation of HH backscatter was weak with all the forest parameters.

Table 6: The correlation analysis between forest parameters and backscatter coefficients of PALSAR-2.

Pearson Product moment correlation Statistic	Forest Parameters	AGB	BA	DBH	Tree Height
	Backscatter				
Correlation coefficient (r)	HV	0.94	0.89	0.71	0.50
Sig (2 tailed)		< 2.2e-16	< 2.2e-16	3.334e-12	8.6e-06
t-value		23.207	15.859	8.4254	4.8083
95% CI		0.9075497 0.9632286	0.8225377 0.9274690	0.5741995 0.8107202	0.3031003 0.6574398
Correlation coefficient (r)	HH	0.34	0.32	0.28	0.22
Sig (2 tailed)		0.003276	0.006054	0.01715	0.0623
t-value		3.0468	2.8322	2.4425	1.8949
95% CI		0.1207533 0.5347018	0.09668932 0.51708554	0.05223825 0.48358034	-0.01149487 0.43322963

Moreover, the correlation analysis between AGB and other forest parameters (BA, DBH and tree height) was conducted. The results showed that AGB was highly correlated with BA at r of 0.95. The correlation between AGB and DBH was moderate whereas the correlation was quite poor between AGB and tree height. The results of these analyses are given in Appendix 22.

The correlation analysis was also conducted between AGB and the derivatives of HV and HH backscatter coefficients, e.g., the sum and the ratio of HV and HH backscatter coefficients. The results of the correlation analysis are shown in Appendix 23.

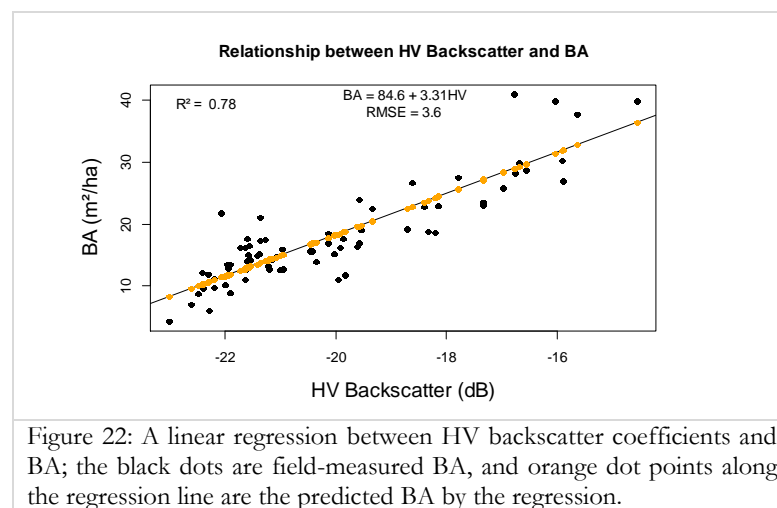
4.3. The relationship between HV Backscatter and BA, DBH & Tree Height

The correlation analysis showed that HV backscatter coefficients are more strongly related to BA, DBH and tree height than HH backscatter coefficients (see Table 6). Therefore, regression analysis was conducted only between HV backscatter coefficients and forest parameters viz. BA, DBH and tree height. The summary statistics of the regression analysis between HV backscatter and BA, DBH & tree height are shown in Table 7.

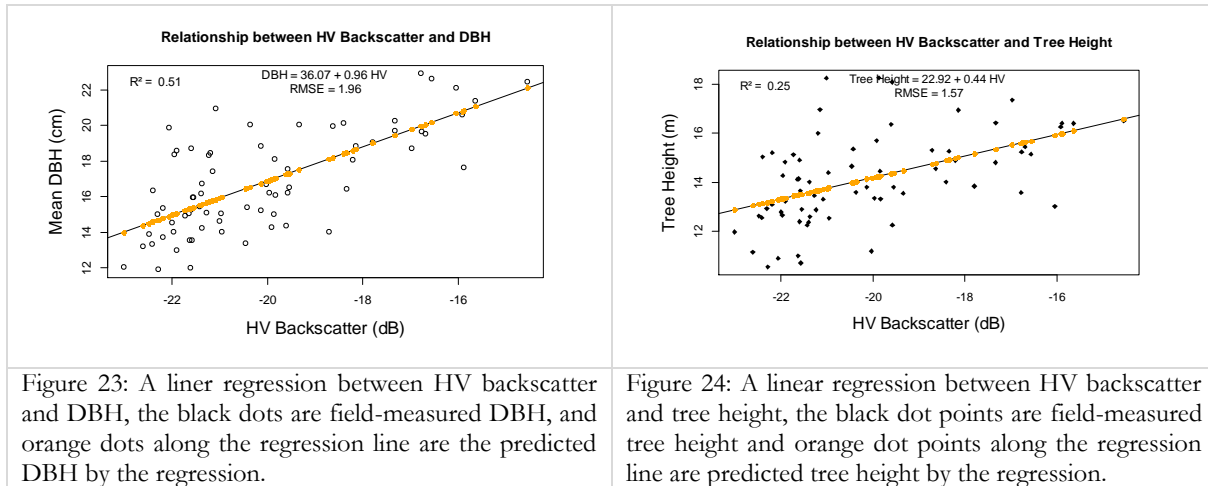
Table 7: Summary statistics of the regression between HV backscatter and BA, DBH & tree height.

Regression Statistics		BA	DBH	Tree Height
R ²	HV Backscatter	0.784724037	0.507096787	0.250978601
RMSE		3.60m ² ha ⁻¹	1.96cm	1.57m
Standard Error		3.652834511	1.988882955	1.587867871
F-stat		251.5188309	70.98691452	23.12019859
Significance F		1.04777E-24	3.3336E-12	8.59979E-06
Coefficients: Intercept		84.59710894	36.06663242	22.92362348
P-value: Intercept		1.74369E-30	1.83897E-24	2.18081E-19
Coefficients: HV		3.314654909	0.958785475	0.436850877
P-value: HV		1.04777E-24	8.425373257	8.59979E-06

From the summary statistics of the regression analysis in Table 7, it can be observed that HV backscatter had a strong relationship with BA at R² of 0.78. This means that HV backscatter coefficients explained 78% variation in BA. The RMSE of the regression stood at 3.60 m² ha⁻¹. The scatterplot of the regression between HV backscatter and BA is given in Figure 22.



The results of the linear regression between DBH and HV backscatter depicted a reasonable accuracy at R^2 of 0.51. This means that HV backscatter explained 51% variation in DBH. The scatterplot of the regression analysis between HV and DBH has been shown in Figure 23. On the contrary, the performance of the regression analysis between tree height and HV backscatter was poor at R^2 of 0.25 implying that HV backscatter explained only 25% variation in tree height. The scatterplot of the regression analysis between HV and tree height has been shown in Figure 24.



4.4. Relationship of BA, DBH and Tree Height with AGB

The relationship of AGB with other forest parameters such as BA, DBH and tree height was explored using linear regression analysis. Out of them, the BA depicted a higher accuracy to predict AGB with R^2 of 0.89. The results of the regression between BA and AGB are shown in Figure 25 and Table 8. The accuracy to predict AGB using DBH was moderate at R^2 of 0.55. However, the relationship between tree height and AGB was weak with R^2 of 0.30. The scatterplot and summary statistic of the relationship of AGB with DBH and tree height are presented in Appendix 24 and Appendix 25 respectively.

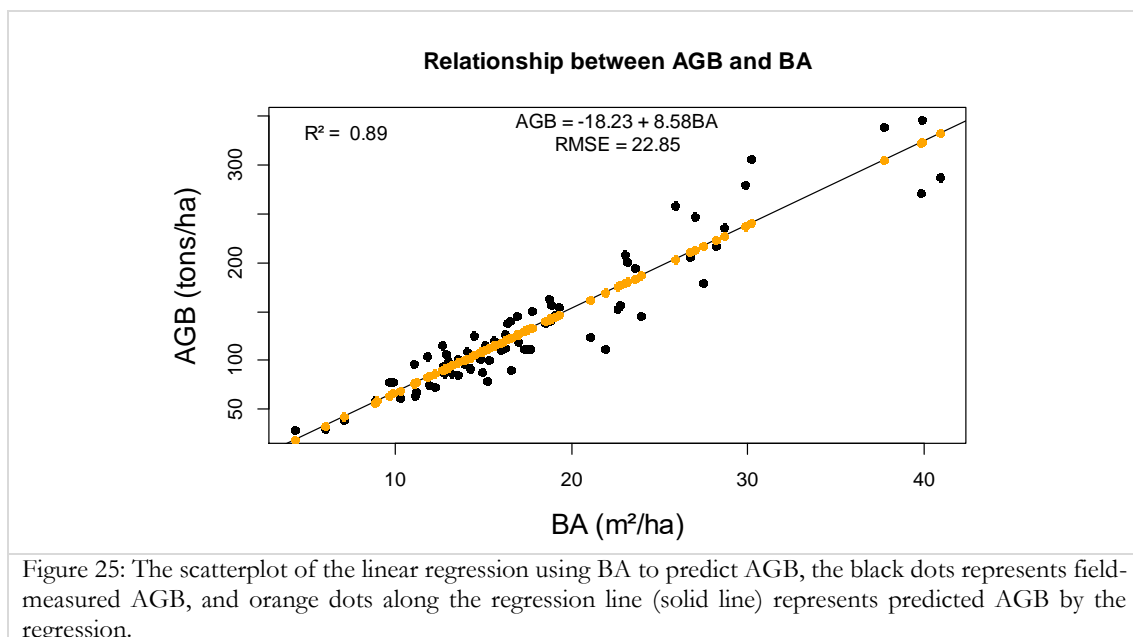


Table 8: Summary statistics of regression between BA and AGB.

<i>Regression Statistics</i>					
Multiple R	0.945809285				
R Square	0.894555204				
Adjusted R Square	0.893027019				
Standard Error	23.18065336				
Observations	71				
<i>ANOVA</i>					
	<i>df</i>	<i>SS</i>	<i>MS</i>	<i>F</i>	<i>Significance F</i>
Regression	1	314544.7431	314544.7431	585.3708424	1.9897E-35
Residual	69	37076.64561	537.34269		
Total	70	351621.3887			
	<i>Coefficients</i>	<i>Std Error</i>	<i>t Stat</i>	<i>P-value</i>	
Intercept	-18.23153298	6.954500778	-2.621544459	0.010760372	
BA	8.575993504	0.354461361	24.19443825	1.9897E-35	

4.5. The Regression between AGB and Backscatter Coefficients

The linear regression was conducted between the field-measured AGB and backscatter coefficients of PALSAR-2. The results of the regression showed that HV backscatter had a higher performance to predict AGB at R^2 of 0.89. However, HH backscatter showed a poor relationship at R^2 of 0.12. The multi-linear regression with HV and HH backscatter had the same performance to predict AGB as the simple linear regression. The sum of HV and HH backscatter had a moderate relationship with AGB at R^2 of 0.55. On the contrary, the ratio of HV and HH showed no relationship with AGB.

Since the HV backscatter showed a higher accuracy to predict AGB, the relationship between HV backscatter and AGB was modeled to estimate AGB in the mangrove forest of the study area using linear regression. Therefore, the requirements of linear regression between HV backscatter and AGB were tested to confirm that the data fit for the model. The results depicted that HV backscatter coefficients and field-measured AGB perfectly fitted for the linear regression analysis. The results of the test are discussed below:

- The HV backscatter coefficients and AGB were not normally distributed which is a requirement of performing a linear regression between the variables. The results of the distribution of HV backscatter and AGB were shown in section 4.1.4.
- The residuals of the regression between HV backscatter and AGB were normally distributed. We performed a Shapiro-Wilk normality test (Shapiro & Wilk, 1965) for testing the normality of the residuals. The results of the Shapiro-Wilk normality test depicted a W statistic at 0.99249 with a p-value of 0.9508. The p-value of 0.95 was > 0.05 , indicating that residuals were normally distributed. The residuals of the regression between HV backscatter and AGB are shown in Appendix 26.
- The variance of the residuals of the regression between field-measured AGB and HV backscatter coefficients were constant over the field-measured AGB values. It means that the residuals of the regression had a constant variation along the line of best fit. This can be observed in the scatterplot of the regression with the line of best fit in Figure 37.
- The mean and sum of the residuals of the linear regression between the field-measured AGB and HV backscatter coefficients were zero.

The results of all the linear regression between backscatter coefficients (HV, HH) and AGB are presented in the following subsections.

4.5.1. The Relationship between HV Backscatter and Field-measured AGB

The linear regression analysis showed a strong relationship between HV backscatter and field measured AGB with R^2 of 0.89 and RMSE of 23.72 tons ha⁻¹ at a p-value of 2.58755E-34. This result depicts that HV backscatter can significantly explain 89% variation in AGB using linear regression. The scatterplot of linear regression between HV backscatter and field-measured AGB is presented in Figure 26 and summary statistics of the regression analysis are given in Table 9.

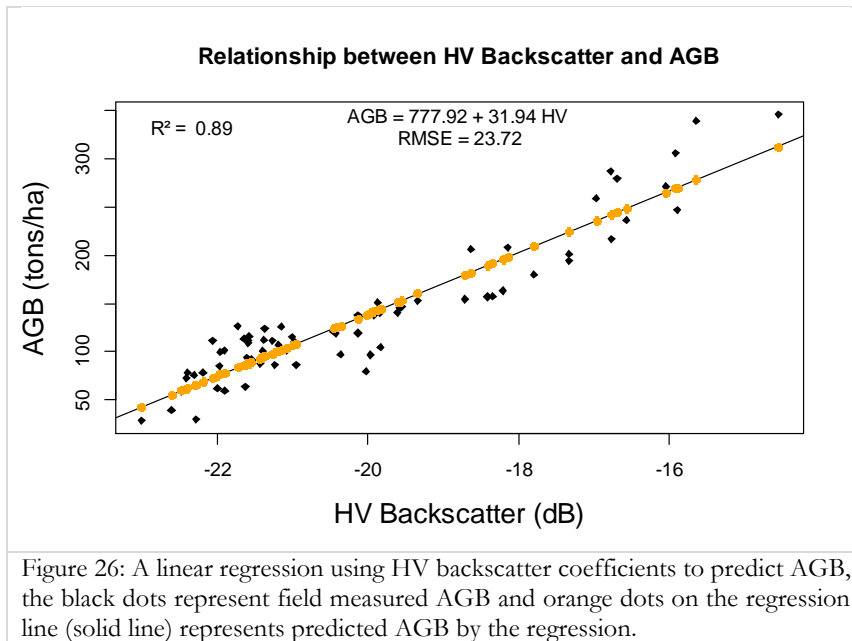


Figure 26: A linear regression using HV backscatter coefficients to predict AGB, the black dots represent field measured AGB and orange dots on the regression line (solid line) represents predicted AGB by the regression.

Table 9: Summary statistics of regression analysis between HV backscatter and AGB.

Regression Statistics					
Multiple R	0.941504298				
R Square	0.886430344				
Adjusted R Square	0.884784407				
Standard Error	24.05715422				
Observations	71				
ANOVA					
	<i>df</i>	<i>SS</i>	<i>MS</i>	<i>F</i>	<i>Significance F</i>
Regression	1	311687.8686	311687.8686	538.5566521	2.58755E-34
Residual	69	39933.52018	578.7466692		
Total	70	351621.3887			
	<i>Coefficients</i>	<i>Std Error</i>	<i>t Stat</i>	<i>P-value</i>	
Intercept	777.916116	27.79457815	27.98805263	2.15299E-39	
HV	31.94353828	1.376471813	23.20682339	2.58755E-34	

4.5.2. The Regression between HH Backscatter and Field-measured AGB

The linear regression between HH backscatter and field-measured AGB showed a very weak relationship at R^2 of 0.12 and RMSE of 66.07 tons ha⁻¹ with the p-value at 0.01. The scatterplot of the regression analysis and the corresponding table of summary statistics are shown in Figure 27 and Table 10.

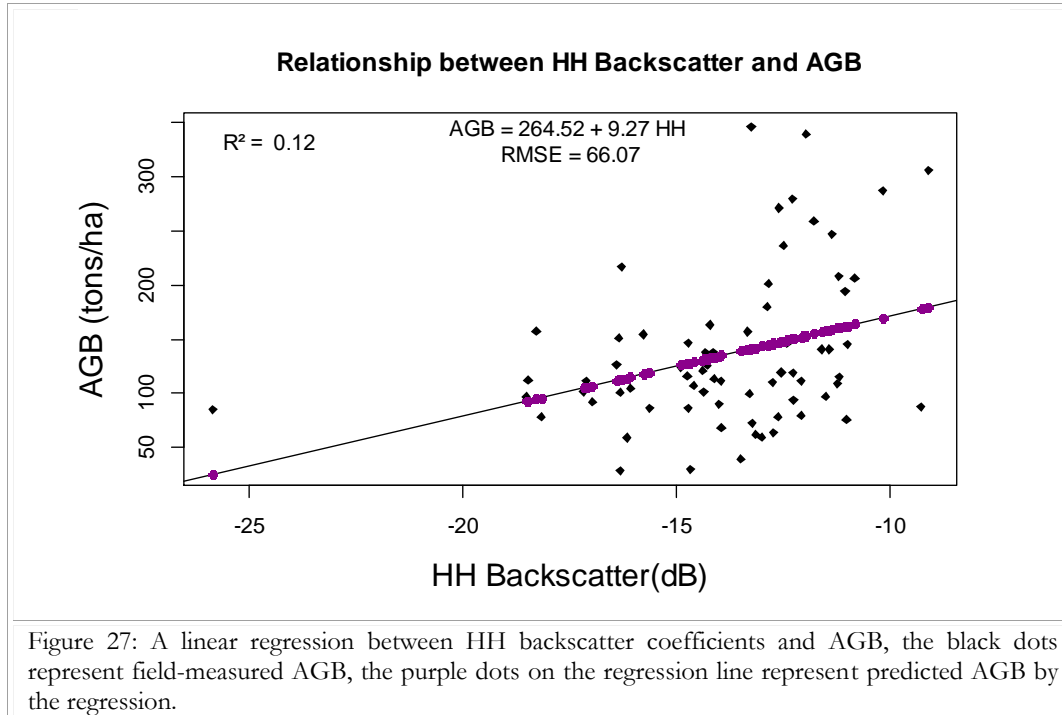


Table 10: Summary statistics of the relationship between HH backscatter and AGB.

Regression Statistics					
Multiple R	0.344355751				
R Square	0.118580883				
Adjusted R Square	0.105806693				
Standard Error	67.01998555				
Observations	71				
ANOVA					
	<i>df</i>	<i>SS</i>	<i>MS</i>	<i>F</i>	<i>Significance F</i>
Regression	1	41695.57475	41695.57475	9.282849403	0.003275817
Residual	69	309925.814	4491.678464		
Total	70	351621.3887			
	<i>Coefficients</i>	<i>Std Error</i>	<i>t Stat</i>	<i>P-value</i>	
Intercept	264.5201521	42.82753998	6.176403133	3.98654E-08	
HH	9.272951288	3.043528171	3.046776888	0.003275817	

4.5.3. The Relationship between the Derivatives of HV and HH Backscatter and Field-measured AGB

The linear regression analysis was performed between the sum of HV and HH backscatter coefficients and field-measured AGB. The results showed that the sum of HV and HH backscatter coefficients had a relationship with field-measured AGB at a coefficient of determination, R^2 of 0.55 and the significance of the relationship was at p-value < 1.33921E-13. This implies that the sum of HV and HH backscatter can

explain 55% variation in AGB. The RMSE of the regression was 47.18 tons ha⁻¹. The scatterplot and summary statistics of the regression analysis are shown in Appendix 27.

The relationship of AGB with the ratio of HV/HH and HH/HV polarized backscatter was analyzed separately using the linear regression model. The R² of the relationship between AGB and HV/HH was 0.05 with an RMSE of 68.47 tons ha⁻¹. Similarly, the R² of the regression between HH/HV accounted for 0.04 and RMSE was 68.91 tons ha⁻¹. These results depicted that there is no relationship between the ratio of the HV and HH backscatter and AGB. The result of the regression analysis of AGB with the ratio of HV and HH backscatter and the corresponding summary statistics are presented in Appendix 28 and Appendix 29 respectively.

4.5.4. The Relationship between AGB and HV, HH Backscatter using Multiple Linear Regression

The multi-linear regression analysis was performed to predict AGB using HV and HH backscatter coefficients. The R² and RMSE of the multi-linear regression analysis accounted for 0.89, and 23.63 tons ha⁻¹ respectively. Therefore, the accuracy to predict AGB using both HV and HH backscatter was the same as to predict AGB using HV backscatter only (R²=0.89 and RMSE=23.72 tons ha⁻¹). The results of the multi-linear regression analysis between AGB and HV & HH backscatter are depicted in Table 11.

Table 11: Summary statistics of multi-linear regression between AGB and HV, HH backscatter.

<i>Regression Statistics</i>					
Multiple R	0.941943744				
R Square	0.887258017				
Adjusted R Square	0.883942076				
Standard Error	24.14493388				
Observations	71				
<i>ANOVA</i>					
	<i>df</i>	<i>SS</i>	<i>MS</i>	<i>F</i>	<i>Significance F</i>
Regression	2	311978.8962	155989.4481	267.57355	5.90083E-33
Residual	68	39642.49258	582.9778321		
Total	70	351621.3887			
	<i>Coefficients</i>	<i>Std Error</i>	<i>t Stat</i>	<i>P-value</i>	
Intercept	782.2762684	28.5704158	27.38063995	1.90326E-38	
HV	31.5941808	1.467315468	21.53196192	4.44234E-32	
HH	0.822838276	1.164590979	0.706547012	0.482262058	

4.6. Model Development, Validation and Accuracy Assessment

Simple linear regression analysis was applied to model and validate the relationship between HV backscatter and field-measured AGB. This is because a simple linear regression analysis depicted the highest accuracy to estimate AGB using HV backscatter coefficients. The multi-linear regression using HV and HH backscatter was also performed to test if it improves the estimation of AGB. However, the result showed the same accuracy at R² of 0.89 as the simple linear regression with HV only. Therefore, simple linear regression was used for model development and validation. The number of plots used for model development was 42 which is 60% of the dataset.

4.6.1. Model Development

A linear regression model to estimate AGB using HV backscatter depicted a very high accuracy with R^2 of 0.89. This implied that HV backscatter can explain 89% of the variation in AGB. The RMSE of the model accounted for 23.16 tons ha^{-1} . The RMSE was calculated based on the validation data. The graphical presentation of the model is shown in Figure 28, and the summary statistics of the regression result is shown in Table 12.

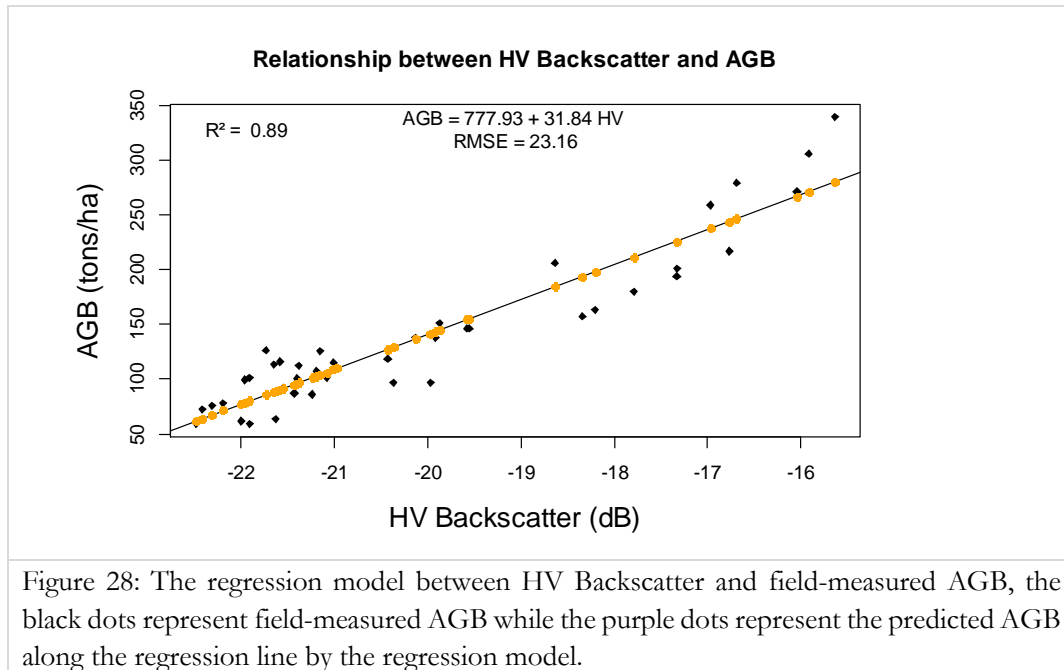


Table 12: Summary statistics of the regression model between AGB and HV backscatter.

Regression Statistics					
Multiple R	0.941616574				
R Square	0.886641773				
Adjusted R Square	0.883807818				
Standard Error	23.7296241				
Observations	42				
ANOVA					
	<i>df</i>	<i>SS</i>	<i>MS</i>	<i>F</i>	<i>Significance F</i>
Regression	1	176171.9874	176171.9874	312.8636706	1.62956E-20
Residual	40	22523.8024	563.0950599		
Total	41	198695.7898			
	<i>Coefficients</i>	<i>Std Error</i>	<i>t Stat</i>	<i>P-value</i>	
Intercept	777.9287067	36.26222587	21.45286694	1.49033E-23	
HV	31.84232664	1.800226809	17.6879527	1.62956E-20	

4.6.2. Model Validation and Accuracy Assessment

The equation derived from the model was used to estimate AGB of the study area. The average estimated AGB from the 29 validation plots was used to validate the model. In other words, estimated AGB from the 29 plots (40% of the dataset) was used to measure the predictive accuracy of AGB by the regression model using HV backscatter. The validation dataset was independent of the data used for model development. The dataset used for model development and validation is shown in Appendix 15.

The regression results of the model validation between the observed (field-measured) AGB and estimated AGB depicted a strong coefficient of determination at R^2 of 0.89. Thus, we concluded that estimated AGB using HV backscatter can explain 89% of the observed AGB. The RMSE of the model validation was calculated at 22.69 tons ha^{-1} which is approximately similar to the model RMSE. The scatterplot of the relationship between the observed and estimated AGB is presented in Figure 29, and the results of the regression statistics of the model validation are shown in Table 13.

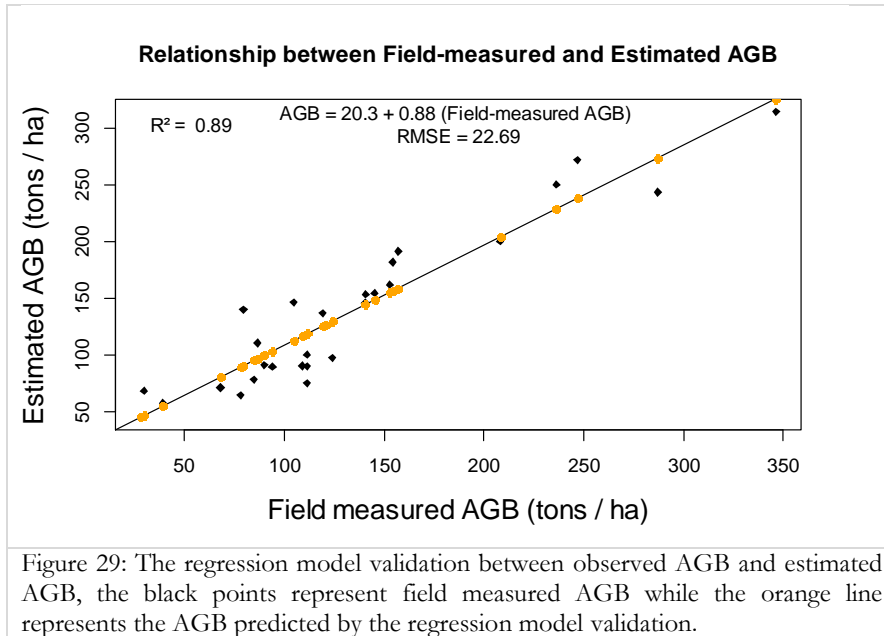


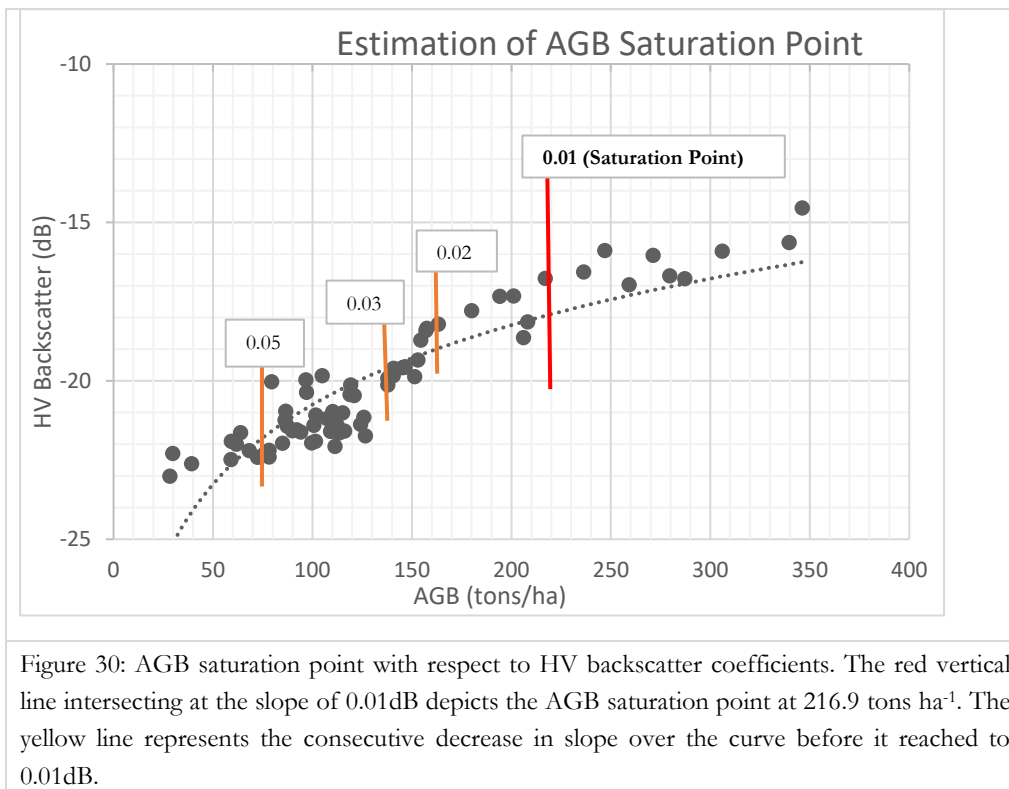
Table 13: Summary statistics of the model validation.

Regression Statistics					
Multiple R	0.942364				
R Square	0.88805				
Adjusted R Square	0.883904				
Standard Error	23.51173				
Observations	29				
ANOVA					
	<i>df</i>	<i>SS</i>	<i>MS</i>	<i>F</i>	<i>Significance F</i>
Regression	1	118398.5092	118398.5092	214.179154	2.33332E-14
Residual	27	14925.63443	552.801275		
Total	28	133324.1436			
	<i>Coefficients</i>	<i>Std Error</i>	<i>t Stat</i>	<i>P-value</i>	
Intercept	20.29957414	9.046459778	2.243924655	0.033237973	
Observed AGB	0.883541913	0.060372416	14.6348609	2.33332E-14	

4.7. Estimation of AGB Saturation Point in relation to HV Backscatter

Figure 30 represents a logarithmic regression between AGB and HV backscatter coefficients. The logarithmic curve has been denoted in the graph by a black dotted line. The slope of the logarithmic regression curve was calculated from the changes in HV backscatter over the changes in AGB following equation 8. The point at which the slope converged to 0.01dB was found at 216 tons ha^{-1} . Thus, we

concluded that the PALSAR-2 HV backscatter saturates at AGB of 216 tons ha⁻¹ as it can be seen at the intersection of the vertical red line in Figure 30.



4.8. AGB and Carbon Stock Map of the Study Area

AGB of the study area was mapped using the equation, $AGB = 777.93 + 31.84 HV$ derived from simple linear regression model developed from the relationship between HV backscatter and AGB as illustrated in section 4.6.1 (Figure 28 and Table 12). Out of 105 ha of the study area, 75 ha was mangrove forest, and 20 ha was water bodies. Therefore, a separate group was created representing water bodies.

The map of estimated AGB of the study area is shown in Figure 31. It can be observed from the AGB map that most of the AGB ranged between 100 tons ha⁻¹ and 200 tons ha⁻¹ followed by 200-300 tons ha⁻¹. The amount of AGB higher than 300 tons ha⁻¹ was mostly found in some areas along the river and scattered in some places over the study area. The average AGB of study area accounted for 181 tons ha⁻¹. The total AGB was estimated at 13,719 tons in the study area.

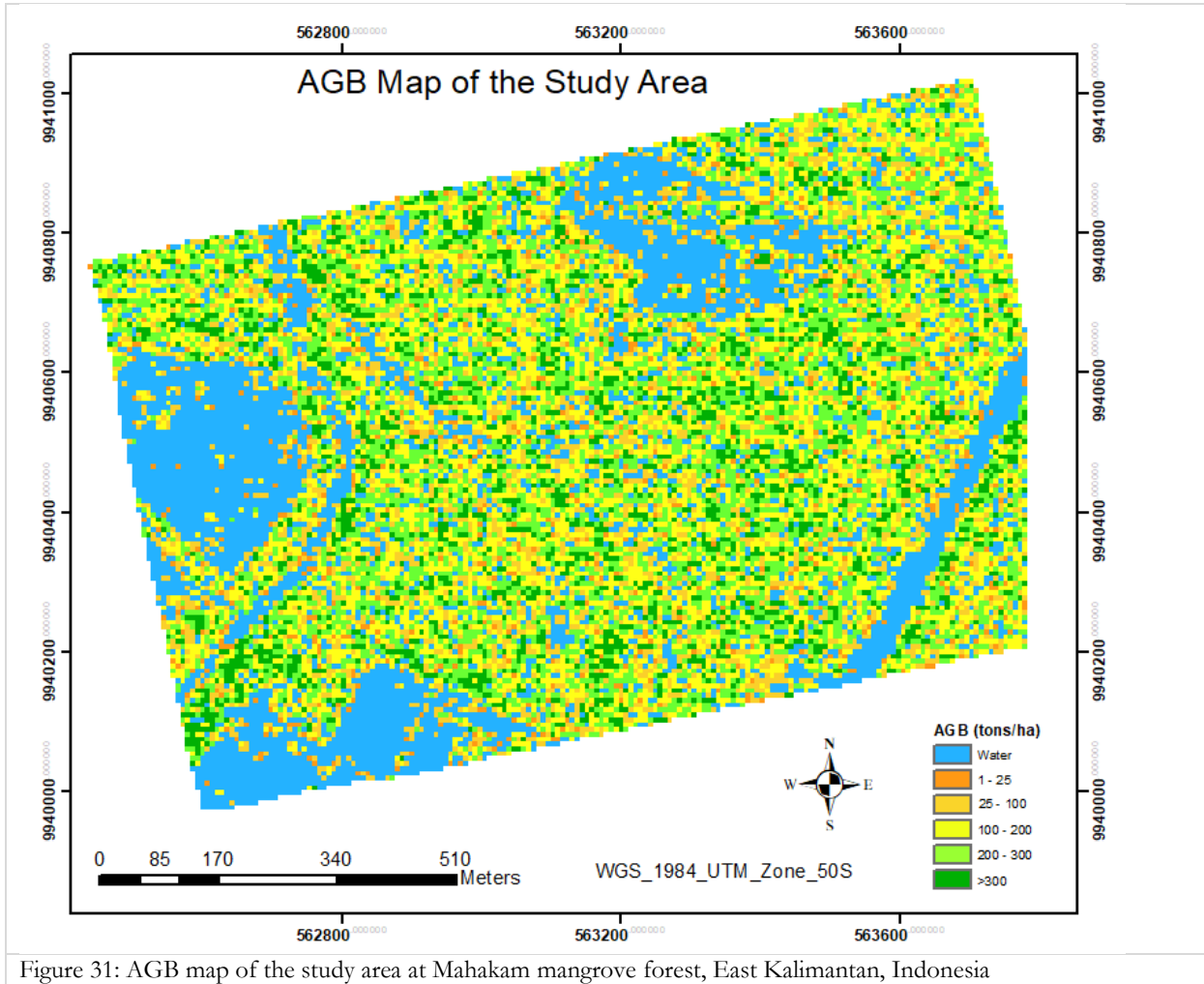


Figure 31: AGB map of the study area at Mahakam mangrove forest, East Kalimantan, Indonesia

It can also be seen from the frequency distribution of the estimated AGB in Figure 32 that AGB ranging from 100-200 tons ha⁻¹ had the highest frequency followed by AGB at 200-300 tons ha⁻¹. The total number of pixels for the range from 100-200 tons ha⁻¹ accounted for 5082, and the total AGB for this range summed to 3773.57 tons. It was followed by 4300 pixels for the AGB ranging from 200-300 tons ha⁻¹ with total AGB at 5193.97 tons. The total AGB with the pixel numbers for the different range of AGB are shown in Table 14. The negative values represented water with a total of 5750 pixels covering an area of 20 ha.

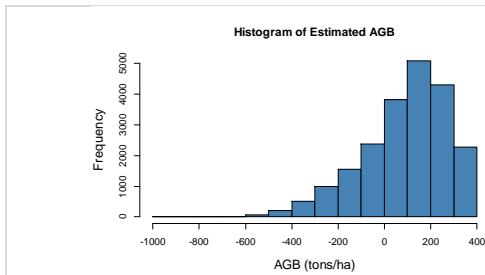


Figure 32: The frequency distribution of the estimated AGB using its histogram. The values more than zero (75 ha) represents ABG values, and the rest is water (20 ha).

Table 14: The total AGB for different AGB ranges with corresponding pixel numbers.

AGB Range	Pixel Number	Total AGB
1-25	767	48.80
25-100	3040	968.27
100-200	5082	3773.57
200-300	4300	5193.97
>300	2271	3734.09
Total	15460	13,719

The carbon stock map of the study area followed the same pattern as the AGB map. This is because the carbon stock map of the study area was produced by converting the AGB estimates using the conversion factor of 0.5 as 50% of forest biomass represents the carbon stock (IPCC, 2007). The average estimated carbon stock stood at 91 tons ha⁻¹ in the study area. The total estimated carbon stock was estimated at 6860 tons. The carbon stock map of the study area is depicted in Figure 33.

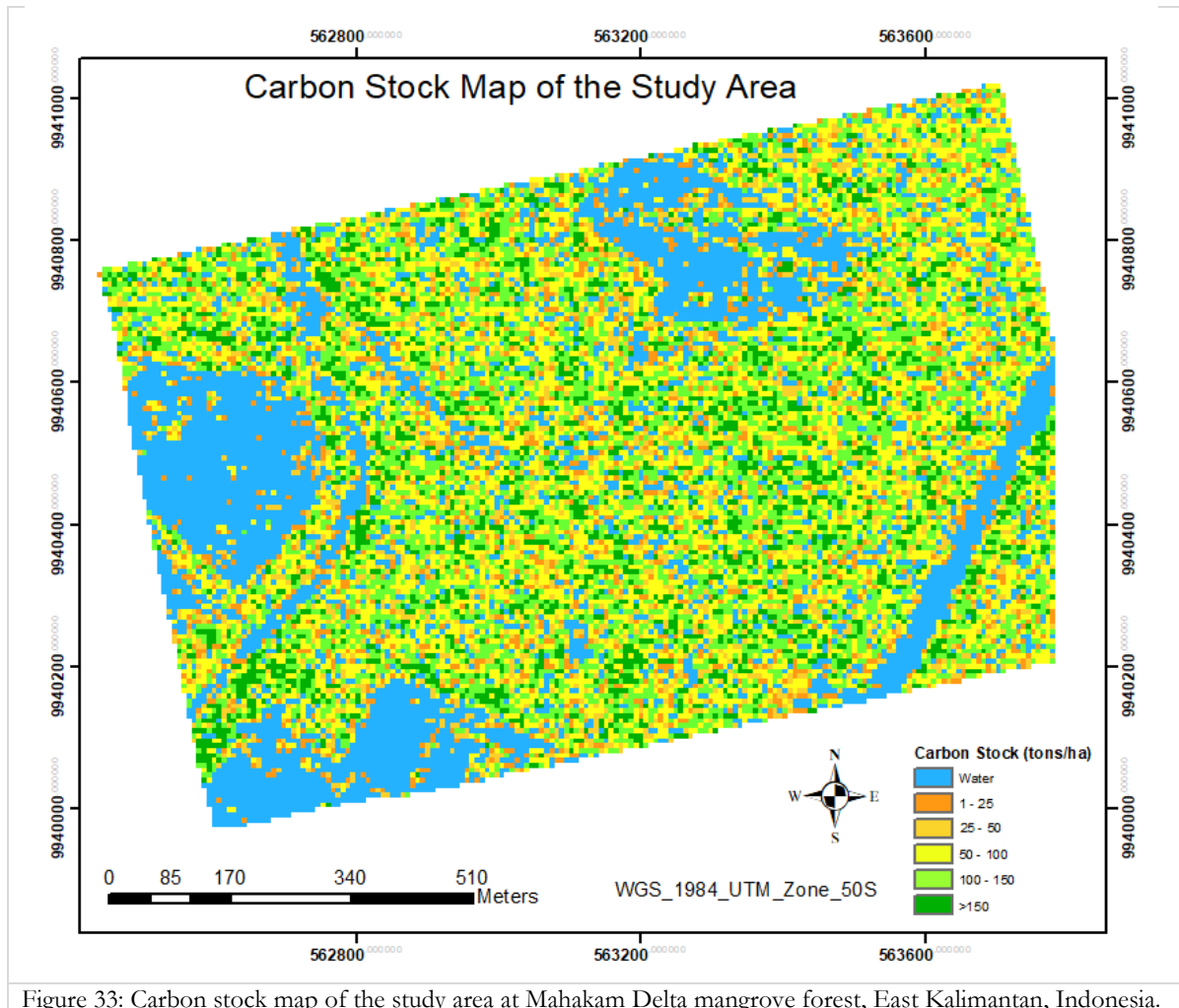


Figure 33: Carbon stock map of the study area at Mahakam Delta mangrove forest, East Kalimantan, Indonesia.

5. DISCUSSION

Mangroves are one of the highest carbon-rich forests in the tropical region, thus play a crucial role in global climate regulation. However, deforestation and degradation of the mangroves contribute to higher carbon emissions accounting for 10% of the CO₂ emissions each year out of 20% emissions in the tropics. To reduce the emissions from deforestation and forest degradation in the tropics, UNFCCC launched UN-REDD+ program in 2008. UN-REDD+ proposed an accurate MRV system of AGB estimation. The MRV system requires a low cost and robust way to measure and monitor the AGB/carbon stock in the tropics. To this end, UN-REDD+ recommends the use of RS techniques. Among different RS techniques, the L-band SAR estimate AGB with higher accuracy in the inland tropical forests. However, the accuracy of AGB estimation is relatively much lower in the mangrove forest. In this context, we aimed to estimate the AGB/carbon stock using ALOS-2 PALSAR-2 in the mangrove forest at Mahakam Delta in East Kalimantan, Indonesia. The accuracy of the AGB/carbon stock estimation is measured in terms of R², RMSE, and p-value.

In our study, a linear regression model is applied to estimate AGB using ALOS-2 PALSAR-2 data. From 71 sample plots, the forest parameters viz. DBH, tree height and wood density are used to calculate field-measured AGB by the allometric equation of Chave et al. (2005). The average HV and HH backscatter coefficients of PALSAR-2 are extracted from the plots using 9 pixels window to cover the approximate plot area. Out of 71 plots, 42 plots are used for model development and the remaining 29 plots for model validation. The regression analysis shows that HV backscatter can predict AGB at higher accuracy whereas the relationship between HH and AGB is very weak. Therefore, cross-polarized backscatter coefficients (HV) are used to estimate and map AGB/carbon stock using a linear regression model in the study area. The data and methods, and the most important findings of AGB estimation and their explanations are described in the following subsections.

5.1. Data and Method of AGB Estimation

The use of the allometric model is a crucial step when it comes to estimating AGB. A general allometric equation for the mixed mangrove forest proposed by Chave et al. (2005) is used in our study to calculate field-measured AGB. This is because AGB is estimated per ha basis in the mangrove forest. One ha of mangrove forest houses several tree species in our study area. Therefore, mixed-species common tree biomass allometry is most appropriate in our case.

We follow the guidelines by Chave et al. (2005) to maintain the quality of the data for calculating field-based AGB in our study. According to Chave et al. (2005), data for calculating AGB in a study should be within the range used in their allometric model. For example, the tree diameter used by Chave et al. (2005) ranges from 5-156 cm. The tree diameter in our study ranges from 11.90 cm to 22.93 cm with a mean DBH of 16.81 cm which is within the range of the allometry model by Chave et al. (2005). The wood density data used by Chave et al. (2005) in their allometric model is available through the World Agroforestry Center database (World Agroforestry Indonesia, 2018; World Agroforestry, 2019). In our study, the wood density data is used from this database. Chave et al. (2005) also stress to measure the diameter in 'cm', and tree height in 'm' which we have followed in our study.

Chave et al. (2005) also mention the necessity to measure the tree parameters correctly. For instance, they recommended to measure the tree diameter above the stem base/buttrass of the tree species. The tree diameter of *Rhizophora spp.* is measured above the buttrass/stem base at 1.3 m height. Moreover, the total

tree height is suggested to measure by Chave et al. (2005). Therefore, tree height is measured from the buttress/stem base to the top of the tree for the *Rhizophora spp.* in our study.

We assumed a linear relationship between the field-measured AGB and HV backscatter coefficients. The reason for assuming a linear relationship is that HV backscatter of L-band SAR increases as the forest biomass increases. Another reason is the homogeneity of the planted young mangrove forest in the study area. Linear regression is sensitive to outliers, and therefore, relative homogeneity of the mangrove forest in our study area leads us to assume that a linear model is a right choice to estimate AGB in our study. Our assumption is proved as linear regression analysis shows a linear relationship between field-measured AGB and HV backscatter coefficients at a higher accuracy. Our data also complies with the requirements of a linear relationship. Therefore, a linear model to estimate AGB is most appropriate in our study.

However, HV tends to saturate at AGB of 216 tons ha⁻¹. This raises a limitation of estimating AGB using HV backscatter coefficients with the higher range > 216 tons ha⁻¹ forest biomass. This means that the relationship is non-linear between forest biomass and HV backscatter in the dense forest where the mean of AGB is more than 216 tons ha⁻¹.

Although the HV signals show saturation, the linear model depicts a higher accuracy in our study. The field-measured AGB in our study ranges from 28.3 tons ha⁻¹ to 346.2 tons ha⁻¹. Thus, we can infer that the linear model estimates AGB beyond the saturation level in our study. This can be supported by the accuracy of the model and model estimation; both have higher accuracy at R² of 0.89. Further research can be done on exploring this issue.

5.2. The relationship between AGB and Backscatter Coefficients

We hypothesize a significant relationship between the field-measured AGB and the backscatter coefficients of the PALSAR-2 in our study. To prove our hypothesis, we perform a linear regression analysis between HV backscatter coefficients and field-measured AGB to estimate the AGB in the study area. The relationship between AGB and HH backscatter coefficients were also explored using simple linear regression. Furthermore, a multi-linear regression is performed using both HV and HH backscatter coefficients to test if it can improve the accuracy of the AGB estimation. The results indicate that HV backscatter coefficients yield higher accuracy for predicting AGB in the mangrove forest (R²=0.89, RMSE=23.16). This implies that there is a significant relationship between field-measured AGB and HV backscatter coefficients at higher accuracy.

Our findings are consistent with the fact that volume scattering increases as the canopy size increases in the forests (Figure 34). Therefore, L-band HV polarized backscatter is used to model AGB in the forests (Carver, 1988; Hussin, 1990; Henderson & Lewis, 1998) .

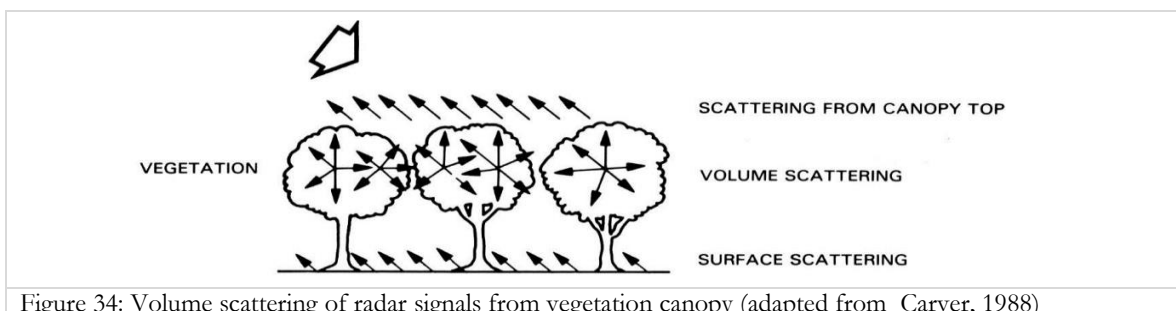


Figure 34: Volume scattering of radar signals from vegetation canopy (adapted from Carver, 1988)

The relationship between HV polarized backscatter of L-band SAR and AGB is significantly positive in the temperate (Rosenqvist et al., 2003), inland tropical forests (Nga, 2010a; Odipo et al., 2016; Sumareke, 2016;

Masolele, 2018) and mangrove forests (Hamdan, et al., 2014; Pham & Yoshino, 2017; Pham, et al., 2017; Pham, et al., 2018). However, the accuracy of AGB estimation using L-band SAR is comparatively much lower in the mangrove forests in earlier studies (Hamdan, et al., 2014; Pham & Yoshino, 2017; Pham, et al., 2017; Pham, et al., 2018) than in the tropical inland forests (Nga, 2010; Odipo et al., 2016; Sumareke, 2016; Masolele, 2018). On the contrary, our study depicts a higher accuracy ($R^2 = 0.89$) to estimate AGB in the tropical mangrove forest using L-band PALSAR-2 as it is observed in the terrestrial tropical forests in earlier studies (Nga, 2010a; Odipo et al., 2016; Sumareke, 2016; Masolele, 2018).

Our study shows HV backscatter coefficients are the best predictor for estimating AGB in the mangrove forest. This is consistent with a previous study in Malaysia (Hamdan et al., 2014) where HV polarized backscatter coefficients are used for estimating AGB in the Matang mangrove forest using a simple linear regression model. However, Hamdan et al. (2014) reports much lower predictive accuracy of HV backscatter to estimate AGB where R^2 is 0.41 with an RMSE of 33.90 tons ha^{-1} . On the other hand, the accuracy to estimate AGB is much higher at R^2 of 0.89 with a RMSE of 23.16 tons ha^{-1} .

The RMSE of AGB estimation in our study is comparatively lower than RMSE found by Hamdan et al. (2014). The reason for relatively lower RMSE is due to the improved accuracy of AGB estimation in our study. It can also be because AGB is estimated in a small and quite homogenous area of the mangrove forest in our study, whereas AGB is estimated for the entire Matang mangrove forest in Malaysia by Hamdan et al. (2014). However, the range of the field measured AGB in our study ranging from 28 - 346 tons ha^{-1} is comparable to the field-measured AGB (9.53 - 340.82 tons ha^{-1}) in the study by Hamdan et al. (2014). Also, some species in our study area are similar to those reported by Hamdan et al. (2014) where 85% of the species were *Rhizophora murconata* and *Rhizophora apiculata*. In our study, *Rhizophora spp.* consists of 38% of the tree species.

Like our study, Hussin et al. (1990) obtain a similar accuracy to model AGB in a swampy forest in Northern Florida. However, the authors develop the models using the tree height and DBH estimated from the radar backscatter coefficients instead of the direct backscatter coefficients. Hussin et al. (1990) obtain R^2 at 0.82 for estimating AGB using the tree height derived from the radar backscatter.

Pham and Yoshino (2017) have reported that multi-polarization backscatter coefficients are better predictor compared to single polarization of HV for estimating AGB in the mangrove forest in Vietnam. The authors use a multi-linear regression model to estimate AGB in the mangrove forest. However, a multi-linear regression model using the multi-polarization of HV and HH backscatter yields almost the same result ($R^2 = 0.89$ and RMSE = 23.63) as the simple linear regression using HV polarization in our study. Given this outcome of our study, we can conclude that the predictive accuracy of HV and HH multi-polarizations to estimate AGB in the mangrove forest is comparable to that of single HV polarization, but not a better predictor.

The results of the study by Pham and Yoshino (2017) depict the accuracy of AGB estimation at $R^2 = 0.51$ and RMSE = 35.5 Mg ha^{-1} for *Sonneratia caseolaris* species, $R^2 = 0.64$, RMSE = 41.3 Mg ha^{-1} for *Kandelia obovata* species and R^2 of 0.34 for the mixed mangrove forest. These findings show much weaker R^2 and higher RMSE, i.e., much lower accuracy where we have higher accuracy ($R^2 = 0.89$ and RMSE = 23.16) for AGB estimation of the mixed mangrove forest comprising mainly *Avicennia Alba* and *Rhizophora spp.*

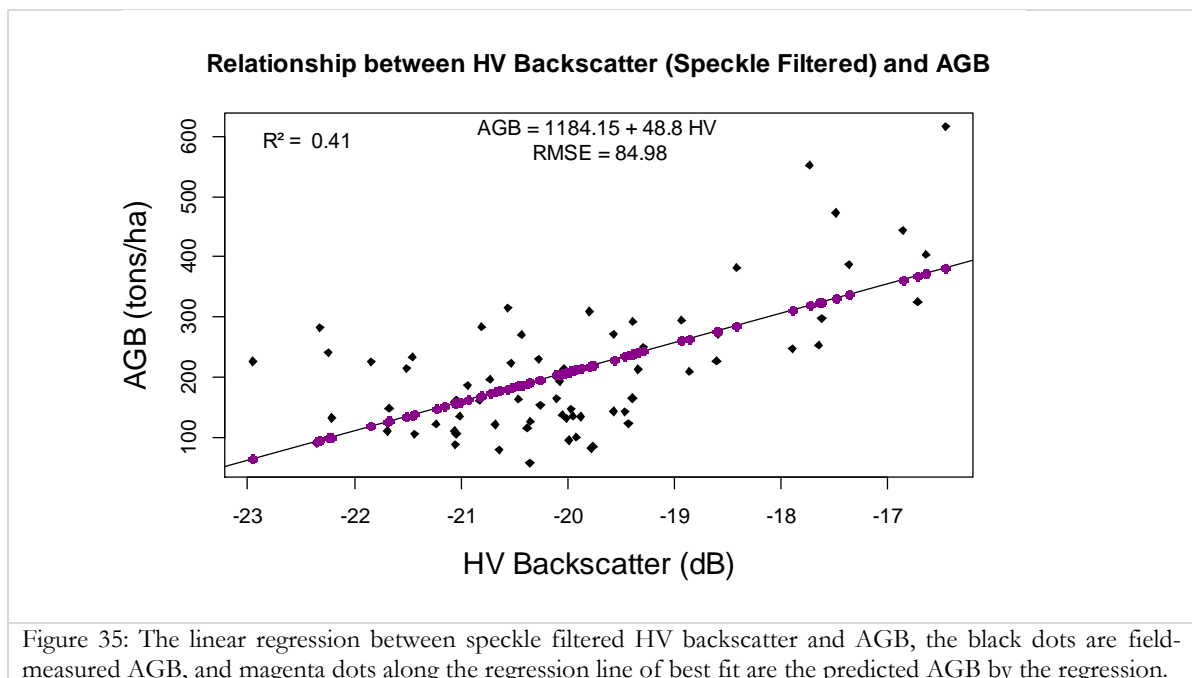
Pham et al. (2017) used multi-polarization HV and HH backscatter from ALOS-2 PALSAR-2 for estimating AGB of a single mangrove species, *Sonneratia caseolaris* using a multi-layer perceptron neural networks (MLPNN) model. The result shows the performance of the model at R^2 of 0.776. However, the MLPNN model does not perform well for mixed mangrove stands (Pham et al., 2018) restricting its application to the single species mangrove forest only. There are several tree species in one hectare of the mangrove forest in the tropics (De Oliveira & Mori, 1999). Therefore, species-wise regression models are not useful in the

tropical forests as in the temperate zones (Ter-Mikaelian and Korzukhin, 1997; Shepashenko et al., 1998). The mangrove forest in our study represents mixed mangrove species at Mahakam Delta. Thus, the higher accuracy of our model has significant implications for estimating AGB in the mixed mangrove forests.

L-band SAR data have also been integrated with optical data to estimate AGB in the mangrove forest in an earlier study (Pham et al., 2018). Pham et al. (2018) integrated PALSAR-2 data with Sentinel-2A data to estimate AGB in the mangrove forest of Vietnam comprising mainly *Kandelia obovata* and *Sonneratia caseolaris* species. The authors used nine variables (HH, HV, HV/HH, HH-HV, NIR, and 4 PC1) resulted from the data integration to predict AGB using machine learning algorithm, support vector regression (SVR). However, the accuracy of the model is moderate at R^2 of 0.596. Pham et al. (2018) also used four other machine learning techniques (radial basis function neural networks, multi-layer perceptron neural networks, Gaussian process, and random forest). Nevertheless, the performance of these models is lower than that of SVR. On the contrary, the accuracy of the linear model in our study to estimate AGB using HV backscatter is much higher than the four models of Pham et al. (2018).

It is evident from the review of the findings that the accuracy of the model in our study to estimate AGB outperforms the accuracy of AGB estimation in the mangrove forests in previous studies. Some factors can explain the higher performance of the AGB estimation in the mangrove forest in our study.

First and foremost, the pre-processing of PALSAR-2 data has a significant influence on achieving higher accuracy of AGB estimation in our research. The PALSAR-2 image is not filtered to remove speckle from the data. This is because filtering greatly affects the accuracy of the AGB estimation in our study. The effect of speckle filtering on the accuracy of AGB estimation is depicted in Figure 35.



The reason why speckle filtering affects the accuracy of AGB estimation can be explained by the characteristics of the study site in our research. The study area is intersected by the Mahakam River and several water channels Appendix 18. Smooth water bodies cause specular reflectance with no return of Radar signals. Thus, the water pixels appear dark on the image. In many places, the muddy ground floor of mangrove forest has water surface even during peak hours of low tide Appendix 14. The specular reflectance from the flooded soil is depicted in Figure 3 in section 2.3.3.

As the specular reflectance causes no return of Radar energy, the water pixels appear dark on the image and have lower pixel values. On the other hand, backscattering from the forest biomass results in a brighter pixel with higher values. During the speckle filtering, the water pixels and forest biomass backscatter pixels are averaged as it takes the average of the pixels from the filtering window. It implies that filtered image has the average values of water pixels and forest biomass backscatter pixels. This degrades the true backscatter coefficients observed in the biomass of mangrove forest in our study. This eventually results in the lower performance of AGB estimation as shown in Figure 35. Therefore, to preserve the true forest biomass backscatter coefficients, only geometrically corrected PALSAR-2 image is used in our study. Eventually, this results in higher accuracy ($R^2 = 0.89$) in estimating AGB in the mangrove forest in our study area.

However, the previous studies used speckle filtering on their L-band SAR to remove the speckle from the data (Pham & Yoshino, 2017; Pham et al., 2017, 2018). The authors used Forst filter with a 5×5 moving window. The use of filtering might also have affected the accuracy of AGB estimation in their study.

Moreover, the enhanced backscattering in the mangrove areas has an important contribution to the AGB estimation in our study. The enhanced backscattering is mainly observed in the forest areas with the muddy ground floor having high water content and higher vegetation in our study (Appendix 11 and Appendix 14), which is related to the time of image acquisition. The image scene acquisition time of PALSAR-2 in our study is 16:26:06 (UTC) on 30 July 2018. This is equivalent to 1:26 (am) local East Kalimantan time which represents the peak hours of the first low tide started at 12. 28 am at Mahakam Delta, East Kalimantan on 30 July 2018 (Tides4Fishing, 2019). Our study area is inundated 2.5 m during the high tide. The inundation of the forest affects the backscattering of the L-band SAR. Therefore, PALSAR-2 image acquisition during the low tide condition contributes to the enhanced backscattering as observed by other studies. According to Ormsby et al. (1985), Imhoff et al. (1986), Imhoff et al. (1987), Hussin (1990), Wang & Imhoff (1993), and Henderson & Lewis (1998), L-band cross-polarized backscatter of the flooded forest is enhanced because of the wet stems and the wet condition of forest ground (Figure 36).

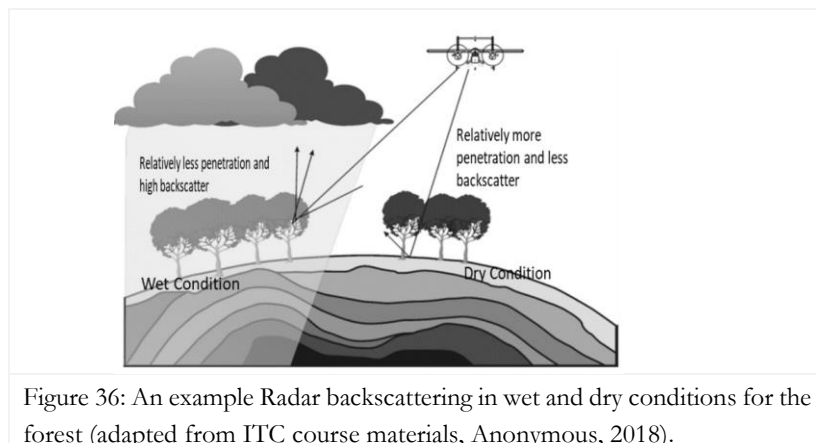
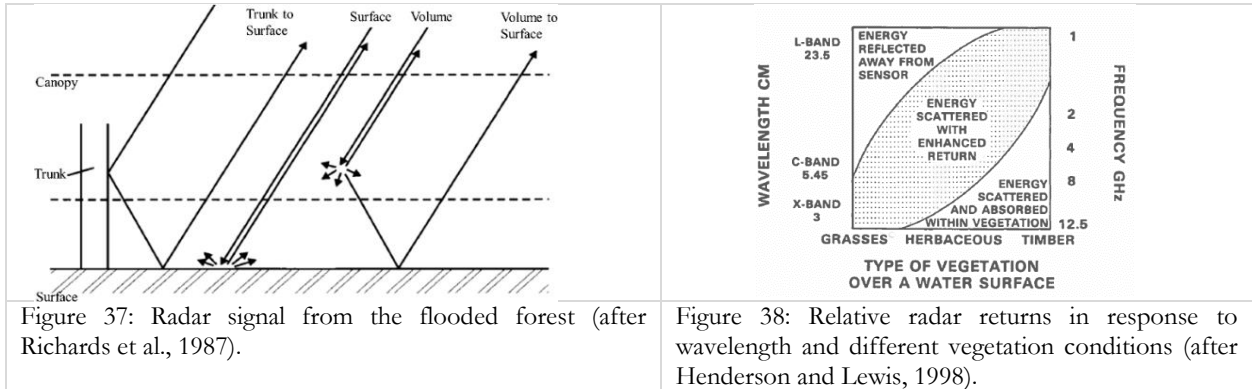
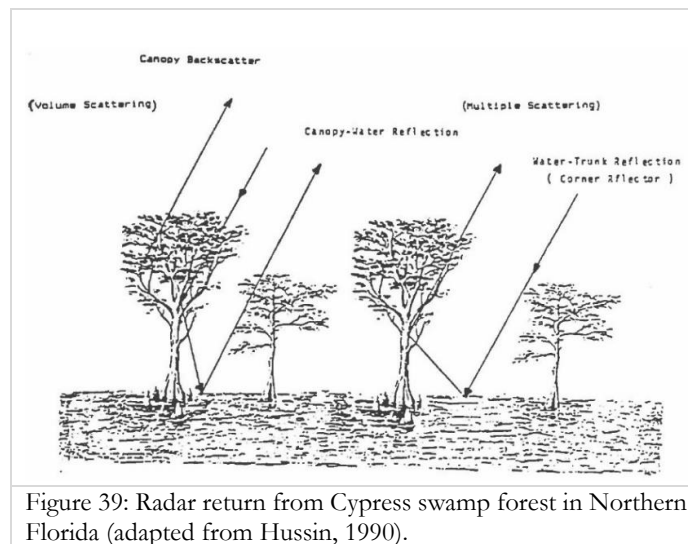


Figure 36: An example Radar backscattering in wet and dry conditions for the forest (adapted from ITC course materials, Anonymous, 2018).

As L-band has a longer wavelength and can penetrate down to the ground surface in the forests, backscatter from L-band radar is enhanced from the flooded forest vegetation because of the high dielectric constant of the ground floor and wet stems. The scattering characteristics from the flooded forest are illustrated in Figure 37 and 38.



Hussin (1990) has observed a similar phenomenon of the enhanced L-band backscatter in a Cypress swamp forest in Northern Florida where the author models the biomass with higher accuracy. The radar returns from the Cypress swamp forest in Northern Florida is shown in Figure 39 which follows the same pattern as in Figure 37.



The growth of the trees can also contribute to the AGB estimation in our study. The age of the mangrove trees in our study area is approximately 16 years which is approximately similar to the studies in Vietnam (Pham & Yoshino, 2017; Pham et al., 2017, 2018) and Malaysia (Hamdan et al., 2014). However, the average height of the trees in our study area is comparatively higher ranging from 10.5 m to 18.3 m while the height of the trees ranged from 2.84 m to 7.61 m in the studies in Vietnam (Pham & Yoshino, 2017; Pham et al., 2017, 2018). The tree diameter in our study differs from the study by Hamdan et al. (2014) where the tree diameter in the sample plots ranges from 5.0 to 48.8 cm. The majority of the plots have higher AGB in our study (>115 tons ha^{-1}) than that of Hamdan et al. (2014) with (<100 tons ha^{-1}). The range of AGB is higher in our study compared to the studies in Vietnam (Pham & Yoshino, 2017; Pham et al., 2017, 2018) where the AGB of the mangrove forest ranges from 36.22 to 230.14 $Mg ha^{-1}$ with a mean of 87.67 $Mg ha^{-1}$. As there is an increase in volume scattering with the growth of the trees (Le Toan et al., 1992), it can influence the AGB estimation using HV backscatter coefficients in our study. This is because the HV polarization of L-band is related to the volume scattering from the forests.

It should be mentioned here that our mangrove forest at Mahakam is about 16 years old with natural style plantations. On the other hand, the mangrove in Malaysia is a planted and sustainably managed mangrove forest (Hamdan et al., 2014). Also, it is a planted mangrove with community-based forest management in Vietnam (Pham & Yoshino, 2017; Pham et al., 2017, 2018). Therefore, the differences mentioned in the

range of biomass and forest parameters are because of the differences in the characteristics of the mangrove forests.

Moreover, the diameter of the trees could play a role in AGB estimation in our study. It has been reported that trees <10 cm in diameter does not contribute significantly to biomass estimation (Brown, 2002). Therefore, we included trees ≥ 10 cm diameter in our study. However, the studies conducted in Malaysia and Vietnam include trees from 5 cm in diameter for AGB estimation (Hamdan et al., 2014; Pham & Yoshino, 2017; Pham et al., 2017, 2018).

The distribution of sample plots in the study area might be another reason. We have a small study area covering nearly 105 ha. The number of sample plots in this small study area was 71 which shows a homogenous distribution of the plots over the study area. Thus, it covers all the variations in the study area. In other studies, the area is larger, but the sample plots are less and scattered over the study areas. This might not cover all the variations in their study area. In the study in Malaysia (Hamdan et al., 2014), 320 sample plots are scattered over 41,000 ha of mangrove forest. While in the study in Vietnam, the number of sample plots is 25 covering the mangrove forest of about 125 km along the Hai Phong coast (Pham & Yoshino, 2017; Pham et al., 2017, 2018).

5.3. The relationship between BA, DBH, Tree Height and Backscatter Coefficients

The HV and HH polarizations are analyzed to assess their relationship with different biophysical parameters of the mangrove forest viz. BA, DBH and tree height. The results show that the BA has a strong positive relationship with L-band HV polarization whereas the relationship is weak with HH polarization. However, no significant relationship is observed between BA and L-band HV or HH polarization in a study conducted on a degraded black mangrove in the Mexican Pacific (Kovacs et al., 2013). Again, Pereira et al., (2016) reported an opposite result on a mangrove forest in São Paulo, Brazil where BA has a weak negative correlation with L-band HV backscatter and a strong positive correlation with HH backscatter.

The strong relationship of L-band HV backscatter with BA in our study is consistent with the findings of the studies on the dry inland forest. For instance, Hussin et al. (1991) observed a strong positive correlation between L-band HV polarized backscatter and BA at R^2 of 0.83 in the Slash Pine forest in Northern Florida. Moreover, the relationship between HV polarization of L-band SAR and BA in the Landes forest of Southern France is observed at R^2 of 0.91 (Le Toan et al., 1992). Furthermore, L-band HV polarizations of SAR is depicted to predict BA in Ayer Hitam tropical rainforest reserve in Malaysia at R^2 of 0.67 (Sumareke, 2016).

In our study, the relationship between DBH and L-band HV polarization is positive and moderately strong while it shows a weak positive relationship with L-band HH. Pham et al. (2017) also reported a positive relationship DBH with L-band HV and HH, but the accuracy is comparatively poor. On the contrary, Pereira et al., (2016) demonstrate a moderate negative correlation of DBH with L-band HH and a weak negative correlation with L-band HV. However, no significant relationship is observed between L-band HV or L-band HH with DBH in a study (Kovacs et al., 2013)

The relationship of tree height with HV and HH polarizations is weak and positive in our study. However, the relationship is comparatively strong in HV polarization than that of HH polarization. This is consistent with the results observed by Pham et al. (2017). However, Pereira et al., (2016) show a moderate negative relationship of tree height with L-band HH and a weak negative relationship with L-band HV backscatter.

The positive relationship of the L-band HV polarization with the forest parameters in our study relates to the fact that AGB is a function of forest parameters such as height, DBH, BA and wood density (Hussin, 1990). Our study depicts a strong positive relationship of L-band HV with BA than other forest parameters,

e.g., DBH and tree height. This is consistent with the findings that BA is the best predictor of AGB reported by some previous studies (Hussin et al., 1991; Le Toan et al., 1992)

In our research, HV polarization has a stronger correlation with all forest parameters compared to HH polarization. These results are consistent with the findings reported by a study in the mangrove forest in Vietnam (Pham et al., 2017). The comparatively strong relationship of HV backscatter with the forest parameters corresponds to the fact that the volume scattering strengthens the L-band cross polarization because it can pass through the canopy down to the ground surface (Mougin et al., 1999; Proisy, 2000).

5.4. Determination of AGB Saturation

The AGB saturation point about HV backscatter is assessed in our study. The results show that HV backscatter saturates at AGB of 216 tons ha⁻¹ in the mangrove forest in our study area. The AGB saturation level estimated in our study is higher compared to other studies in the mangrove forests using L-band SAR. Lucas et al. (2007) depict that L-band SAR saturates at AGB over 100 Mg ha⁻¹ in mangrove forests. Similarly, the saturation level of AGB has been shown at 100-150 tons ha⁻¹ at Matang mangrove forest in Malaysia using HV backscatter of PALSAR (Hamdan et al., 2014). AGB saturation has also been reported over 100 tons ha⁻¹ using the backscatter of PALSAR-2 in the mangrove of Hai Phong city in Vietnam (Pham et al., 2018).

Our study area is affected by the tidal phenomenon; the forest floor is inundated during high tide and usually muddy with high water content during low tide. The muddy surface with high content has a high dielectric constant. We used ALOS-2 PALSAR-2 image that was captured during peak hours of low tide; thus, the backscatter of PALSAR-2 is greatly enhanced by the high dielectric constant of the muddy ground surface. Therefore, we can conclude that inundation of mangroves does not induce saturation at a low level of AGB as observed by Lucas et al. (2007). The ground picture of the study area during peak hours of low tide is presented in Appendix 14.

The extensive prop root systems and tidal inundation level of mangroves affect saturation level of AGB in the mangroves (Lucas et al., 2007). It also depends on the dielectric constant and distribution of the backscattering and forward-scattering functions of the individual scatterers (Chen et al., 2009). The saturation level at increased AGB level in our study can be caused by increased dielectric constant, among others. The dielectric constant of dry soil is 4, and that of water is about 81. This means that the dielectric constant of the ground increases with the increase of water content (Richards, 2009). Therefore, the muddy surface during low tide leads to high dielectric constant, which greatly enhance the backscatter of the forested area (Ling & Dai, 2012; Wang et al., 1995).

5.5. AGB and Carbon Stock Map

Since the HV backscatter coefficients are the best predictor for estimating AGB in our study, a linear regression model is developed between HV backscatter coefficients and AGB. The model predicts AGB at a higher accuracy with a coefficient of determination, R², of 0.89. This indicates a satisfactory correlation between model estimation and field measured AGB. The model validation also results in identical accuracy at R² of 0.89. This means that the predictive performance of the model stays unaltered when it is applied to the dataset that was not used in the model AGB estimation.

The estimated AGB ranges between 1 - 350 tons ha⁻¹ with an average of 181 tons ha⁻¹ in our study. The results reveal that the mean of the estimated AGB is consistent with the mean of field measured AGB. This implies that the estimated AGB by the model reflects the field-measured AGB. The range of the estimated AGB in our study is comparable to the study on Matang mangrove forest (Hamdan et al., 2014) where the estimated AGB ranges between 2.98 and 378.32 ± 33.90 Mg ha⁻¹. However, the average estimated AGB is

higher in our study compared to the study by Hamdan et al. (2014). On the other hand, our results differ from the study reported by Pham et al. (2018) where the distribution of AGB ranged from 36.22 and 230.14 tons ha⁻¹ with an average of 87.67 tons ha⁻¹.

It is evident from the AGB map in our study that areas close to the river and water bodies have relatively higher AGB values. This is mainly because mangrove trees on both sides of the river are bigger and dense resulting in higher backscattering and thus, higher AGB estimates. Another reason is the double bounce scattering along the river, i.e., scattering from water to tree. The acquired PALSAR-2 was right looking. Therefore, the forest on the right side of the river presents higher pixel values as a result of double bouncing between water and trees. Some areas with higher AGB values were also scattered in the study area. This is because of the high dielectric constant of the muddy surface and double-bounce scattering from the ground surface to the tree canopy. The areas with open canopy and ground floor having water surface have lower AGB in the study areas. These low AGB can be attributed to the specular reflectance from the ground with water surface particularly from the areas with an open canopy.

Backscatter outliers with highly extreme values are masked out from the study area. The highest field measured AGB of 346 tons ha⁻¹ (round off to 350 tons ha⁻¹) is used a cut-off value to mask out these outliers. It is done to eliminate the effect of outliers from over-estimation of AGB/carbon stock. These outliers are present in the study area because of the backscattering from the corner reflectors, and double-bounce scattering.

A separate group was created for negative AGB values. The reason behind having negative AGB values is that the study area is intersected by the Mahakam River and several water channels. Smooth water bodies cause specular reflectance with no return of radar signals appearing dark on the image. Therefore, a separate water layer is created for the negative values to differentiate between water and forest biomass in the AGB/carbon stock map.

5.6. Limitations and Uncertainties of the Study

5.6.1. Uncertainties associated with the Field Data Measurement

A Leica DISTO D510, laser height measurement instrument, is used for measuring tree height in our study. However, a laser from this instrument cannot reach at the top branches of the trees as tree canopy act as a barrier for the laser to reach the canopy top. Sometimes, the branches of the other trees in front of a tree pose a limitation to measure the tree height correctly. These shortcomings lead to underestimation of tree height using a Leica DISTO D510. From the measurement of tree height using Terrestrial Laser Scanning (TLS) for other studies in our study area, it is observed that the underestimation of tree height using a Leica DISTO D510 is approximately 2 m on average.

In the case of *Rhizophora spp.*, tree height is measured from the prop roots on the ground to the top of the trees as prop roots contribute to the backscattering of PALSAR-2. However, the amount of backscattering from prop roots is unknown.

The errors associated with the measurement of plot coordinates by Garmin GPS introduced difficulties in identification of the plot center. The uncertainties of GPS location measurement are around 5 m. This error level is observed in the location of the plot center by cross-checking through additional coordinates taken at four corners of the plot. This shifting in a plot position has caused difficulties in the identification of the exact plot position, thereby extraction of average backscatter values from the plot. We have addressed this issue with the visual analysis of the plot position using the drone images. Although this has helped to fix the shifting problem of the plot, it is not free from error.

5.6.2. Uncertainties associated with the Wood Density Data

The wood density data is collected from the World Agroforestry and World Agroforestry Indonesia database (World Agroforestry Indonesia, 2018; World Agroforestry, 2019). Most of the wood density data in this database are compiled from different mangrove forests of Indonesia including East Kalimantan. However, some of the data are also acquired from Australia and Latin America. Therefore, it may not be truly representative of the wood density of the tree species in our study area. Also, the growth and age of mangrove forest included in the database vary from the mangrove forest in our study. Therefore, the use of wood density data from this database might have introduced some errors to the field-measured AGB.

5.6.3. Uncertainties associated with AGB Calculation using Field Data and Allometry

The use of allometric equation for AGB calculation might have introduced some error to the field measured AGB. There are many multi-stemmed trees in the study area. Each stem is treated as an individual tree as allometric relationships are very similar to a single tree for each stem of a multi-stemmed tree (Clough et al., 1997). In case of *Rhizophora spp.*, the DBH measurements are taken at 1.3 m height from the stem junction over the prop roots for both single and multi-stemmed trees.

The allometric equation developed by Chave et al. (2005) uses data from 27 sites across the tropics. For developing the allometric equation, trees with diameter ≥ 5 cm are used by Chave et al. (2005). However, trees ≥ 10 cm is measured in our study since trees ≤ 10 cm in diameter has no significant contribution to AGB estimation (Brown, 2002).

Considering all these aspects, it seems clear that there might be some uncertainties in calculating field AGB due to differences in measurements of forest parameters between our study and the study on the allometric model by Chave et al. (2005).

5.6.4. Uncertainties associated with the Conversion of the Plot AGB

The conversion of the plot AGB into the AGB estimates of the study area involves some steps. These steps deal with various techniques that introduce some uncertainties in the estimation. The sources of these errors in AGB estimation in the tropical forests are shown by Chave et al. (2004) as in Figure 40. These include uncertainties with a single tree AGB measurement, error due to using an allometry equation, sampling uncertainty, uncertainties with a single plot and uncertainties in the estimation of AGB over the study area using all the sample plots.

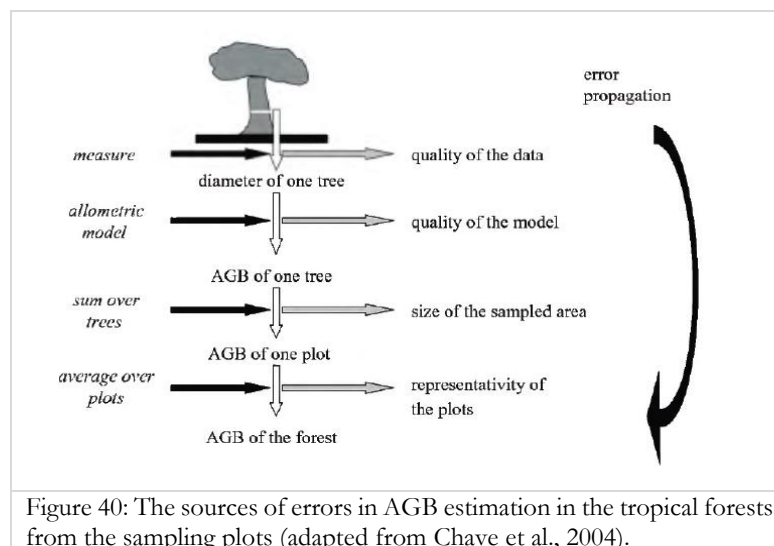
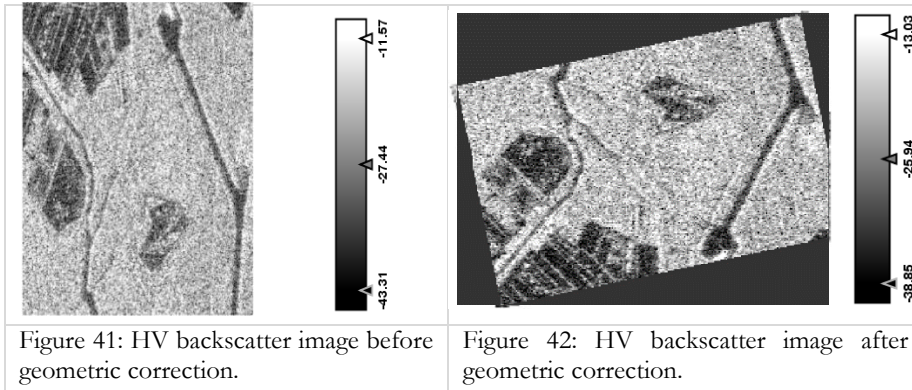


Figure 40: The sources of errors in AGB estimation in the tropical forests from the sampling plots (adapted from Chave et al., 2004).

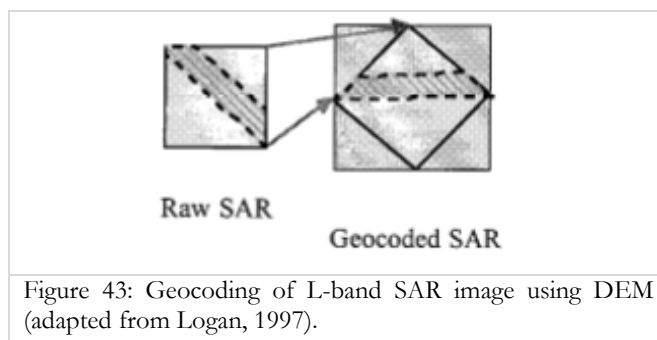
5.6.5. Uncertainties associated with PALSAR-2 data processing

After retrieving the backscatter of HV and HH polarizations, geometric correction is performed on the PALSAR-2 image using SRTM-1 of 30 m resolution. On the other hand, the PALSAR-2 image has 4.29 m pixel spacing. The use of lower resolution SRTM for geometric correction cause lower resolution of PALSAR-2 image (7 m resolution), thus affecting the backscatter values which is visible in the backscatter image before and after geometric correction (Figure 41 and 42).



It can be seen from the legend of Figure 41 and 42 that most of the values range between -11.57 dB and -27.44 dB before geometric correction. On the contrary, most of the backscatter values range from -13.03 dB to -25.94 dB after the geometric correction. This degradation in the backscatter values is attributed to the geometric correction of the PALSAR-2 image using low-resolution SRTM compared to the resolution of PALSAR-2 image. Therefore, it is evident that there are some uncertainties in AGB estimation caused by geometric correction.

The reason behind the lower resolution of PALSAR-2 image is that during the geometric correction, PALSAR-2 is resampled to the spatial representation of the SRTM-1 digital elevation model (DEM). This involves the rotation and scaling of the PALSAR-2 image to transform it correctly into the Universal Transverse Mercator map projection (Logan, 1997). An example of this process is given in Figure 43. The resampling of PALSAR-2 image on the comparatively low-resolution SRTM DEM lowers the backscatter values as illustrated in the previous Figure 41 and 42.



5.7. The Relevance of the Study

5.7.1. Relevance in terms of Generalization

The model in our study can be replicable to estimate AGB with higher accuracy in other mangrove forest areas. However, some aspects need to take into consideration before replicating the model. For instance, our study is conducted on the mangrove forest in the sea-front areas. Therefore, it is highly affected by tides and intersected by the river and several water channels. Therefore, data acquisition and processing should

be done considering the characteristics of the study. For example, PALSAR-2 data is acquired during peak hours of low tide in our study area. Moreover, we avoid speckle filtering of PALSAR-2 data as it mixes the water and forest biomass pixels, thus affects the accuracy of AGB estimation.

Biometric data collection should also be done carefully. The dominant tree species are *Avicennia alba* and *Rhizophora spp.* in our study area. In the case of *Rhizophora spp.*, the measurements should be taken above the buttress and tree height from the ground to the top of the canopy. Importantly, our study area is homogeneous as it represents the planted mangrove forest of about 16 years old. Thus, our model can be replicated for AGB estimation of a mangrove forest having similar characteristics.

There are limitations inherent to the methods used in our study to generalize the findings beyond the study conditions. For instance, the relationship may not be linear between the HV backscatter and AGB in all cases. If the variation is higher in forest biomass distribution, our model findings cannot be generalized. Also, AGB saturation is another disadvantage. AGB saturation varies from forest to forest depending on the forest structure and backscattering mechanism, among others. The use of allometry to calculate field-based AGB poses another limitation for generalization of the findings in a broader context. This is because the allometry equation is applied for a given range of conditions. For example, the diameter of the tree should be 5-126 cm.

5.7.2. Relevance to the MRV system of UN-REDD+

Measuring AGB accurately over the tropics using RS is a requisite for the MRV system of UN-REDD+. Many studies show higher accuracy to estimate AGB using L-band SAR data in the inland forest/rainforest in the tropics and subtropics. However, the research is limited for AGB estimation in the mangrove forest due to the complex nature of the forest. A few studies have been conducted so far on the estimation of AGB using L-band SAR. However, the accuracy of the estimation is comparatively low.

Our study is the first study to obtain such higher accuracy of the AGB estimation using L-band HV polarized backscatter in the mangrove forest. Therefore, the findings of our study depict that L-band ALOS-2 PALSAR-2 data has a great potential to estimate AGB with higher accuracy in the mangrove forest as in the inland forest in the tropical and sub-tropical region. Thus, the findings of our study can contribute to the MRV system of UN-REDD+ for monitoring the mangrove forest management in the tropics and subtropics. However, more research is needed to confirm the findings of our research.

6. CONCLUSION

6.1. Conclusion

This study assessed the relationship between forest parameters of the mangrove forest and the backscatter coefficients of HV and HH polarized L-band PALSAR-2. The AGB of the mangrove forest was modeled with HV and HH polarized backscatter values of PALSAR-2 using a simple linear regression. Although the AGB estimation showed the tendency to saturate, the simple linear model using HV backscatter showed the higher accuracy to estimate AGB. Therefore, the simple linear regression model was used to map the AGB/carbon stock in the study area. The main findings of this research are described briefly in the following sections.

RQ 1: What is the relationship between mangrove forest parameters (DBH, BA and tree height) and ALOS-2 PALSAR-2 backscatter coefficients?

The relationship between BA, DBH and Tree Height with PALSAR-2 backscatter coefficients were modeled using linear regression model. Among them, BA showed a high correlation with HV backscatter values at R^2 of 0.78. The tree DBH and HV polarized backscatter had a moderate relationship at R^2 of 0.51. However, the relationship between the tree height and HV backscatter coefficients was quite weak at R^2 of 0.25. On the contrary, the relationship between all these forest parameters and HH backscatter coefficients showed very weak relationships.

RQ 2: What is the relationship between HV and/or HH backscatter of ALOS-2 PALSAR-2 and AGB/carbon stock in the mangrove?

The relationship between cross (HV) polarized L-band PALSAR-2, and AGB showed higher accuracy with R^2 of 0.89 and RMSE of 23 tons ha^{-1} . The inclusion of like polarized (HH) backscatter values in the model did not improve the accuracy of the model prediction; rather it was the same as the simple linear regression model.

RQ 3: What is the saturation point of AGB/carbon stock estimation in the mangrove forest in relation to the ALOS-2 PALSAR-2 backscatter coefficients?

The L-band HV polarized backscatter values depicted the presence of saturation to estimate AGB at 216.9 tons ha^{-1} . This is an indication of the limitation of AGB estimation where the mean AGB is > 216.9 tons ha^{-1} using L-band SAR.

RQ 4: what is the AGB/carbon stock in the study area and how to map it?

The amount of estimated AGB in the study area ranged between 1 and 350 tons/ha. The estimated AGB was classified into five classes, and the majority of AGB estimates were found to be ranged from 100 to 200 tons/ha. The total amount of AGB in the study area is 13,719 tons, and the corresponding figure for carbon was 6860 tons. The accuracy of the estimation was observed at R^2 of 0.89 and RMSE of 22.69.

6.2. Recommendations

The pre-processing and processing of PALSAR data should be done carefully. Given the context of mangrove forest affected by tides and intersected by water channels, speckle filtering may affect the accuracy of AGB estimates. In such cases, filtering can be avoided to improve the accuracy of the AGB estimates.

Advanced GPS instrument should be used to establish the location of the plot in the field. This will avoid errors associated with extraction of plot backscatter.

L-band SAR data needs geometric correction using DEM data. The use of high-resolution DEM data for geometric correction of the L-band SAR data should be used to maintain the spatial resolution of the original backscatter image.

The HV polarization PALSAR backscatter coefficients show a higher accuracy in estimating AGB beyond the saturation level in our study. Therefore, HV polarization is recommended to model AGB estimation in the mangrove forest to test if it results in the same accuracy in another mangrove forest. Another aspect to explore is that up to what level PALSAR-2 can estimate AGB with similar accuracy in the mangrove forest. Most importantly, can PALSAR be used to estimate AGB in the natural mangrove forest with a similar accuracy?

LIST OF REFERENCES

- Abd Rahman, M., Abu Bakar, M., Razak, K., Rasib, A., Kanniah, K., Wan Kadir, W., ... Abd Latif, Z. (2017). Non-Destructive, Laser-Based Individual Tree Aboveground Biomass Estimation in a Tropical Rainforest. *Forests*, 8(3), 86. <https://doi.org/10.3390/f8030086>
- Abdul Rashid, A. M., Shamsudin, I., Ismail, P., & Fletcher, S. C. (2009). The role of FRIM in addressing climate-change issues. Research Pamphlet No. 128. *Forest Research Institute Malaysia, Kepong*.
- Ager, T. P. (2011). An introduction to synthetic aperture radar imaging. *Oceanography*, 24(3), 162–173. <https://doi.org/10.5670/oceanog.2011.65>
- Alongi, D. M. (2002). Present state and future of the world's mangrove forests. *Environmental Conservation*, 29(03). <https://doi.org/10.1017/S0376892902000231>
- Altman, D. G., & Bland, J. M. (1995). Statistics notes: The normal distribution. *BMJ*, 310(6975), 298–298. <https://doi.org/10.1136/bmj.310.6975.298>
- Anonymous. (2018). *Imaging Radar: ITC course materials, Univerisy of Twente, Enschede, the Netherlands*.
- Argamosa, R. J. L., Blanco, A. C., Baloloy, A. B., Candido, C. G., Dumalag, J. B. L. C., Dimapilis, L. L. C., & Paringit, E. C. (2018). Modelling above ground biomass of mangrove forest using Sentinel-1 imagery, *IV*, 7–10.
- Asmare, M. F. (2013). *Airborne LiDAR data and VHR WorldView satellite imagery to support community based forest certification in Chitwan, Nepal (MSc Thesis)*. ITC, University of Twente, The Netherlands. Retrieved from https://www.itc.nl/library/papers_2013/msc/nrm/asmare.pdf%0A%0A
- Asner, G. P. (2001a). Cloud cover in Landsat observations of the Brazilian Amazon. *International Journal of Remote Sensing*, 22(18), 3855–3862. <https://doi.org/10.1080/01431160010006926>
- Asner, G. P. (2001b). Cloud cover in Landsat observations of the Brazilian Amazon. *International Journal of Remote Sensing*, 22(18), 3855–3862. <https://doi.org/10.1080/01431160010006926>
- Barbier, E. B., Hacker, S. D., Kennedy, C., Koch, E. W., Stier, A. C., & Silliman, B. R. (2011). The value of estuarine and coastal ecosystem services. *Ecological Monographs*, 81(2), 169–193. <https://doi.org/10.1890/10-1510.1>
- Bosma, R., Sidik, A. S., van Zwieten, P., Aditya, A., & Visser, L. (2012). Challenges of a transition to a sustainably managed shrimp culture agro-ecosystem in the Mahakam delta, East Kalimantan, Indonesia. *Wetlands Ecology and Management*, 20(2), 89–99. <https://doi.org/10.1007/s11273-011-9244-0>
- Bouillon, S., Borges, A. V., Castañeda-Moya, E., Diele, K., Dittmar, T., Duke, N. C., ... Twilley, R. R. (2008). Mangrove production and carbon sinks: A revision of global budget estimates. *Global Biogeochemical Cycles*, 22(2), n/a-n/a. <https://doi.org/10.1029/2007GB003052>
- Brown, S. (1997). *Estimating biomass and biomass change of tropical forests, FAO FORESTRY PAPER. 134*. Rome. Retrieved from <http://www.fao.org/docrep/w4095e/w4095e00.HTM>
- Brown, S. (2002). Measuring carbon in forests: Current status and future challenges. *Environmental Pollution*, 116(3), 363–372. [https://doi.org/10.1016/S0269-7491\(01\)00212-3](https://doi.org/10.1016/S0269-7491(01)00212-3)
- Carreiras, J.M.B., Vasconcelos, M.J., & Lucas, R. M. (2012). Understanding the relationship between aboveground biomass and ALOS PALSAR data in the forests of Guinea-Bissau (West Africa). *Remote Sensing of Environment*, 121, 426–442. <https://doi.org/10.1016/j.rse.2012.02.012>
- Carver, K. (1988). "SAR Synthetic Aperture Radar – Earth Observing System." NASA National Aeronautics & Space Administration. Instrument Panel Report. Vol IIf. In *Radar Imaging From Space*.
- Chave, J., Andalo, C., Brown, S., Cairns, M. A., Chambers, J. Q., Eamus, D., ... Yamakura, T. (2005). Tree allometry and improved estimation of carbon stocks and balance in tropical forests. *Oecologia*, 145(1), 87–99. <https://doi.org/10.1007/s00442-005-0100-x>
- Chave, J., Condit, R., Aguilar, S., Hernandez, A., Lao, S., & Perez, R. (2004). Error propagation and scaling for tropical forest biomass estimates. *Philosophical Transactions of the Royal Society of London. Series B, Biological Sciences*, 359(1443), 409–420. <https://doi.org/10.1098/rstb.2003.1425>
- Chave, J., Coomes, D., Jansen, S., Lewis, S. L., Swenson, N. G., & Zanne, A. E. (2009). Towards a worldwide wood economics spectrum. *Ecology Letters*, 12(4), 351–366. <https://doi.org/10.1111/j.1461-0248.2009.01285.x>
- Chave, J., Réjou-Méchain, M., Búrquez, A., Chidumayo, E., Colgan, M. S., Delitti, W. B. C., ... Vieilledent, G. (2014). Improved allometric models to estimate the aboveground biomass of tropical trees. *Global Change Biology*, 20(10), 3177–3190. <https://doi.org/10.1111/gcb.12629>

- Chen, E., Li, Z., Ling, F., Lu, Y., He, Q., & Fan, F. (2009). Forest volume density estimation capability of Alos Palsar data over hilly region. In *Proceedings of 4th International Workshop on Science and Applications of SAR Polarimetry and Polarimetric Interferometry—PolInSAR*.
- Chmura, G. L., Anisfeld, S. C., Cahoon, D. R., & Lynch, J. C. (2003). Global carbon sequestration in tidal, saline wetland soils. *Global Biogeochemical Cycles*, 17(4), n/a-n/a. <https://doi.org/10.1029/2002GB001917>
- Clough, B. F., Dixon, P., & Dalhaus, O. (1997). Allometric Relationships for Estimating Biomass in Multi-stemmed Mangrove Trees. *Australian Journal of Botany*, 45(6), 1023. <https://doi.org/10.1071/BT96075>
- Combes Motel, P., Pirard, R., & Combes, J. L. (2009). A methodology to estimate impacts of domestic policies on deforestation: Compensated Successful Efforts for “avoided deforestation” (REDD). *Ecological Economics*, 68(3), 680–691. <https://doi.org/10.1016/j.ecolecon.2008.06.001>
- CRISP (Centre for Remote Imaging, S. and P. (2001). SAR Imaging - Frequency, Polarisation and Incident Angle. Retrieved May 1, 2019, from <https://crisp.nus.edu.sg/~research/tutorial/freqpol.htm>
- Curlander, J. C. (1982). Location of Spaceborne Sar Imagery. *IEEE Transactions on Geoscience and Remote Sensing*, GE-20(3), 359–364. <https://doi.org/10.1109/TGRS.1982.350455>
- Cutler, M. E. J., Boyd, D. S., Foody, G. M., & Vetrivel, A. (2012). Estimating tropical forest biomass with a combination of SAR image texture and Landsat TM data: An assessment of predictions between regions. *ISPRS Journal of Photogrammetry and Remote Sensing*, 70, 66–77. <https://doi.org/10.1016/j.isprsjprs.2012.03.011>
- De Oliveira, A. A., & Mori, S. A. (1999). A central Amazonian terra firme forest. I. High tree species richness on poor soils. *Biodiversity & Conservation*, 8(9), 1219–1244. <https://doi.org/10.1023/A:1008908615271>
- de Souza Pereira, F. R., Kampel, M., & Cunha-Lignon, M. (2016). Mangrove vegetation structure in Southeast Brazil from phased array L-band synthetic aperture radar data. *Journal of Applied Remote Sensing*, 10(3), 036021. <https://doi.org/10.1117/1.JRS.10.036021>
- Deng, S., Katoh, M., Guan, Q., Yin, N., & Li, M. (2014). Estimating Forest Aboveground Biomass by Combining ALOS PALSAR and WorldView-2 Data: A Case Study at Purple Mountain National Park, Nanjing, China. *Remote Sensing*, 6(9), 7878–7910. <https://doi.org/10.3390/rs6097878>
- DLR. (2013). Microwaves and Radar Institute - Mission Concept-DLR. Retrieved May 1, 2019, from https://www.dlr.de/hr/en/desktopdefault.aspx/tabid-8113/14171_read-35852/
- Dobson, M. C., Ulaby, F. T., LeToan, T., Beaudoin, A., Kasischke, E. S., & Christensen, N. (1992). Dependence of radar backscatter on coniferous forest biomass. *IEEE Transactions on Geoscience and Remote Sensing*, 30(2), 412–415. <https://doi.org/10.1109/36.134090>
- Donato, D. C., Kauffman, J. B., Murdiyarso, D., Kurnianto, S., Stidham, M., & Kanninen, M. (2011). Mangroves among the most carbon-rich forests in the tropics. *Nature Geoscience*, 4(5), 293–297. <https://doi.org/10.1038/ngeo1123>
- Du, H., Zhou, G., Ge, H., Fan, W., Xu, X., Fan, W., & Shi, Y. (2012). Satellite-based carbon stock estimation for bamboo forest with a non-linear partial least square regression technique. *International Journal of Remote Sensing*, 33(6), 1917–1933. <https://doi.org/10.1080/01431161.2011.603379>
- Dube, T., & Mutanga, O. (2015). Evaluating the utility of the medium-spatial resolution Landsat 8 multispectral sensor in quantifying aboveground biomass in uMgeni catchment, South Africa. *ISPRS Journal of Photogrammetry and Remote Sensing*, 101, 36–46. <https://doi.org/10.1016/j.isprsjprs.2014.11.001>
- Duncanson, L. I., Niemann, K. O., & Wulder, M. A. (2010). Estimating forest canopy height and terrain relief from GLAS waveform metrics. *Remote Sensing of Environment*, 114(1), 138–154. <https://doi.org/10.1016/j.rse.2009.08.018>
- Dutrieux, E. (1991). Study of the ecological functioning of the Mahakam delta (east Kalimantan, Indonesia). *Estuarine, Coastal and Shelf Science*, 32(4), 415–420. [https://doi.org/10.1016/0272-7714\(91\)90053-E](https://doi.org/10.1016/0272-7714(91)90053-E)
- E. Kushan. (2016). The importance of Mangrove wetlands, it’s pollution and threats. Retrieved November 10, 2018, from <https://www.slideshare.net/kushane1/mangrove-its-threats>
- Emery, W., & Camps, A. (2017). Radar. In W. Emery & A. B. T.-I. to S. R. S. Camps (Eds.), *Introduction to Satellite Remote Sensing* (pp. 291–453). Elsevier. <https://doi.org/https://doi.org/10.1016/B978-0-12-809254-5.00005-1>
- ESA. (2002). Geometry Glossary-ESA Earth Online. Retrieved December 20, 2018, from <https://earth.esa.int/handbooks/asar/CNTR5-5.html>
- ESA. (2009a). Sentinel 1 Toolbox. Retrieved January 28, 2019, from <http://step.esa.int/main/toolboxes/sentinel-1-toolbox/>
- ESA. (2009b). SNAP. Retrieved January 28, 2019, from <http://step.esa.int/main/toolboxes/snap/>
- ESA. (2015). PALSAR-ESA EARTH OBSERVATION DATA: Sensor Performance, products and

- algorithms. Retrieved May 27, 2018, from <https://earth.esa.int/web/sppa/mission-performance/esa-3rd-party-missions/alos/palsar/sensor-description>
- Estornell, J., Ruiz, L. A., Velázquez-Martí, B., & Fernández-Sarría, A. (2011). Estimation of shrub biomass by airborne LiDAR data in small forest stands. *Forest Ecology and Management*, 262(9), 1697–1703. <https://doi.org/10.1016/j.foreco.2011.07.026>
- Evans, D. L., Farr, T. G., van Zyl, J. J., & Zebker, H. A. (1988). Radar polarimetry: analysis tools and applications. *IEEE Transactions on Geoscience and Remote Sensing*, 26(6), 774–789. <https://doi.org/10.1109/36.7709>
- FAO. (2007). The world's mangroves 1980-2005. Retrieved August 15, 2018, from <https://forestsnews.cifor.org/31178/indonesian-mangroves-special-fact-file-a-global-treasure-under-threat?fnl=en>
- FAO. (2018a). REDD+ Reducing Emissions from Deforestation and Forest Degradation. Retrieved June 21, 2018, from <http://www.fao.org/redd/overview/en/>
- FAO. (2018b). REDD+ Reducing Emissions from Deforestation and Forest Degradation. Retrieved June 4, 2018, from <http://www.fao.org/redd/initiatives/un-redd/en/>
- FFPRI. (2012). *REDD plus cookbook: how to measure and monitor forest carbon*. Tsukuba, Japan. Retrieved from <https://theredddesk.org/resources/redd-plus-cookbook-how-measure-and-monitor-forest-carbon>
- Field, A. (2009). *Discovering Statistics Using IBM SPSS* (3rd ed.). London: SAGE publications Ltd.
- Ghasemi, N., Sahebi, M. R., & Mohammadzadeh, A. (2011). A review on biomass estimation methods using synthetic aperture radar data. *International Journal Ofgeomatics and Geosciences*, 1(4), 776–788.
- Gibbs, H. K., Brown, S., Niles, J. O., & Foley, J. A. (2007). Monitoring and estimating tropical forest carbon stocks: making REDD a reality. *Environmental Research Letters*, 2(2007), 045023. <https://doi.org/10.1088/1748-9326/2/4/045023>
- Gibbs, H. K., & Herold, M. (2007). Tropical deforestation and greenhouse gas emissions. *Environmental Research Letters*, 2(4), 045021. <https://doi.org/10.1088/1748-9326/2/4/045021>
- Giri, C., Ochieng, E., Tieszen, L. L., Zhu, Z., Singh, A., Loveland, T., ... Duke, N. (2011). Status and distribution of mangrove forests of the world using earth observation satellite data. *Global Ecology and Biogeography*, 20(1), 154–159. <https://doi.org/10.1111/j.1466-8238.2010.00584.x>
- Gobakken, T., & Næsset, E. (2008). Assessing effects of laser point density, ground sampling intensity, and field sample plot size on biophysical stand properties derived from airborne laser scanner data. *Canadian Journal of Forest Research*, 38(5), 1095–1109. <https://doi.org/10.1139/X07-219>
- Goh, J., Miettinen, J., Chia, A., Chew, P., & Liew, S. (2013). Biomass estimation in humid tropical forest using a combination of ALOS PALSAR and Spot 5 satellite imagery. *Asian Journal of Geoinformatics*, 13.
- Grassi, G., Monni, S., Federici, S., Achard, F., & Mollicone, D. (2008). Applying the conservativeness principle to REDD to deal with the uncertainties of the estimates. *Environmental Research Letters*, 3(3). <https://doi.org/10.1088/1748-9326/3/3/035005>
- Hamdan, O., Aziz, H. K., & Hasmadi, I. M. (2014). L-band ALOS PALSAR for biomass estimation of Matang Mangroves, Malaysia. *Remote Sensing of Environment*, (April 2018). <https://doi.org/10.1016/j.rse.2014.04.029>
- Hamdan, O., Ismail, M. H., Khali, H., Norizah, K., & Helmi, S. (2015). L-band saturation level for aboveground biomass of dipterocarp forests in peninsular Malaysia. *Journal of Tropical Forest Science*, 27, 388–399.
- Hamdan, O., Khali, H. A., & Abd Rahman, K. (2011). Remotely sensed L-band SAR Data for tropical forest biomass estimation. *Journal of Tropical Forest Science*, 23(3), 318–327.
- Hamilton, S. E., & Friess, D. A. (2018). Global carbon stocks and potential emissions due to mangrove deforestation from 2000 to 2012. *Nature Climate Change*, 8(3), 240–244. <https://doi.org/10.1038/s41558-018-0090-4>
- Hartini, S., Saputro, G. B., Yulianto, M., & Suprajaka. (2010). Assessing the used of remotely sensed data for mapping mangroves Indonesia. In *10th WSEAS/LASME International Conference on Electric Power Systems, High Voltages, Electric Machines, POWER'10, 6th WSEAS International Conference on Remote Sensing, REMOTE'10* (pp. 210–215). <https://doi.org/10.4240/wjgs.v8.i2.115>
- Henderson, F. M., & Lewis, A. J. (1998). *Principles and Applications of Imaging Radar, Manual of Remote Sensing, 3rd Edition, Volume 2*. United States.
- Hertz, H. (2008). Overview of Polarimetric Radar Imaging. In *Polarimetric Radar Imaging* (1st ed., p. 432). Taylor & Francis Group, LLC.
- Hirata, Y., Tabuchi, R., Patanaponpaiboon, P., Pongparn, S., Yoneda, R., & Fujioka, Y. (2014). Estimation of aboveground biomass in mangrove forests using high-resolution satellite data. *Journal of Forest*

- Research*, 19(1), 34–41. <https://doi.org/10.1007/s10310-013-0402-5>
- Ho Tong Minh, D., Le Toan, T., Rocca, F., Tebaldini, S., Villard, L., Réjou-Méchain, M., ... Chave, J. (2016). SAR tomography for the retrieval of forest biomass and height: Cross-validation at two tropical forest sites in French Guiana. *Remote Sensing of Environment*, 175, 138–147. <https://doi.org/10.1016/j.rse.2015.12.037>
- Humboldt State University. (2016). Interpreting Imaging Radar. Retrieved January 5, 2019, from http://gsp.humboldt.edu/olm_2015/Courses/GSP_216_Online/lesson7-2/interpreting-radar.html
- Hussin, Y. A. (1990). *The effects of polarization and incidence angle on radar backscatter from forest cover*. Fort Collins: Colorado State University.
- Hussin, Y. A., Reich, R. M., & Hoffer, R. M. (1991). Estimating splash pine biomass using radar backscatter. *IEEE Transactions on Geoscience and Remote Sensing*, 29(3), 427–431. <https://doi.org/10.1109/36.79433>
- Hyde, P., Nelson, R., Kimes, D., & Levine, E. (2007). Exploring LiDAR–RaDAR synergy—predicting aboveground biomass in a southwestern ponderosa pine forest using LiDAR, SAR and InSAR. *Remote Sensing of Environment*, 106(1), 28–38. <https://doi.org/10.1016/j.rse.2006.07.017>
- Imhoff, M. L. (1995). Radar backscatter and biomass saturation: ramifications for global biomass inventory. *IEEE Transactions on Geoscience and Remote Sensing*, 33(2), 511–518. <https://doi.org/10.1109/36.377953>
- Imhoff, M. L., Vermillion, C., Story, M. H., Choudhury, A. M., Gafoor, A., & Polcyn, F. (1987). Monsoon flood boundary delineation and damage assessment using spaceborne imaging radar and Landsat data. *Photogrammetric Engineering and Remote Sensing*, 53(4).
- Imhoff, M., Story, M., Vermillion, C., Khan, F., & Polcyn, F. (1986). Forest Canopy Characterization and Vegetation Penetration Assessment with Space-Borne Radar. *IEEE Transactions on Geoscience and Remote Sensing*, GE-24(4), 535–542. <https://doi.org/10.1109/TGRS.1986.289668>
- IPCC. (2007). Climate change 2007: Synthesis report. *Contribution of Working Groups I, II and III to the Fourth Assessment Report of the Intergovernmental Panel on Climate Change*. IPCC Geneva, Switzerland.
- JAXA. (2009). About ALOS-PALSAR. Retrieved June 19, 2018, from <https://www.eorc.jaxa.jp/ALOS/en/about/palsar.htm>
- JAXA. (2016). ALOS-2 Project / PALSAR-2. Retrieved January 6, 2019, from <https://www.eorc.jaxa.jp/ALOS-2/en/about/palsar2.htm>
- Jensen, J. R. (2007). *Remote Sensing of the Environment: An Earth Resource Perspective* (2nd ed.). Upper Saddle River, NJ: Pearson Prentice Hall.
- Jiang, W., Yu, A., Dong, Z., & Wang, Q. (2016). Comparison and Analysis of Geometric Correction Models of Spaceborne SAR. *Sensors*, 16(7), 973. <https://doi.org/10.3390/s16070973>
- Joshi, N., Mitchard, E., Schumacher, J., Johannsen, V., Saatchi, S., & Fensholt, R. (2015). L-Band SAR Backscatter Related to Forest Cover, Height and Aboveground Biomass at Multiple Spatial Scales across Denmark. *Remote Sensing*, 7(4), 4442–4472. <https://doi.org/10.3390/rs70404442>
- Kaasalainen, S., Holopainen, M., Karjalainen, M., Vastaranta, M., Kankare, V., Karila, K., & Osmanoglu, B. (2015). Combining Lidar and Synthetic Aperture Radar Data to Estimate Forest Biomass: Status and Prospects. *Forests*, 6(12), 252–270. <https://doi.org/10.3390/f6010252>
- Kankaku, Y., Sagisaka, M., & Suzuki, S. (2014). PALSAR-2 launch and early orbit status. In *2014 IEEE Geoscience and Remote Sensing Symposium* (pp. 3410–3412). IEEE. <https://doi.org/10.1109/IGARSS.2014.6947213>
- Kankaku, Y., Suzuki, S., & Osawa, Y. (2013). ALOS-2 mission and development status. In *2013 IEEE International Geoscience and Remote Sensing Symposium - IGARSS* (pp. 2396–2399). IEEE. <https://doi.org/10.1109/IGARSS.2013.6723302>
- Kelsey, K., & Neff, J. (2014). Estimates of Aboveground Biomass from Texture Analysis of Landsat Imagery. *Remote Sensing*, 6(7), 6407–6422. <https://doi.org/10.3390/rs6076407>
- Kershaw, J. A., Ducey, M. J., Beers, T. W., & Husch, B. (2016). *Forest mensuration* (5th ed.). New York: John Wiley.
- Komiyama, A., Ong, J. E., & Pongpam, S. (2008). Allometry, biomass, and productivity of mangrove forests: A review. *Aquatic Botany*, 89(2), 128–137. <https://doi.org/10.1016/j.aquabot.2007.12.006>
- Kovacs, J. M., Lu, X. X., Flores-Verdugo, F., Zhang, C., Flores de Santiago, F., & Jiao, X. (2013). Applications of ALOS PALSAR for monitoring biophysical parameters of a degraded black mangrove (*Avicennia germinans*) forest. *ISPRS Journal of Photogrammetry and Remote Sensing*, 82, 102–111. <https://doi.org/10.1016/j.isprsjprs.2013.05.004>
- Kristensen, E., Bouillon, S., Dittmar, T., & Marchand, C. (2008). Organic carbon dynamics in mangrove ecosystems: A review. *Aquatic Botany*, 89(2), 201–219. <https://doi.org/10.1016/j.aquabot.2007.12.005>
- Kuenzer, C., Bluemel, A., Gebhardt, S., Quoc, T. V., & Dech, S. (2011). Remote Sensing of Mangrove

- Ecosystems: A Review. *Remote Sensing*, 3(5), 878–928. <https://doi.org/10.3390/rs3050878>
- Kumar, S., Khati, U. G., Chandola, S., Agrawal, S., & Kushwaha, S. P. S. (2017). Polarimetric SAR Interferometry based modeling for tree height and aboveground biomass retrieval in a tropical deciduous forest. *Advances in Space Research*, 60(3), 571–586. <https://doi.org/10.1016/j.asr.2017.04.018>
- Kurvonen, L., Pulliainen, J., & Hallikainen, M. (1999). Retrieval of biomass in boreal forests from multitemporal ERS-1 and JERS-1 SAR images. *IEEE Transactions on Geoscience and Remote Sensing*, 37(1), 198–205. <https://doi.org/10.1109/36.739154>
- Kusmana, C. (2014). Distribution and Current Status of Mangrove Forests in Indonesia. In *Mangrove Ecosystems of Asia* (pp. 37–60). New York, NY: Springer New York. https://doi.org/10.1007/978-1-4614-8582-7_3
- Laar, A. van, & Akça, A. (2007). *Forest Mensuration* (Vol. 13). Dordrecht: Springer Netherlands. <https://doi.org/10.1126/science.24.624.760>
- Larsen, D. R. (2018). Natural Resources Biometrics. Retrieved December 25, 2018, from <http://oak.snr.missouri.edu/nr3110/topics/basalarea.php>
- Le Toan, T., Beaudoin, A., Riom, J., & Guyon, D. (1992a). Relating forest biomass to SAR data. *IEEE Transactions on Geoscience and Remote Sensing*, 30(2), 403–411. <https://doi.org/10.1109/36.134089>
- Le Toan, T., Beaudoin, A., Riom, J., & Guyon, D. (1992b). Relating Forest Parameters To Sar Data. In *[Proceedings] IGARSS'91 Remote Sensing: Global Monitoring for Earth Management* (Vol. 2, pp. 689–692). IEEE. <https://doi.org/10.1109/IGARSS.1991.579979>
- Lee, J.-S., & Pottier, E. (2009). *Polarimetric Radar Imaging: From Basics to Applications*. Chapman and Hall/CRC: ProQuest Ebook Central. Retrieved from <https://ebookcentral.proquest.com/lib/itc/detail.action?docID=427062>.
- Liang, X., Kankare, V., Hyypä, J., Wang, Y., Kukko, A., Haggrén, H., ... Vastaranta, M. (2016). Terrestrial laser scanning in forest inventories. *ISPRS Journal of Photogrammetry and Remote Sensing*, 115, 63–77. <https://doi.org/10.1016/j.isprsjprs.2016.01.006>
- Lillesand, T. M., & Kiefer, R. W. (1994). *Remote Sensing and Image Interpretation*. John Wiley and Sons, Inc. (3rd ed.). Hoboken, 750.
- Ling, F., & Dai, Y. (2012). Understanding the enhanced backscatter of coastal forest plantation in L-band synthetic aperture radar images. In *2012 First International Conference on Agro- Geoinformatics (Agro- Geoinformatics)* (pp. 1–4). IEEE. <https://doi.org/10.1109/Agro-Geoinformatics.2012.6311619>
- Logan, T. L. (1997). Terrain Correction of Synthetic Aperture Radar Imagery Using the Cray T 3.
- Lu, D., Mausel, P., Brondizio, E., & Moran, E. (2004). Relationships between forest stand parameters and Landsat TM spectral responses in the Brazilian Amazon Basin. *Forest Ecology and Management*, 198(1–3), 149–167. <https://doi.org/10.1016/j.foreco.2004.03.048>
- Lucas, R., Fairfax, R., Fensham, R., Accad, A., Carreiras, J., Kelley, J., ... Shimada, M. (2010). An Evaluation of the ALOS PALSAR L-Band Backscatter—Above Ground Biomass Relationship Queensland, Australia: Impacts of Surface Moisture Condition and Vegetation Structure. *Ieee Journal of Selected Topics in Applied Earth Observations and Remote Sensing*, 3(4), 576–593.
- Lucas, R. M., Mitchell, A. L., & Armston, J. (2015). Measurement of Forest Above-Ground Biomass Using Active and Passive Remote Sensing at Large (Subnational to Global) Scales. *Current Forestry Reports*, 1(3), 162–177. <https://doi.org/10.1007/s40725-015-0021-9>
- Lucas, R. M., Mitchell, A. L., Rosenqvist, A., Proisy, C., Melius, A., & Ticehurst, C. (2007). The potential of L-band SAR for quantifying mangrove characteristics and change: case studies from the tropics. *Aquatic Conservation: Marine and Freshwater Ecosystems*, 17(3), 245–264. <https://doi.org/10.1002/aqc.833>
- Luo, S., Wang, C., Xi, X., Pan, F., Peng, D., Zou, J., ... Qin, H. (2017). Fusion of airborne LiDAR data and hyperspectral imagery for aboveground and belowground forest biomass estimation. *Ecological Indicators*. <https://doi.org/10.1016/j.ecolind.2016.10.001>
- Manavalan, R. (2018). Review of synthetic aperture radar frequency, polarization, and incidence angle data for mapping the inundated regions. *Journal of Applied Remote Sensing*, 12(02), 1. <https://doi.org/10.1117/1.JRS.12.021501>
- Masolele, R. N. (2018). *ALOS-2 PALSAR-2 L-band cross-polarized radar data analysis for modelling above-ground biomass/ carbon stock and carbon sequestration of tropical rainforest, Berkelah, Malaysia (MSc Thesis)*. Faculty of Geo-Information and Earth Observation (ITC), University of Twente, The Netherlands. Retrieved from http://www.itc.nl/library/papers_2018/msc/nrm/masolele.pdf
- Mermoz, S., Rejou-Méchain, M., Villard, L., Le Toan, T., Rossi, V., Gourlet-FliMermoz, S. (2014). Biomass of dense forests related to L-band SAR backscatter? *IEEE Geoscience and Remote Sensing*, (May). <https://doi.org/10.1109/IGARSS.2014.6946605>

- Moore, D. S., McCabe, G. P., & Craig, B. A. (2017). *Introduction to the practice of statistics*. (9th, Ed.). New York : W.H. Freeman, Macmillan Learning.
- Moreira, A., Prats-Iraola, P., Younis, M., Krieger, G., Hajnsek, I., & Papathanassiou, K. P. (2013). A tutorial on synthetic aperture radar. *IEEE Geoscience and Remote Sensing Magazine*, 1(1), 6–43. <https://doi.org/10.1109/MGRS.2013.2248301>
- Morel, A. C., Saatchi, S. S., Malhi, Y., Berry, N. J., Banin, L., Burslem, D., ... Ong, R. C. (2011). Estimating aboveground biomass in forest and oil palm plantation in Sabah, Malaysian Borneo using ALOS PALSAR data. *Forest Ecology and Management*, 262(9), 1786–1798. <https://doi.org/https://doi.org/10.1016/j.foreco.2011.07.008>
- Mougin, E., Proisy, C., Marty, G., Fromard, F., Puig, H., Betoulle, J. L., & Rudant, J. P. (1999). Multifrequency and multipolarization radar backscattering from mangrove forests. *IEEE Transactions on Geoscience and Remote Sensing*, 37(1), 94–102. <https://doi.org/10.1109/36.739128>
- Mouginis-Mark, P. (2001). Virtually Hawaii: Radar Remote Sensing Example. Retrieved January 27, 2019, from http://satftp.soest.hawaii.edu/space/hawaii/vfts/kilauea/radar_ex/page2.html
- NASA. (1987). *SAR (Synthetic Aperture Radar): Earth observing system*. Retrieved from <https://ntrs.nasa.gov/search.jsp?R=19880005902>
- Natural Resources Canada. (2014). Polarization in radar systems. Retrieved January 6, 2019, from <https://www.nrcan.gc.ca/node/9567>
- Natural Resources Canada. (2015a). Polarimetric scattering. Retrieved January 6, 2019, from <https://www.nrcan.gc.ca/node/9547%0A%0A>
- Natural Resources Canada. (2015b). Radar Polarimetry. Retrieved January 6, 2019, from <https://www.nrcan.gc.ca/earth-sciences/geomatics/satellite-imagery-air-photos/satellite-imagery-products/educational-resources/9275>
- Neumann, M., Saatchi, S. S., Ulander, L. M. H., & Fransson, J. E. S. (2012). Assessing Performance of L- and P-Band Polarimetric Interferometric SAR Data in Estimating, 50(3), 714–726.
- Nga, T. N. (2010). *Estimation and mapping of above ground biomass for the assessment and mapping of carbon stocks in tropical forest using SAR data- a case study in Afram Headwaters Forest, Ghana (MSc Thesis)*. ITC, University of Twente, The Netherlands. Retrieved from http://www.itc.nl/library/papers_2010/msc/nrm/nga.pdf
- Odipo, V., Nickless, A., Berger, C., Baade, J., Urbazaev, M., Walther, C., & Schmulius, C. (2016). Assessment of Aboveground Woody Biomass Dynamics Using Terrestrial Laser Scanner and L-Band ALOS PALSAR Data in South African Savanna. *Forests*, 7(12), 294. <https://doi.org/10.3390/f7120294>
- Omar, H., Ismail, M. H., Hamzah, K. A., Shafri, H. Z. M., & Kamarudin, N. (2015). Estimating biomass in logged tropical forest using L-band SAR (PALSAR) data and GIS. *Sains Malaysiana*, 44(8), 1085–1093. <https://doi.org/10.17576/jsm-2015-4408-02>
- Ormsby, J. P., Blanchard, B. J., & Blanchard, A. J. (1985). Detection of lowland flooding using active microwave systems. *Photogrammetric Engineering and Remote Sensing*, 51(3).
- Pan, Y., Birdsey, R. A., Fang, J., Houghton, R., Kauppi, P. E., Kurz, W. A., ... Hayes, D. (2011). A large and persistent carbon sink in the world's forests. *Science (New York, N.Y.)*, 333(6045), 988–93. <https://doi.org/10.1126/science.1201609>
- Pham, T. D., & Yoshino, K. (2017). Aboveground biomass estimation of mangrove species using ALOS-2 PALSAR imagery in Hai Phong City, Vietnam. *Journal of Applied Remote Sensing*, 11(2), 026010. <https://doi.org/10.1117/1.JRS.11.026010>
- Pham, T. D., Yoshino, K., & Bui, D. T. (2017). Biomass estimation of *Sonneratia caseolaris* (L.) Engler at a coastal area of Hai Phong city (Vietnam) using ALOS-2 PALSAR imagery and GIS-based multi-layer perceptron neural networks. *GIScience & Remote Sensing*, 54(3), 329–353. <https://doi.org/10.1080/15481603.2016.1269869>
- Pham, T. D., Yoshino, K., Le, N. N., & Bui, D. T. (2018). Estimating aboveground biomass of a mangrove plantation on the Northern coast of Vietnam using machine learning techniques with an integration of ALOS-2 PALSAR-2 and Sentinel-2A data. *International Journal of Remote Sensing*, 39(22), 7761–7788. <https://doi.org/10.1080/01431161.2018.1471544>
- Phillips, O., Baker, T., Feldpausch, T., & Brien, R. (2006). Field manual for establishment and re-measurement (RAINFOR).
- Powell, S. L., Cohen, W. B., Healey, S. P., Kennedy, R. E., Moisen, G. G., Pierce, K. B., & Ohmann, J. L. (2010). Quantification of live aboveground forest biomass dynamics with Landsat time-series and field inventory data: A comparison of empirical modeling approaches. *Remote Sensing of Environment*, 114(5),

- 1053–1068. <https://doi.org/10.1016/j.rse.2009.12.018>
- Proisy, C. (2000). Interpretation of Polarimetric Radar Signatures of Mangrove Forests. *Remote Sensing of Environment*, 71(1), 56–66. [https://doi.org/10.1016/S0034-4257\(99\)00064-4](https://doi.org/10.1016/S0034-4257(99)00064-4)
- Quinn, G. P., & Keough, M. J. (2002). *Experimental Design and Data Analysis for Biologists*. Cambridge: Cambridge University Press. <https://doi.org/10.1017/CBO9780511806384>
- Reuben, S. (2009). Assessment of the status of the development of the standards for the Terrestrial Essential Climate Variables. GTOS 67. Retrieved August 14, 2018, from <http://www.fao.org/docrep/012/i1238e/i1238e00.htm>
- Richards, J. A. (2009). *Remote Sensing with Imaging Radar*. Berlin, Heidelberg: Springer Berlin Heidelberg. <https://doi.org/10.1007/978-3-642-02020-9>
- Richards, J. A., Woodgate, P. W., & Skidmore, A. K. (1987). An explanation of enhanced radar backscattering from flooded forests. *International Journal of Remote Sensing*, 8(7), 1093–1100. <https://doi.org/10.1080/01431168708954756>
- Rosenqvist, A., Shimada, M., Igarashi, T., Watanabe, M., Tadono, T., & Yamamoto, H. (2003). Support to multi-national environmental conventions and terrestrial carbon cycle science by ALOS and ADEOS-II -the Kyoto & carbon initiative. *IGARSS 2003. 2003 IEEE International Geoscience and Remote Sensing Symposium. Proceedings (IEEE Cat. No.03CH37477)*, 3(C), 1471–1476. <https://doi.org/10.1109/IGARSS.2003.1294147>
- Ruiz, L. A., Hermosilla, T., Mauro, F., & Godino, M. (2014). Analysis of the influence of plot size and LiDAR density on forest structure attribute estimates. *Forests*, 5(5), 936–951. <https://doi.org/10.3390/f5050936>
- Sai Bharadwaj, P., Kumar, S., Kushwaha, S. P. S., & Bijker, W. (2015). Polarimetric scattering model for estimation of above ground biomass of multilayer vegetation using ALOS-PALSAR quad-pol data. *Physics and Chemistry of the Earth*, 83–84, 187–195. <https://doi.org/10.1016/j.pce.2015.09.003>
- Saputro, G. B. (2009). *Peta mangroves Indonesia*. Cibinong, Bogor: Pusat Survey Sumber Daya Alam Laut, Badan Koordinasi Survey dan Pemetaan Nasional (Bakosurtanal).
- Sassi, M. G., Hoitink, A. J. F., de Brie, B., Vermeulen, B., & Deleersnijder, E. (2011). Tidal impact on the division of river discharge over distributary channels in the Mahakam Delta. *Ocean Dynamics*, 61(12), 2211–2228. <https://doi.org/10.1007/s10236-011-0473-9>
- Schreier, G. (1993). Geometrical properties of SAR images. In *SAR Geocoding - Data and Systems*. Karlsruhe: Wichmann.
- Shapiro, S. S., & Wilk, M. B. (1965). An analysis of variance test for normality (complete samples). *Biometrika*, 52(3–4), 591–611. <https://doi.org/10.1093/biomet/52.3-4.591>
- Shepashenko, D., Shvidenko, A., & Nilsson, S. (1998). Phytomass (live biomass) and carbon of Siberian forests. *Biomass and Bioenergy*, 14(1), 21–31. [https://doi.org/10.1016/S0961-9534\(97\)10006-X](https://doi.org/10.1016/S0961-9534(97)10006-X)
- Shimada, M., Isoguchi, O., Tadono, T., & Isono, K. (2009). PALSAR Radiometric and Geometric Calibration. *IEEE Transactions on Geoscience and Remote Sensing*, 47(12), 3915–3932. <https://doi.org/10.1109/TGRS.2009.2023909>
- Shimada, M., Itoh, T., Motooka, T., Watanabe, M., Shiraiishi, T., Thapa, R., & Lucas, R. (2014). New global forest/non-forest maps from ALOS PALSAR data (2007–2010). *Remote Sensing of Environment*, 155, 13–31. <https://doi.org/10.1016/j.rse.2014.04.014>
- Sidik, A. S. (2008). The change of mangrove ecosystem in Mahakam delta, Indonesia: A complex social-environment pattern of linkages in resources utilization. In *The South China Sea: Sustaining Ocean Productivities, Maritime Communities and the Climate Conference*. Kuantan, Malaysia.
- Singh, M., Malhi, Y., & Bhagwat, S. (2014). Biomass estimation of mixed forest landscape using a Fourier transform texture-based approach on very-high-resolution optical satellite imagery. *International Journal of Remote Sensing*, 35(9), 3331–3349. <https://doi.org/10.1080/01431161.2014.903441>
- Small, D., Jehle, M., Schubert, A., & Meier, E. (2009). Accurate geometric correction for normalisation of PALSAR radiometry.
- Solberg, S., Nasset, E., Gobakken, T., & Bollandsas, O.-M. (2014). Forest biomass change estimated from height change in interferometric SAR height models. *Carbon Balance and Management*, 9(1), 5. <https://doi.org/10.1186/s13021-014-0005-2>
- Stein, A. . F. van M. and B. G. (1999). Spatial Statistics For Remote Sensing. In *Spatial Statistics For Remote Sensing* (pp. 15–16). Dordrecht: Kluwer Academic.
- Sumareke, A. M. (2016). *Modelling and Mapping Aboveground Biomass and Carbon Stock Using Alos-2 Palsar-2 Data in Ayer Hitam Tropical Rainforest Reserve in Malaysia (Msc thesis)*. ITC, University of Twente, The Netherlands. Retrieved from http://www.itc.nl/library/papers_2018/msc/nrm/sumareke.pdf

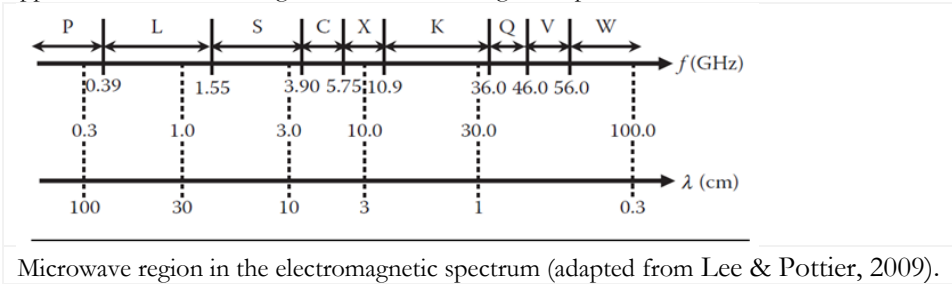
- Susilo, H., Takahashi, Y., & Yabe, M. (2017). Evidence for Mangrove Restoration in the Mahakam Delta, Indonesia, Based on Households' Willingness to Pay. *Journal of Agricultural Science*, 9(3), 30. <https://doi.org/10.5539/jas.v9n3p30>
- Suzuki, R., Kim, Y., & Ishii, R. (2013). Sensitivity of the backscatter intensity of ALOS/PALSAR to the above-ground biomass and other biophysical parameters of boreal forest in Alaska. *Polar Science*, 7(2), 100–112. <https://doi.org/10.1016/j.polar.2013.03.001>
- Takeuchi, W., Tien, D. V., Phuong, V. T., Van, A. N., Oo, K. S., & Resources, F. (2011). Above Ground Biomass Mapping of Mangrove Forest in Vietnam by ALOS. *3rd International Asia-Pacific Conference on Synthetic Aperture Radar (APSAR) 2011*, 3–5.
- Ter-Mikaelian, M. T., & Korzukhin, M. D. (1997). Biomass equations for sixty-five North American tree species. *Forest Ecology and Management*, 97(1), 1–24. [https://doi.org/10.1016/S0378-1127\(97\)00019-4](https://doi.org/10.1016/S0378-1127(97)00019-4)
- Thapa, R. B., Watanabe, M., Motohka, T., & Shimada, M. (2015). Potential of high-resolution ALOS–PALSAR mosaic texture for aboveground forest carbon tracking in tropical region. *Remote Sensing of Environment*, 160, 122–133. <https://doi.org/https://doi.org/10.1016/j.rse.2015.01.007>
- Thapa, R. B., Watanabe, M., Motohka, T., Shiraiishi, T., & Shimada, M. (2015). Calibration of Aboveground Forest Carbon Stock Models for Major Tropical Forests in Central Sumatra Using Airborne LiDAR and Field Measurement Data. *IEEE Journal of Selected Topics in Applied Earth Observations and Remote Sensing*, 8(2), 661–673. <https://doi.org/10.1109/JSTARS.2014.2328656>
- Tides4Fishing. (2019). High Tides and low tides, Balikpapan (30 July 2018). Retrieved January 30, 2019, from <https://tides4fishing.com/as/central-indonesia/balik-papan>.
- UNFCCC. (2010). Report of the Conference of the Parties on its fifteenth session, held in Copenhagen from 7 to 19 December 2009, Addendum, Part Two: Action taken by the Conference of the Parties at its fifteenth session. *Unfccc*, 1–43. <https://doi.org/10.1038/news.2009.1156>
- van der Werf, G. R., Morton, D. C., DeFries, R. S., Olivier, J. G. J., Kasibhatla, P. S., Jackson, R. B., ... Randerson, J. T. (2009). CO₂ emissions from forest loss. *Nature Geoscience*, 2, 737. Retrieved from <https://doi.org/10.1038/ngeo671>
- Van Laar, A., & Akca, A. (2007). *Forest Mensuration*. Springer (Vol. 13). Dordrecht: Springer Netherlands. <https://doi.org/10.1126/science.24.624.760>
- Villard, L., Le Toan, T., Ho Tong Minh, D., Mermoz, S., & Bouvet, A. (2016). Forest Biomass From Radar Remote Sensing. In *Land Surface Remote Sensing in Agriculture and Forest* (pp. 363–425). Elsevier. <https://doi.org/10.1016/B978-1-78548-103-1.50009-1>
- Wang, Y., Hess, L. L., Filoso, S., & Melack, J. M. (1995). Understanding the radar backscattering from flooded and nonflooded Amazonian forests: Results from canopy backscatter modeling. *Remote Sensing of Environment*, 54(3), 324–332. [https://doi.org/10.1016/0034-4257\(95\)00140-9](https://doi.org/10.1016/0034-4257(95)00140-9)
- Wang, Y., & Imhoff, M. L. (1993). Simulated and observed L-HH radar backscatter from tropical mangrove forests. *International Journal of Remote Sensing*, 14(15), 2819–2828. <https://doi.org/10.1080/01431169308904311>
- Watanabe, M., Shimada, M., Rosenqvist, A., Tadono, T., Matsuoka, M., Romshoo, S. A., ... Moriyama, T. (2006). Forest Structure Dependency of the Relation Between L-Band σ^0 and Biophysical Parameters. *IEEE Transactions on Geoscience and Remote Sensing*, 44(11), 3154–3165. <https://doi.org/10.1109/TGRS.2006.880632>
- World Agroforestry. (2019). Database: Wood Density. Retrieved January 5, 2019, from http://www.worldagroforestry.org/output?field_type_tid=63
- World Agroforestry Indonesia. (2018). Database: Wood Density. Retrieved December 2, 2018, from http://www.worldagroforestry.org/output?field_type_tid=63
- Wright, S. J. (2005). Tropical forests in a changing environment. *Trends in Ecology & Evolution*, 20(10), 553–560. <https://doi.org/10.1016/j.tree.2005.07.009>
- Zain, Z., Hutabarat, S., Prayitno, S. B., & Ambaryanto, A. (2014). Potency of Mahakam Delta in East Kalimantan, Indonesia. *International Journal of Science and Engineering*, 6(2). <https://doi.org/10.12777/ijse.6.2.126-130>
- Zwieten, P. A. M. van, Sidik, A. S., Noryadi, N., Suyatna, I., & Abdunnur, A. (2006). Aquatic food production in the coastal zone: data-based perceptions on the trade-off between mariculture and fisheries production of the Mahakam Delta and estuary, East Kalimantan, Indonesia. In *Environment and livelihoods in tropical coastal zones: managing agriculture-fishery-aquaculture conflicts* (pp. 219–236). Wallingford: CABI. <https://doi.org/10.1079/9781845931070.0219>

LIST OF APPENDICES

Appendix 1: Radar system and its comparison to optical RS system.

<p>Appendix 1A: Principle of the imaging radar system (adapted from ITC course materials, Anonymous, 2018).</p>	<p>Appendix 1B: Imaging radar system compared to optical RS system (adapted from ITC course materials, Anonymous, 2018).</p>

Appendix 2: Microwave region of the electromagnetic spectrum.



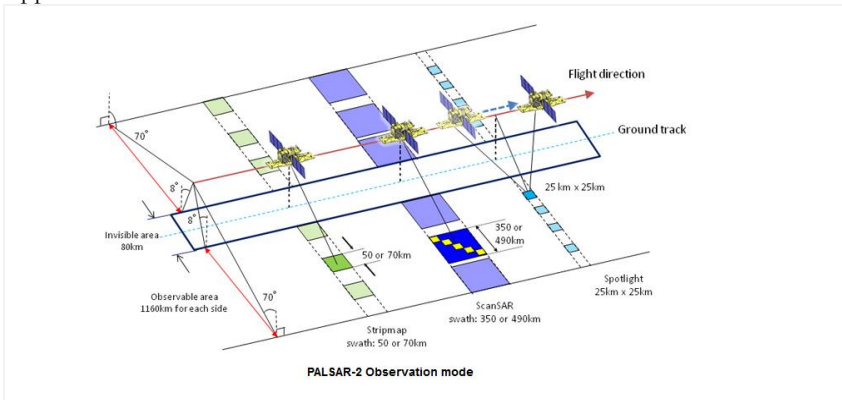
Appendix 3: SAR imaging geometry system.

<p> R_o = Distance between the radar and the antenna footprint centre L_x = Physical dimensions of the antenna L_y = Physical dimensions of the antenna ΔX = Range swath ΔY = Azimuth Swath θ_0 = Incident Angle </p>	<p>The SAR imaging system moves along its path having a velocity V_{SAR} at a height H. The antenna illuminates perpendicular to the flight direction and referred to azimuth (y). Then, the antenna beam is focused towards the ground at slantwise direction with an angle of incidence θ_0. The radar line of sight is called the slant range (r). The antenna footprint is the area covered by the antenna beam in the “ground range” (x) and azimuth (y) directions. The radar swath is the area scanned by the antenna beam.</p>
<p>SAR imaging geometry along with its description (adapted from Lee & Pottier, 2009).</p>	

Appendix 4: Outlook of ALOS-2 and observation attitude of PALSAR-2.

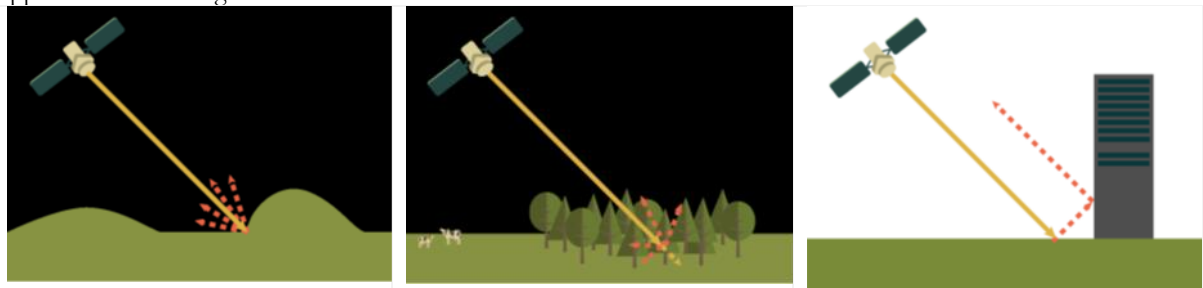
<p>Appendix 3A: Outlook of ALOS-2 (adapted from Kankaku et al., 2013)</p>	<p>Appendix 3B: PALSAR-2 Observation attitude (adapted from Kankaku et al., 2014)</p>

Appendix 5: Observation modes of PALSAR-2



PALSAR -2 observation modes (adapted from JAXA, 2016).

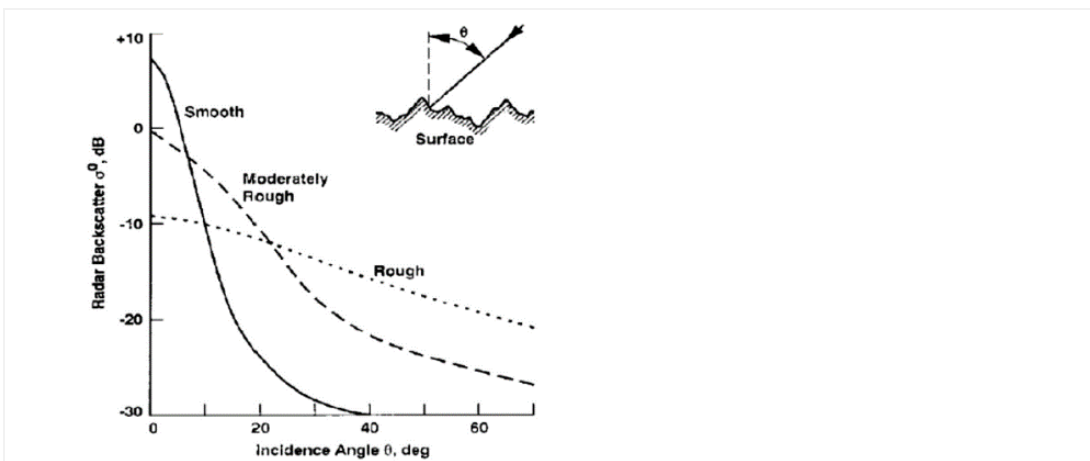
Appendix 6: Scattering mechanisms of Radar.



(a)Surface scattering (b)Volume scattering (c)Double-bounce scattering

Different types of scattering mechanisms of Radar (after, Evans et al., 1988).

Appendix 7: Incidence angle in relation to surface roughness.



Incidence angle in relation to surface roughness (adapted from Emery & Camps, 2017).

<p>Appendix 8: The diffuse, specular and corner reflectance.</p>	<p>Appendix 9: The effects of topography/local incidence angle on Radar backscattering.</p>
<p>Diffuse, specular and corner reflectance (adapted from Lillesand & Kiefer, 1994; Humboldt State University, 2016).</p>	<p>Effects of local incidence angle (adapted from Anonymous, 2018: Course Materials, ITC).</p>

Appendix 10: Tree height measurement of *Rhizophora spp.*

<p>Tree height measurement of <i>Rhizophora spp.</i>, measurement was taken from the ground to the top of the trees.</p>	<p>Tree height measurement of <i>Rhizophora spp.</i>, measurement was taken from the ground to the top of the trees.</p>

Appendix 11: DBH and tree height measurement of the *Avicennia alba* tree species.

<p>DBH measurement of <i>Avicennia spp.</i> at 1.3 m height from the ground.</p>	<p>Tree height measurement of <i>Avicennia spp.</i></p>

Appendix 12: Multi-stem trees of *Rhizophora* and *Avicennia* species.



Multi-stem *Rhizophora* tree species in the study area.

Multi-stem *Avicennia alba* tree species.

Appendix 13: An example of a field datasheet.

DATA COLLECTION FORM FOR MAHAKAM DELTA, INDONESIA

Name of Recorder: Date: 24 Oct 2019 Plot Radius Size:

D1201

Sampling Plot No.	Map scale	Map No.	Sample Plot Center X Y	Dist. to Center of plot. (m)	Bearing to Center of plot.	Elevation	Slope (%)	Aspect
<u>01</u>			<u>117.56454° 100.64008°</u>					

Forest characteristics:													
Land cover			Forest use type				Stand composition		Type of stand		Crown cover (%)	Undergrowth	
F	D	A	M	P	N	T	A	R	E	P	N	G	N

Tree No.	Species	DBH (cm)	Height (m)	Crown diam.(m)	Tree class				Tree No.	Species	DBH (cm)	Height (m)	Crown diam(m)	Tree class				
					1	2	3	4						d	1	2	3	4
1	Api-Api	10.6	12.38						21	Api-Api	11.3	10.73						
2	Api-Api	10.0	10.57						22	Api-Api	11.6	11.67						
3	Api-Api	13.3	12.25						23	Api-Api	14.1	11.77						
4	Api-Api	14.0	13.71						24	Api-Api	10.9	7.92						
5	Api-Api	13.0	14.38						25	Api-Api	10.6	11.78						
6	Api-Api	12.3	13.36						26	Api-Api	14.9	11.35						
7	Api-Api	23.7	15.88						27	Api-Api	12.5	10.03						
8	Api-Api	14.7	15.05						28	Api-Api	10.0	11.17						
9	Api-Api	15.4	11.49						29	Api-Api	14.7	15.37						
10	Api-Api	10.0	12.35						30	Api-Api	12.0	15.46						
11	Api-Api	11.3	12.09						31	Api-Api	10.0	12.83						
12	Api-Api	10.0	11.71						32	Api-Api	12.6	13.41						
13	Api-Api	10.3	13.05						33	Api-Api	11.3	12.53						
14	Api-Api	13.7	13.94						34	Api-Api	12.9	15.93						
15	Api-Api	14.5	13.44						35	Api-Api	14.6	13.52						
16	Api-Api	22.7	12.20						36	Api-Api	10.0	11.94						
17	Api-Api	14.7	12.99						37	Api-Api	11.5	11.01						
18	Api-Api	16.3	15.83						38	Api-Api	19.1	15.84						
19	Api-Api	11.0	11.67						39	Api-Api	21.0	15.46						
20	Api-Api	19.2	10.12						40	Api-Api	15.3	10.82						
									41	Api-Api	11.3	11.61						

Appendix 14: Ground surface during peak hours of low tide in the study area.



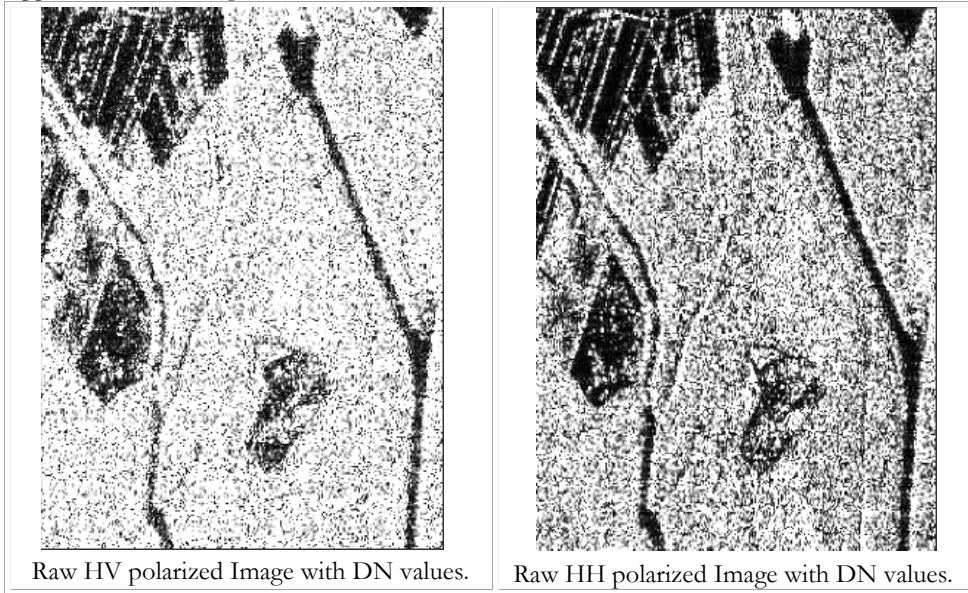
Ground condition during peak hours of low tide in the study area.

Appendix 15: Summary of the study parameters per plot; the plots with yellow marker denotes the validation plot and other plots are model plots.

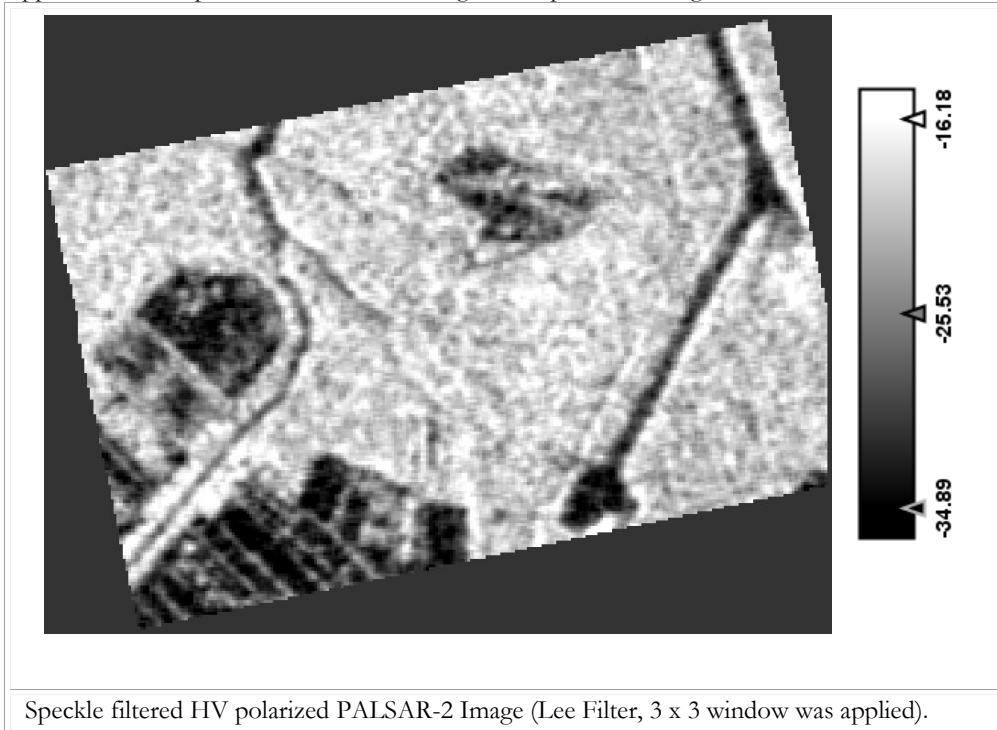
Plot_ID	Mean DBH	Mean Tree Height	BA (m ² /ha)	AGB (ton/ha)	Mean HV	Mean HH
P01	15.98	12.90	14.20	91.90	-21.55	-16.97
P02	15.96	10.70	16.50	89.90	-21.57	-14.01
P03	19.66	15.23	28.18	216.90	-16.77	-16.29
P04	16.21	13.34	10.99	96.70	-19.97	-18.52
P05	18.84	14.10	18.47	137.90	-20.14	-14.33
P06	15.12	13.45	17.47	111.30	-21.28	-13.96
P07	15.46	12.25	14.92	87.30	-21.43	-9.28
P08	19.54	15.44	29.80	279.50	-16.69	-12.28
P09	18.07	14.88	18.67	163.30	-18.21	-14.23
P10	16.23	12.25	23.93	146.20	-19.58	-12.42
P11	20.97	13.30	14.81	101.60	-21.09	-17.18
P12	15.03	18.25	17.68	151.30	-19.87	-16.35
P13	15.08	14.12	16.20	113.40	-21.65	-14.13
P14	14.02	15.31	19.27	154.40	-18.71	-15.78
P15	14.27	15.70	16.28	137.90	-19.92	-14.15
P16	14.62	18.25	12.62	115.10	-21.01	-11.20
P17	16.54	13.80	19.01	146.50	-19.55	-14.72
P18	22.65	15.14	28.67	236.30	-16.56	-12.51
P19	15.38	15.20	9.83	78.10	-22.20	-12.62
P20	21.39	16.40	37.70	339.60	-15.63	-11.97
P21	20.27	16.42	23.15	201.10	-17.33	-12.85
P22	18.85	16.94	23.00	208.20	-18.14	-11.20
P23	19.89	10.89	21.86	111.30	-22.07	-17.12
P24	18.34	12.87	13.20	86.20	-21.24	-14.73
P25	16.71	11.18	15.17	79.50	-20.03	-12.09
P26	19.73	14.80	23.57	194.10	-17.33	-11.06
P27	22.11	13.01	39.78	271.20	-16.04	-12.61
P28	18.74	17.35	25.87	259.10	-16.97	-11.79
P29	16.46	15.26	18.85	157.40	-18.34	-18.29
P30	14.94	15.12	16.18	126.50	-21.73	-16.41
P31	14.37	16.36	16.42	140.70	-19.61	-11.61
P32	15.43	15.36	15.63	118.80	-20.43	-12.28
P33	11.99	14.14	12.72	94.00	-21.61	-12.27
P34	15.28	14.90	14.03	109.00	-21.60	-11.24
P35	13.40	14.65	15.57	120.90	-20.46	-14.39

P36	17.66	16.41	26.99	246.90	-15.89	-11.36
P37	22.93	13.57	40.92	287.10	-16.77	-10.18
P38	12.04	11.97	4.28	28.30	-23.01	-16.32
P39	20.61	16.26	30.20	305.90	-15.91	-9.11
P40	19.97	14.55	26.73	206.10	-18.63	-10.83
P41	20.06	13.55	22.57	152.90	-19.34	-12.04
P42	18.70	12.39	17.67	111.40	-21.60	-12.09
P43	16.75	12.58	21.02	124.10	-21.37	-14.90
P44	15.25	13.80	16.92	119.20	-20.13	-12.56
P45	19.07	13.84	27.47	180.00	-17.79	-12.89
P46	18.59	14.82	13.55	101.40	-21.91	-14.37
P47	20.13	14.00	22.75	157.00	-18.41	-13.34
P48	18.12	14.45	18.76	140.60	-19.84	-11.43
P49	22.48	16.50	39.88	346.20	-14.54	-13.26
P50	17.55	18.09	16.87	145.30	-19.58	-11.00
P51	13.35	12.55	12.22	72.40	-22.42	-13.24
P52	15.05	14.39	15.95	110.20	-20.97	-12.75
P53	15.01	12.93	11.88	75.70	-22.31	-11.02
P54	14.25	14.01	17.30	112.30	-21.38	-18.48
P55	20.04	13.58	13.85	97.00	-20.37	-11.51
P56	13.57	13.65	15.03	116.10	-21.58	-14.75
P57	13.72	13.09	11.16	68.10	-22.20	-13.95
P58	14.55	12.78	10.22	61.80	-22.00	-13.16
P59	11.90	10.54	5.99	29.70	-22.29	-14.67
P60	14.02	12.66	13.53	84.90	-21.97	-25.86
P61	16.16	12.36	15.28	100.60	-21.40	-16.32
P62	14.02	12.53	12.77	86.50	-20.96	-15.64
P63	16.36	15.03	9.62	78.20	-22.40	-18.17
P64	13.55	10.99	11.11	63.80	-21.63	-12.73
P65	13.20	11.14	7.07	39.20	-22.62	-13.50
P66	18.36	14.26	12.95	99.50	-21.96	-13.29
P67	17.42	16.96	14.41	125.80	-21.15	-14.28
P68	18.47	15.99	12.80	107.30	-21.20	-14.60
P69	16.08	13.31	11.80	104.80	-19.83	-16.08
P70	13.90	12.62	8.76	59.00	-22.48	-16.16
P71	13.01	13.23	8.95	59.20	-21.91	-13.01

Appendix 16: The original ALOS-2 PALSAR-2 data with DN values.



Appendix 17: HV polarized PALSAR-2 image after speckle filtering.



Appendix 18: Some pictures of the water channels and Mahakam river near the sample plots, and muddy ground surface covered by water in the sample plots taken during data collection in the field.



A small water channels near a plot, the arrow indicates the water channel.



Muddy ground surface covered by water in the sample plot.



A small water channel near a plot indicated by the arrow.



The Mahakam river: the arrow indicates the location of the plot next to the river Mahakam.



A small water channel near a plot shown by the arrow.



Muddy ground surface covered by water.

Appendix 19: The photos of sample plot 3 and plot 4 taken during data collection.

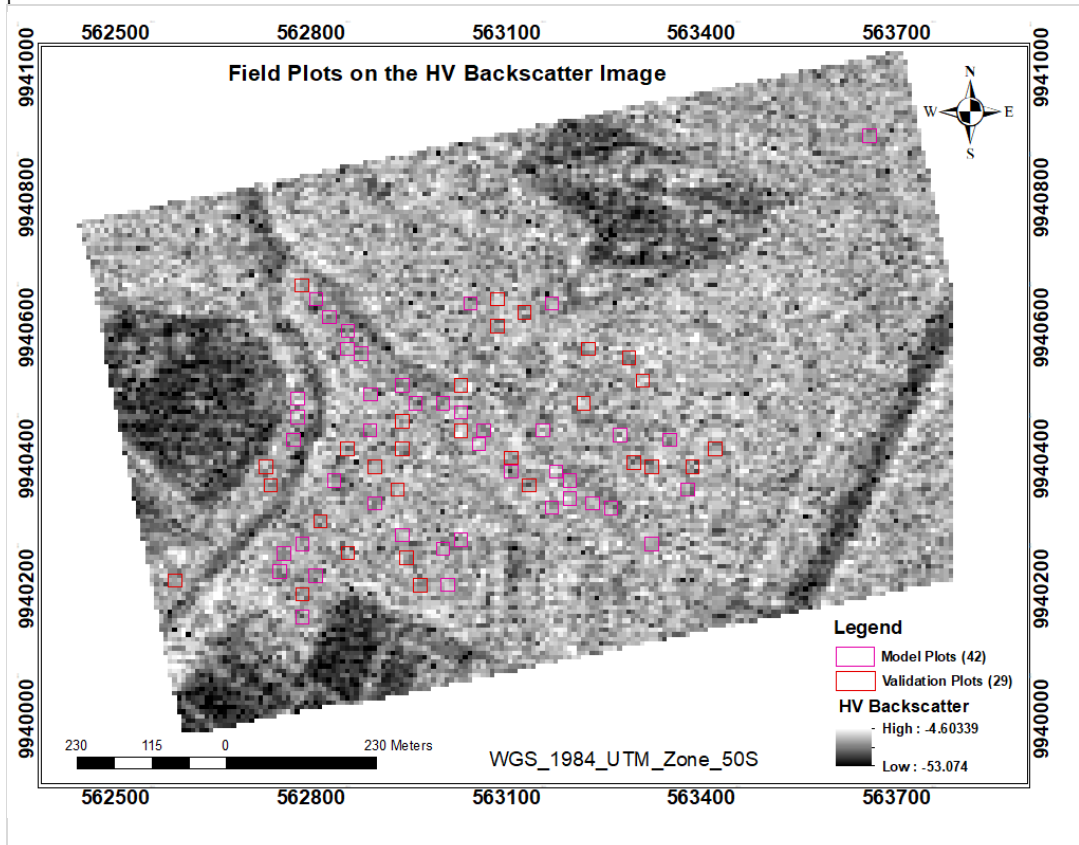


A field photo of plot 3.



A field photo of plot 4.

Appendix 20: The sampling plots (71) on the PALSAR-2 backscatter image; 42 plots for model development and 29 plots for model validation.



Appendix 21: The results of the correlation analysis between the field-measured AGB and speckle filtered HV polarization backscatter coefficients.

Correlation Statistics	Parameters	HV
Correlation	AGB	0.6408688
Sig (2-tailed)		1.746e-09
T value		6.9347
95% CI		0.4792161
		0.7604694

Appendix 22: The results of correlation analysis between AGB and other forest parameters.

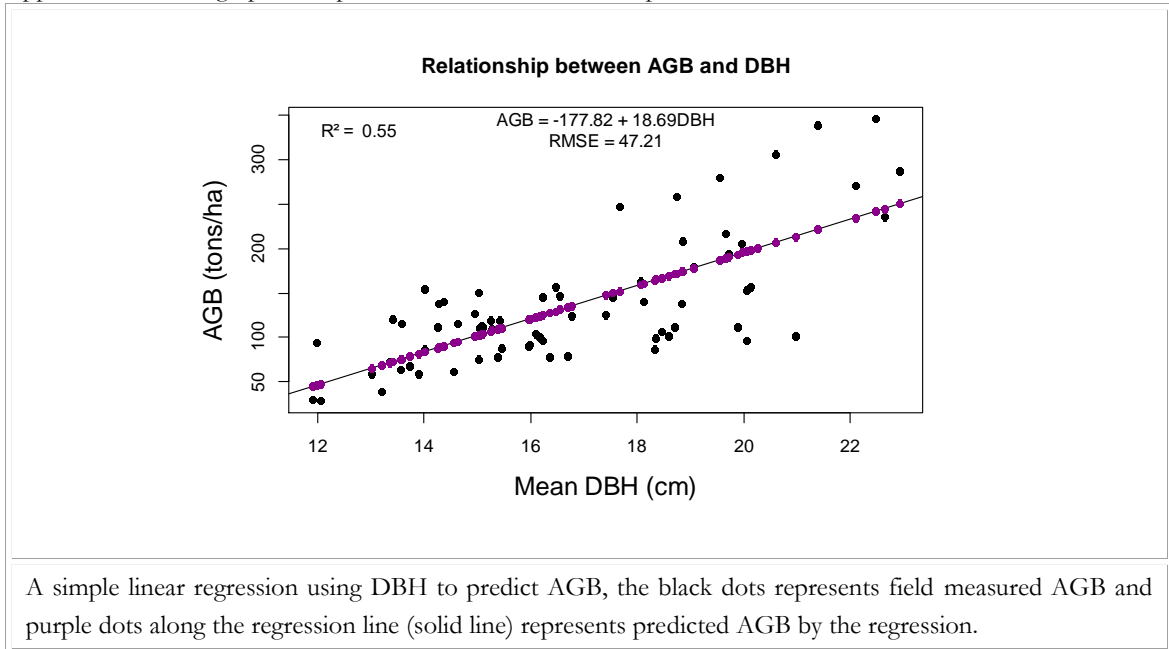
Correlation Statistics	Parameters	BA	DBH	Tree Height
Correlation	AGB	0.95	0.74	0.55
Sig (2-tailed)		< 2.2e-16	1.386e-13	6.238e-07
T value		24.194	9.1832	5.4906
95% CI		0.9142432	0.6146622	0.3650844
		0.9659628	0.8311182	0.6952779

Appendix 23: The results of the correlation between AGB and the derivatives of HH and HV polarization backscatter coefficients.

Correlation Statistics	Parameters	Sum of HV and HH	HV/HH	HH/HV
Correlation	AGB	0.74	-0.2308184	0.2030453
Sig (2-tailed)		1.339e-13	0.05279	0.08946
T value		9.1915	-1.9705	1.7225
95% CI		0.6150790 0.8313253	-0.440405922 0.002626792	-0.03176312 0.41661352

Appendix 24: Regression analysis between AGB and DBH.

Appendix 24A: The graphical representation of the relationship between AGB and DBH.

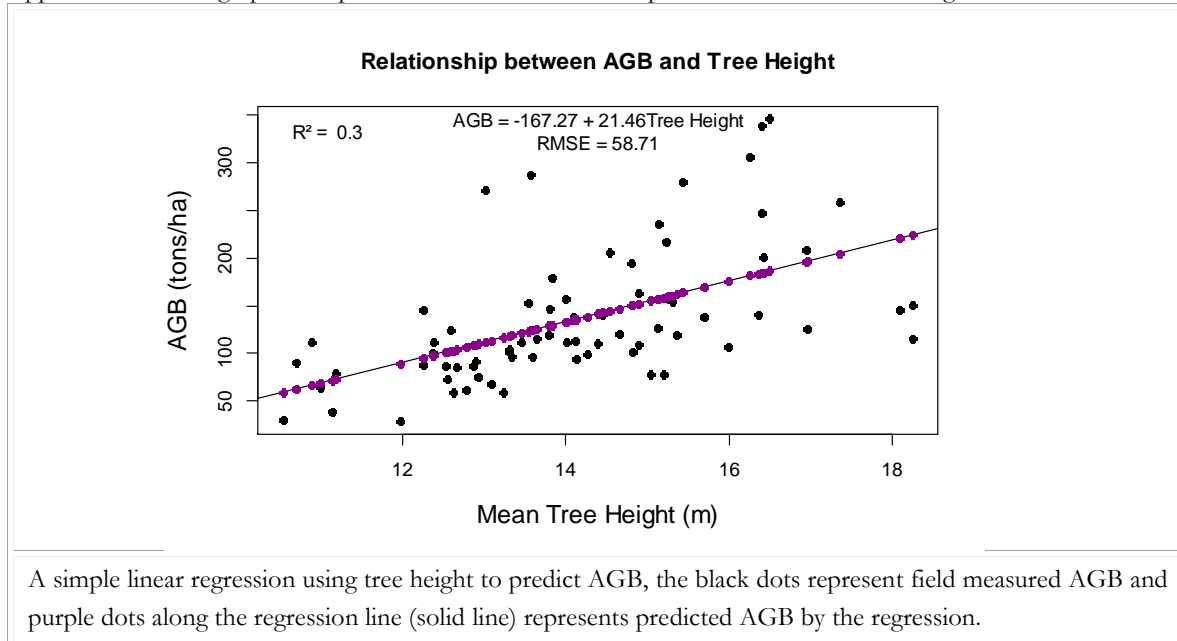


Appendix 24B: Summary statistics of regression between AGB and DBH.

Regression Statistics					
Multiple R	0.741615985				
R Square	0.549994269				
Adjusted R Square	0.543472447				
Standard Error	47.88749495				
Observations	71				
ANOVA					
	df	SS	MS	F	Significance F
Regression	1	193389.7488	193389.7488	84.33138073	1.38648E-13
Residual	69	158231.6399	2293.212173		
Total	70	351621.3887			
	Coefficients	Standard Error	t Stat	P-value	
Intercept	-177.8164784	34.6748813	-5.128106333	2.5568E-06	
DBH	18.688041	2.0350223	9.183211896	1.38648E-13	

Appendix 25: The regression analysis between AGB and tree height.

Appendix 25A: The graphical representation of the relationship between AGB and tree height.



Appendix 25B: Summary statistics of the regression between AGB and tree height.

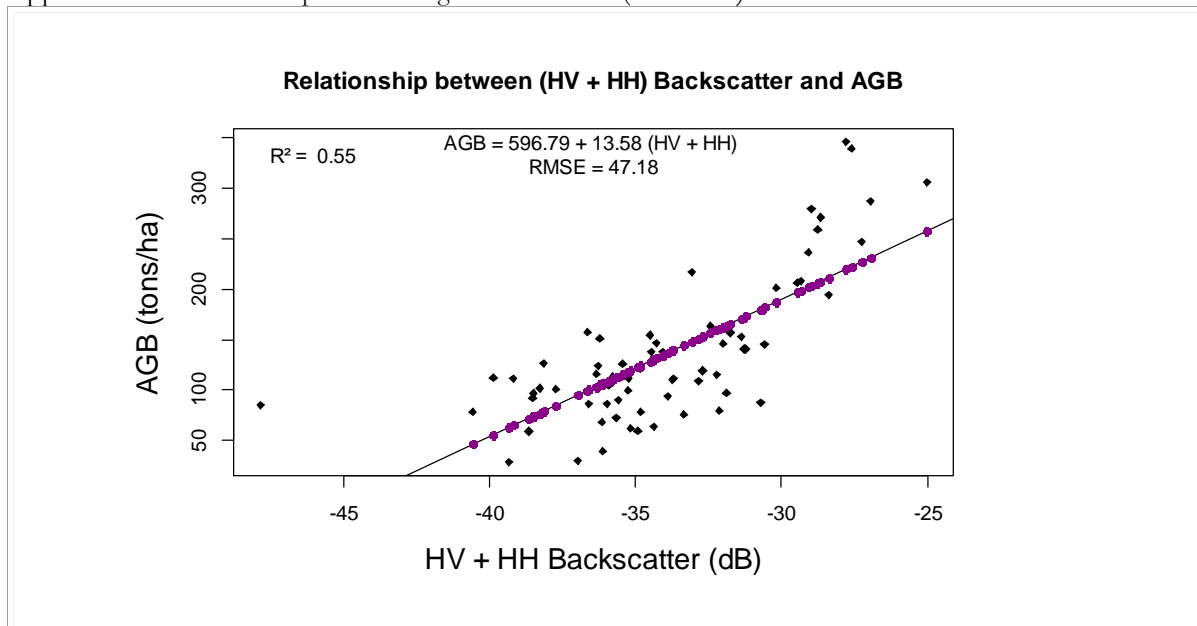
Regression Statistics					
Multiple R	0.551420604				
R Square	0.304064683				
Adjusted R Square	0.293978664				
Standard Error	59.55216234				
Observations	71				
ANOVA					
	df	SS	MS	F	Significance F
Regression	1	106915.646	106915.646	30.14714528	6.23793E-07
Residual	69	244705.7427	3546.460039		
Total	70	351621.3887			
	Coefficients	Standard Error	t Stat	P-value	
Intercept	-167.2653479	55.73843466	-3.000897834	0.00374429	
Tree Height	21.45501577	3.907560774	5.490641609	6.23793E-07	

Appendix 26: Residuals of the regression analysis between HV backscatter and AGB.

4.449794	-7.33394	7.451926	22.66228	43.11613	23.30384	-32.2932	-24.5409
0.719365	-0.35033	61.13759	-30.3192	-13.4452	-32.6327	27.89623	-17.456
-22.2814	10.36103	-23.215	44.36403	33.84988	-5.34371	-1.38559	22.08114
-39.4527	26.75574	8.241246	-12.573	21.475	34.31819	-14.4715	23.64795
3.561936	-23.6268	40.29858	-7.92185	-8.47211	-9.27613	-36.2383	6.703549
12.69941	-3.42162	-12.9142	4.701728	21.4184	9.241921	18.10665	-37.6068
-10.1929	5.881357	-60.0112	18.26757	29.36152	1.087471	7.921943	0.378067
34.57169	-5.92865	-31.5725	-3.04049	-16.6161	7.398839	-20.8484	-20.212
-32.0071	-12.3988	6.077635	-24.1005	-29.5556	20.83003	18.71675	

Appendix 27: The regression analysis between the sum backscatter coefficients (HV+HH) and AGB.

Appendix 27A: The scatterplot of the regression between (HV+HH) backscatter coefficients and AGB.

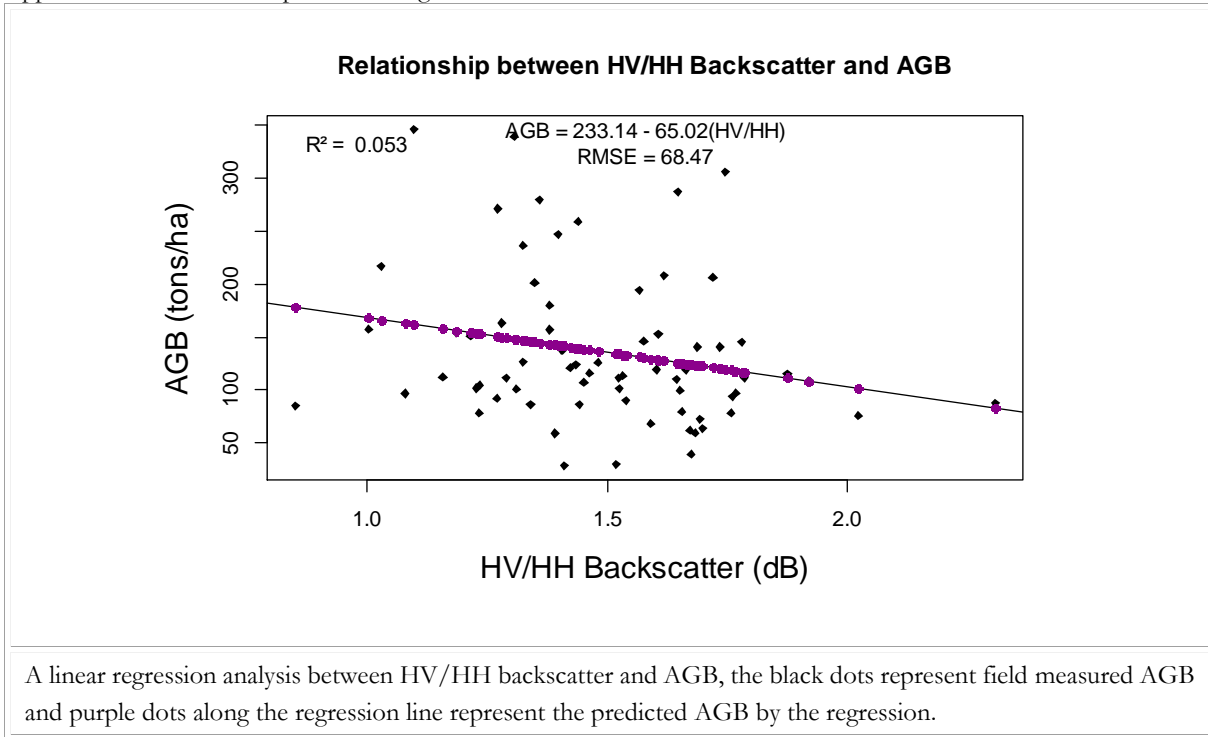


A linear regression analysis between HV + HH backscatter and AGB, the black dots represent field measured AGB and purple dots along the regression line represent the predicted AGB by the linear regression.

Table 27B: Summary statistics of the relationship between AGB and the sum of HV and HH backscatter.

<i>Regression Statistics</i>					
Multiple R	0.741917392				
R Square	0.550441416				
Adjusted R Square	0.543926074				
Standard Error	47.86369742				
Observations	71				
<i>ANOVA</i>					
	<i>df</i>	<i>SS</i>	<i>MS</i>	<i>F</i>	<i>Significance F</i>
Regression	1	193546.9751	193546.9751	84.48388944	1.33921E-13
Residual	69	158074.4136	2290.933531		
Total	70	351621.3887			
	<i>Coefficients</i>	<i>Standard Error</i>	<i>t Stat</i>	<i>P-value</i>	
Intercept	596.7874231	50.41974636	11.83638289	2.83804E-18	
HH+HV	13.57849411	1.477286259	9.191511815	1.33921E-13	

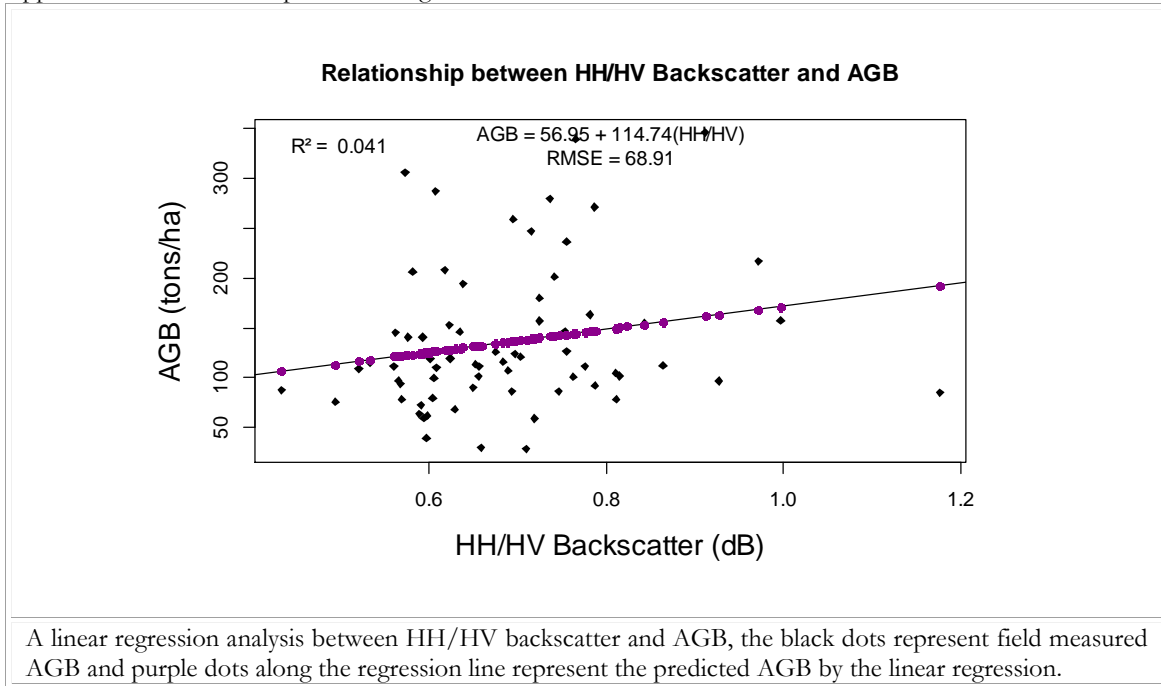
Appendix 28: The regression analysis between the ratio of HV/HH backscatter coefficients and AGB.
 Appendix 28A: The scatterplot of the regression between the ratio of HV/HH backscatter and AGB.



Appendix 28B: Summary statistics of the regression between AGB and the ratio of HV/HH backscatter coefficients.

<i>Regression Statistics</i>					
Multiple R	0.230818396				
R Square	0.053277132				
Adjusted R Square	0.039556511				
Standard Error	69.45836095				
Observations	71				
<i>ANOVA</i>					
	<i>df</i>	<i>SS</i>	<i>MS</i>	<i>F</i>	<i>Significance F</i>
Regression	1	18733.37919	18733.37919	3.882997064	0.052791009
Residual	69	332888.0095	4824.463906		
Total	70	351621.3887			
	<i>Coefficients</i>	<i>Standard Error</i>	<i>t Stat</i>	<i>P-value</i>	
Intercept	233.1416114	49.82931731	4.678804045	1.39255E-05	
HV/HH	-65.02370529	32.99804287	-1.970532178	0.052791009	

Appendix 29: The regression analysis between the ratio of HH/HV backscatter coefficients and AGB.
 Appendix 29A: The scatterplot of the regression between the ratio of HH/HV and AGB.



Appendix 29B: Summary statistics of the regression between AGB and the ratio of HH/HV.

Regression Statistics					
Multiple R	0.203045275				
R Square	0.041227384				
Adjusted R Square	0.027332129				
Standard Error	69.89899118				
Observations	71				
ANOVA					
	<i>df</i>	<i>SS</i>	<i>MS</i>	<i>F</i>	<i>Significance F</i>
Regression	1	14496.42996	14496.42996	2.967011612	0.089458409
Residual	69	337124.9588	4885.868968		
Total	70	351621.3887			
	Coefficients	Standard Error	t Stat	P-value	
Intercept	56.95088013	46.80958072	1.21665008	0.227882736	
HH/HV	114.7389694	66.61182337	1.722501557	0.089458409	